UNIVERSITÀ
DEGLI STUDI
DI PADOVA

Università degli Studi di Padova

Dipartimento di Scienze Chimiche

Center for Nanoscience and Technology, CNST@PoliMi,

Istituto Italiano di Tecnologia

The Stability of Third Generation Solar Cells

SCUOLA DI DOTTORATO DI RICERCA IN: SCIENZA ED INGEGNERIA DEI MATERIALI

CICLO: XXVII

Direttore della Scuola: Ch.mo Prof. Gaetano Granozzi

Supervisore: Ch.mo Prof. Guglielmo Lanzani

Ch.mo Prof. Moreno Meneghetti

Tutor: Dr. Annamaria Petrozza

Dottorando : Michele De Bastiani

Preface

In the lasts fifty years the tremendous evolution of modern technologies has gradually unbalanced the equilibrium between the production and the consumption of energy. Traditional energy resources, like coal, oil and natural gases, are no longer sufficient to satisfy the demand of energy without spoiling earth environment. Renewable energies have attracted a lot of attention because they are potential solution to this important problem. In particular photovoltaic solar cells are considered the most promising technology for a low-cost and environmentally friendly energy production. However, in order to exploit these technologies in real world applications, the complete physics of solar cells must be understood. Stability is one of the fundamental aspects and is related to the processes that regulate the energy conversion, both in long-term degradation as well in electrical stability. In this work the stability of two emerging categories of solar cells is thoroughly addressed: organic photovoltaics and organometal-halide perovskite.

In organic photovoltaics understanding the stability and degradation mechanisms of photoactive blends is required to achieve long device lifetimes. Recent reports on organic solar cells presenting power conversion efficiencies exceeding 10% have made the need to improve the device stability compelling. In general, instability is caused by the combination of light and atmospheric agents, with major roles of oxygen and water. The detrimental effects are electron trapping and photo-oxidation that break polymer conjugation and bleach the absorption. However, so far, no effective solution preserving low cost and flexibility has been achieved. The reason is that the degradation mechanisms are still unknown.

Solution-processable hybrid perovskite semiconductors have risen to the forefront of photovoltaics research, offering the potential to combine low-cost fabrication with high-power conversion efficiency (PCE). Originally used in dye-sensitized solar cell technology, the first architectures saw the use of TiO_2, both in the form of mesoporous and compact films, as an electron

extracting layer. Further development has been driven by empirical optimization strategies and testing of a variety of different architectures. These devices are divided in two categories: standard and inverted. Standard uses TiO_2 (compact or mesoporous) to collect the electrons and a small molecule or polymer organic semiconductor for the holes, with record efficiencies of 21% and an open circuit voltage above 1 V; it must be noted that these devices exhibit a kind of electrical instability manifested as slow transient and hysteretic effects that severely affect the final efficiency. The inverted configuration is more similar to organic photovoltaics, exploiting similar materials for the extraction of photogenerated charges. These devices report lower efficiencies respect to standard device but a higher electrical stability which is manifest with stabilized efficiencies and apparently hysteresis-free behaviour.

Abstract

Negli ultimi cinquant'anni la rapida evoluzione delle tecnologie ha gradualmente sbilanciato l'equilibrio che esiste tra la produzione e il consumo dell'energia. Le risorse tradizionali che vengono sfruttate per la produzione di energia - carbone, petrolio e gas naturali - iniziano ad essere sempre meno sufficienti per soddisfare la richiesta di energia senza rischiare di danneggiare l'ambiente che ci circonda. E' proprio per questo motivo che le energie rinnovabili attraggono sempre più interessi e attenzioni andandosi a candidare come una potenziale soluzione al fabbisogno energetico. Tra le energie rinnovabili, il fotovoltaico si conferma come una delle tecnologie più promettenti per fornire energia a costi contenuti nel rispetto dell'ambiente. Tuttavia per poter sfruttare appieno il potenziale di questa tecnologia la fisica e i meccanismi di conversione fotovoltaica devono essere studiati nel dettaglio. Tra questi la stabilità delle celle solari ricopre uno degli aspetti fondamentali, dove per stabilità si intendono sia la durata e il tempo di vita dei dispositivi sia la stabilità dei meccanismi elettrici delle celle. In questa tesi viene studiata nel dettaglio la stabilità di due tecnologie emergenti nel settore fotovoltaico: le celle solari polimeriche e le celle solari a base di perovskiti.

Nelle celle solari polimeriche capire e comprendere i meccanismi di degrado dei materiali foto attivi permette di sviluppare nuovi materiali in grado di aumentare la durata e l'efficienza delle celle. In generale, il degrado di questi dispositivi è dovuto all'interazione tra la parte ultravioletta della luce e gli agenti atmosferici, in particolare ossigeno e vapore acqueo. Gli effetti del decadimento si riscontrano da un lato nella formazione di stati elettronici che fungono da "trappole" per le cariche fotogenerate diminuendo l'efficienza generale della cella, dall'altro nella modifica chimica dei materiali che porta ad una rottura delle catene polimeriche deteriorando completamente le proprietà ottiche della cella. Studiare e comprendere questi meccanismi è la corretta strada per lo sviluppo di nuovi materiali per celle più efficienti.

L’introduzione delle perovskiti ibride ha rappresentato una rivoluzione nel settore fotovoltaico. Questa tipologia di materiali offre il vantaggio sia di essere processabile da soluzioni sia quello di avere un’efficienza confrontabile a quella del silicio cristallino. Inizialmente queste perovskiti erano utilizzate come materiale fotoassorbente in celle solari simili alle dye senistized solar cells (DSSCs). Questi primi dispositivi sfruttavano uno scaffold mesoporoso di diossido di titanio per estrarre gli elettroni. Successivamente, in seguito allo sviluppo empirico delle celle, lo scaffold mesoporoso è stato rimosso in favore di una configurazione planare. Tuttavia, in entrambe le configurazioni, queste celle hanno dimostrato una naturale instabilità elettrica che si manifesta in una forma di isteresi nella determinazione della caratteristica curva corrente/voltaggio. Questo fenomeno rende ambigua la determinazione finale dell’efficienza di questi dispositivi limitandone effettivamente le possibili applicazioni. In questa tesi viene presentata un’indagine completa delle cause e delle conseguenze di questo fenomeno, mostrando una possibile soluzione a questo problema.

Thesis Plan

The thesis is divided into 6 chapters.

Chapter 1 is dedicated to the background of photovoltaics. The physics of the solar cells through light-to-current conversion is introduced together with the main characteristics of photovoltaic devices.

Chapter 2 is dedicated to the detailed description of thin films solar cells. In particular, the working principles and the description of the different materials used in organic photovoltaics and in perovskite solar cells are examined.

Chapter 3 describes all the experimental tools and techniques used, including sample fabrication, solar cell realization and the analysis techniques used in the further chapters.

Chapter 4 contains a detailed analysis of the photophysicals mechanisms for an Organic Photovoltaics blend: PCPDTBT/PCBM through the joint of optical and magnetic spectroscopy techniques. Subsequently, the chapter analyzes the main findings in the degradation processes that hamper the stability of these materials.

Chapter 5 is dedicated to the description of the optical properties of organometal halide perovskite. The optical absorption, the photoluminescence and the Raman spectra are considered as a function of the crystallization substrates and of the perovskite crystals size. Finally, the degradation of the optical properties in presence of moisture and electric fields is described.

Chapter 6 provides a complete description of the electrical properties of the organometal halide perovskite. The main issue is discussion on the electrical instability, manifested as hysteretic behaviour, that affects the determination of the final efficiency of the solar cells. The nature of this phenomenon and the possible solution by the explanation of optimized charge extraction layers is reported.

Contents

Chapter 1
The Physics of Solar Cells

The humankind needs energy to exist. This energy is constantly produced through technologies that have evolved over time. One of the main factors that characterize the production of energy is the resource that is being exploited. The resources available can be divided in two main categories: non-renewable and renewable. In the first category are included all the sources of energy that can be exploited in a finite quantity, or with a regeneration time long enough to be considered finite in quantity. Coal, natural gases, petroleum and its derivatives, radioactive elements. All these resources are in the first category. The amount of energy that can be obtained from these resources is in generally high. In second category all the resources with an instantaneous regeneration are included, which means inexhaustible sources of energy. Tides, geothermal, hydroelectricity, wind and solar are the main sources of renewable energy. The energy currently obtained from these resources is generally lower compared to non-renewable, however the idea of a theoretically inexhaustible source of energy attracts a lot of attention, especially in sight of a possible depletion of non-renewable sources.

Researchers, scientists and industries have collaborated over the years to find an answer to the constant demand of energy. Nowadays, the modern sources of energy implemented in everyday life are the results of years of study, research development and, finally, industrialized processes. Among all the different sources, both renewable or not, solar energy has always attracted a lot of interests. The energy provided by the Sun in the form of light is something natural as clearly shown in photosynthesis. The idea to convert sunlight into a usable form of energy is the base concept of the solar cell. The solar cell is an optoelectronic device able to convert light into electric current, both the direct Sun light and also artificial or ambient light. However, the term light is referred here as the electromagnetic radiation emitted by the Sun onto the surface of the Earth. The Sun emits electromagnetic waves all over the spectrum of frequencies like a black body with a calculated temperature of 5777 K[1]. Only a fraction of this radiation reaches the surface of the Earth. The air mass coefficient (AM1.5) is an index used to determine the effective electromagnetic radiation emitted by the Sun at the sea level (figure 1.1)[2]. The main losses with respect the pristine emission are due absorption by the atmosphere of the Earth. Ozone, water vapour, oxygen and carbon dioxide are the relevant absorbing agents that preclude the ultraviolet (UV) and some parts of the infrared (IR) portions of the solar spectrum. The AM1.5 spectrum represents the

maximum amount of energy available for a solar cell to be converted in electrical current. According to the AM1.5 spectrum the maximum irradiance peak is in the visible region, however an ideal solar cell must be able to convert the whole part of the spectrum to maximize the yield of photogenerated current.

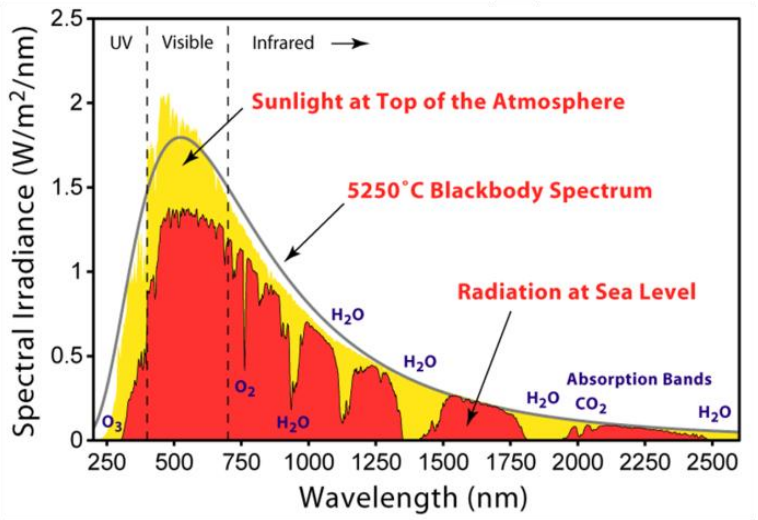

Figure 1.1: Solar irradiance spectrum above the atmosphere and at the surface, taken from [2].

As already anticipated, a solar cell is an optoelectronic device able to convert light into electric current, which means that a solar cell can be imagined as a "black box" where light goes in and electrons go out. The different nature of the "black box" is what differentiates the numerous types of solar cells. In principle all the different kind of solar cells must respect these characteristics[1]:

- *Being able to absorb the incident light*. Light must be absorbed prior to be converted into electric current. The absorption of light is a characteristic of the core material used to realize the solar cell and is related to the absorption spectrum of the material itself. The absorption spectrum is the fraction of incident radiation absorbed by the material over a range of frequencies and is determined by the atomic and molecular composition of the material. An ideal candidate core material for current generation in a solar cell has an absorption spectrum that matches with the AM1.5 spectrum.
- *Being able to generate charges.* Light absorption is the first step, the second is the generation of photocarriers. The core of a solar cell must be able to generate both the electron and hole with the energy provided by the absorption of light. There are several mechanisms in which the photogeneration occurs. This process defines the type of the solar cell. The materials that fulfil the requirements are semiconductors

that thanks to their electronic band structure, can generate pairs of electrons and holes effectively.

- *Being able to transport the charges.* Once light is absorbed and the charges have been generated, the solar cell must be able to collect them in a current. Without any driving force the photogenerated electron and hole will recombine geminately. To collect them efficiently, the solar cell must provide an internal electric field, usually defined as the built-in field, which transports the electrons and the holes in opposite directions. The built-in field is optimized with the engineering of the solar cell: it can be a modification of the core material or the inclusion of other materials which act as selectors of the carriers thanks to a different alignment of the energy levels.

The history of solar cells can be divided in three parts (figure 2)[3]. The "first generation" of solar cell was based on silicon wafers. The main problem for this technology was the requirement for high volume of starting materials. A "second generation" of solar cells was developed from the early 1980s. These solar cells used the thin-film technology. Regardless of the semiconductor involved, thin film technology offers prospects for a large reduction in costs by minimising the quantity of material used. However, even for these solar cells the balance between costs and energy produced has become negative over time. For this reason, the researchers pushed towards new types of solar cells that exploited alternative mechanisms of energy conversion. This latter type of solar cells represents the "third generation" of solar cells.

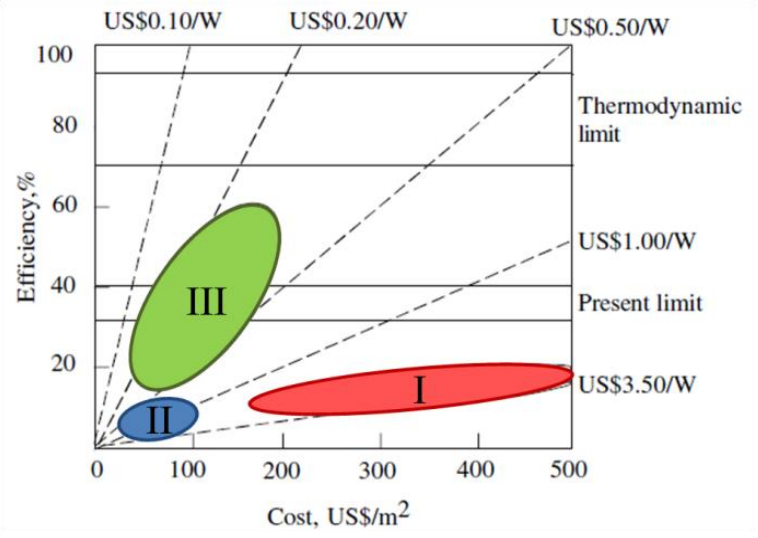

Figure 1.2: Efficiency-cost trade-off for the three generation of solar cells. Taken from [3].

The third generation of solar cells represents the most promising technologies for the evolution of photovoltaic systems (figure 1.3) [4].

Multijunction solar cells, employing several layers of semiconductors in order to cover the whole solar spectrum, retain the record in terms of conversion efficiencies. Emerging photovoltaics are attracting more and more interest due to their potential cost benefits in a broad range of applications for example in multijunction solar cells and on flexible substrates.

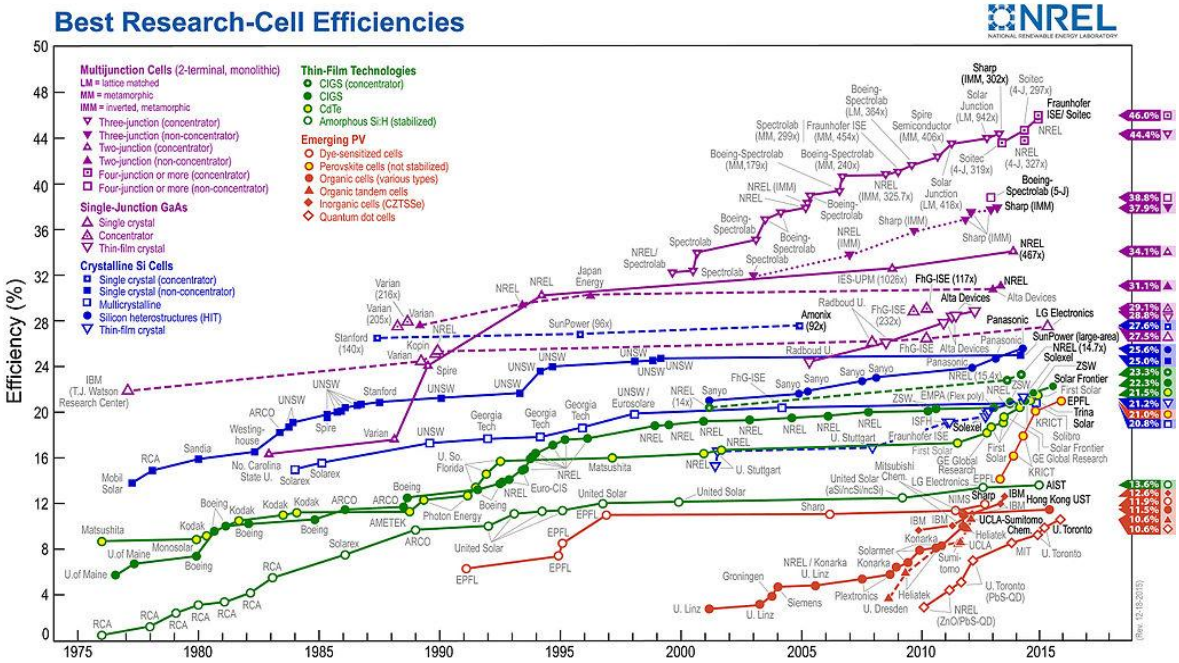

Figure 1.3: Reported timeline of solar cell energy conversion efficiencies. From NREL (National Renewable Energy Laboratory) website[4].

Even if the resulting efficiencies are not the same as multijunction or crystalline silicon, many of these new solar cells can be made from solution-processed techniques that may drastically lower the cost of production. These can be realized with industrial printing techniques such as roll-to-roll, slot dye, inkjet printing and bar coating and thus are easily scalable to large productions. In this category of solar cells there are two promising photovoltaics systems: organic solar cells and perovskite solar cells.

Organic solar cells, also referred as organic photovoltaics (OPV), use the concept of semiconducting organic polymers or small molecules for light absorption and charge transport. This technology was first developed in the 1990s[5] and attracted a lot of interest mainly due to the reduced cost of production and due to additional possible applications. These solar cells are flexible, light and semitransparent. Thanks to these

properties they may find a place in building integrated and portable electronics[6]. The limiting factors of this type of solar cell are the low efficiency and the long term stability.

Perovskite solar cells (PSC) are a relatively new concept of photovoltaics. The first demonstration of the use of perovskites in solar cells was in 2009[7], however it was in 2012 that the perovskites start a revolution in photovoltaics[8]. These cells exhibit some of the advantages of OPV, such as being solution processable, with the upgrade of having efficiencies comparable with crystalline silicon. The disadvantages of PSC are related to the electronic stability of the cell itself.

1.1 Characteristics of Solar Cells

The solar cell can be compared with a battery in a simple electrical circuit, with the difference that in the dark the cell does nothing[9]. When it is illuminated the cell develops a photovoltage. When the two terminals of the cell are isolated (like with an infinite load resistance) the photovoltage created is defined as the *open circuit voltage* (V_{oc}). The current generated by the cell under illumination when the two terminals are connected togheter is the *short circuit current* (I_{sc}). For a load resistance (R_L) the cell provides a current I(V) for voltages between 0 and V_{OC} according to Ohm's law: $V = R_L I$. I(V) defines the current-voltage characteristic of the cell under a particular illumination. Since the current generated by the cell is proportional to the illuminated area, the short circuit current density (J_{sc}) replaces the I_{sc}, as the current normalized over this area.

A standard solar cell behaves like a diode in dark (figure 1.4), with a different amount of current under forward bias ($V > 0$) respect to reverse bias ($V < 0$). This rectifying behaviour is a feature of photovoltaic devices and is a consequence of the asymmetric junction needed to separate charges. Under light the I(V) characteristic of the diode is shifted by a factor theoretically proportional to the short circuit current. The resulting total current is the superimposion of the photocurrent and the dark current.

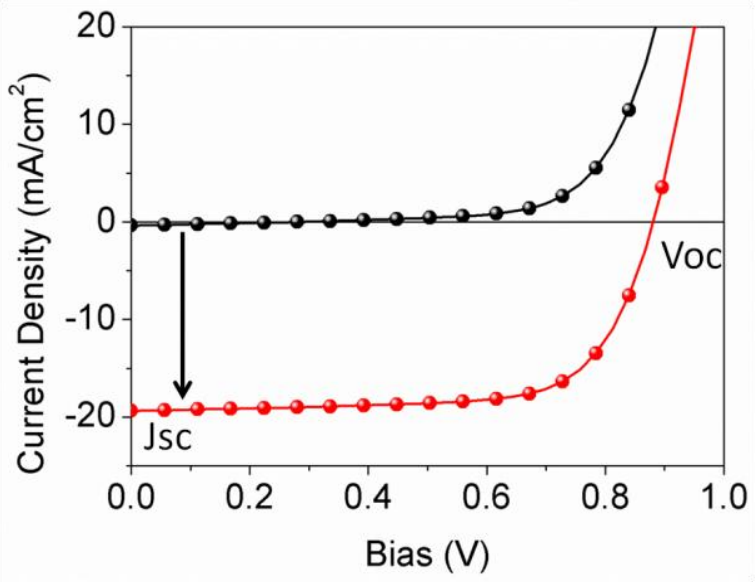

Figure 1.4: Current-voltage characteristic of an ideal solar cell in light (red line) and in dark (black line). The sign convention is with a negative short circuit current.

Electrically, the solar cell is equivalent to a current generator in parallel with a diode (figure 1.5). The photocurrent produced is divided between the variable resistance of the diode and the load applied. Without the diode there is no photovoltage and nothing to lead the photocurrent through the load.

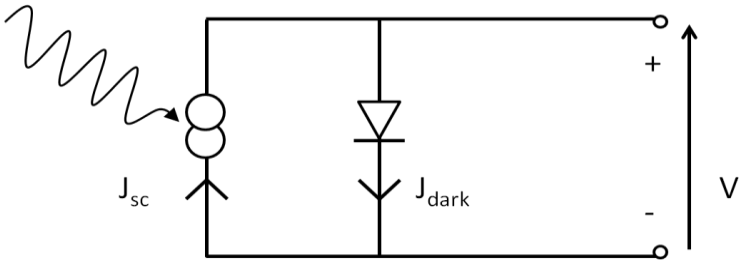

Figure 1.5: Equivalent circuit of ideal solar cell.

The working zone of a solar cell is the range of bias from 0 to Voc. Within this range the cell delivers power. The power density of the cell is:

$$P = JV \tag{1}$$

The maximum value of P is defined as the maximum power point of the cell, which occurs at some voltage V_m with the corresponding current density J_m. This means that

the optimum load for a solar cell has a resistance given by V_m/J_m. The Fill Factor (FF) can be defined from J_m and V_m as:

$$FF = \frac{J_m V_m}{J_{sc} V_{oc}} \tag{2}$$

which basically describes the "squareness" of the J-V curve.

The efficiency η of a cell is the power delivered at the maximum power point as a fraction of the incident light power density P_s:

$$\eta = \frac{J_m \mathrm{V_m}}{P_s} \tag{3}$$

Using the definition of FF in (3):

$$\eta = \frac{J_m \mathrm{V_m} FF}{P_s} \tag{4}$$

The four quantities: J_{sc}, V_m, FF and η are the key performance characteristics of a solar cell. These must be defined under standard illumination conditions using the AM1.5 spectrum under an incident power density of 1000 W/m^2.

1.2 The Physics of Semiconductors

When two atoms form a molecule their atomic orbitals combine to create pairs of molecular orbitals with the energy levels slightly separated from the originals. When many atoms form a solid, the separation energy of all the orbitals becomes so close that forms a *continuum* of accessible levels. This *continuum* is defined with the term of *band*. Previously it was noted that a suitable photovoltaic material should absorb visible light. This process requires the material to have a gap in its bands. This defines a *band gap* which is a separation in energy between the highest occupied state and the lowest unoccupied state. All semiconducting and insulating material possess a band gap, but only semiconductors have the right gap in order to be used in light absorption, since the gap of insulators is too big[10]. Without a band gap, like in metals, the excited electrons don't have enough time to be collected once excited: electrons would decay through a continuum of intermediate levels. In the presence of a band gap, when an electron is excited it quickly decays to the minimum energy of the conduction band, this process

takes few femtoseconds[11]. Then the recombination to the valence band occurs with a slower mechanism which takes several microseconds, giving enough time to the solar cell to extract the electron. This process is sketched in figure 1.5.

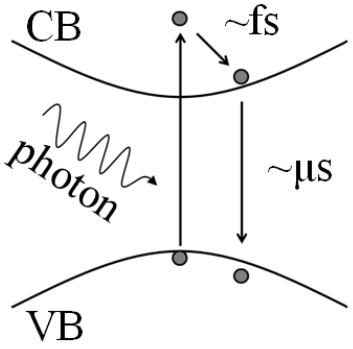

Figure 1.5: Excitation mechanism of an electron from the valence band (VB) to the conduction band (CB) by the absorption of a photon. The thermalization and recombination dynamics are also reported.

The nature of the band gap in a material is related to its atomic characteristics[11]. When two atoms form a molecule, the respective electron orbitals in the atoms combine together to form molecular orbitals, with new energy levels. When this process is repeated to form a solid, each atomic orbital splits in a continuum of levels forming a "band". Now, these bands may or not overlap and this is due to the energy distribution, which is a reflection of the electronic properties of the atoms. The occupation of these bands depend on the original occupation of the molecular orbitals. The highest occupied band is defined as the *valence band* (VB). The lowest unoccupied band is defined as *conduction band* (CB). If the valence band and the conduction band overlap the solid is a metal, if the two band are separated in energy the solid is a semiconductor or an insulator if the separation is large. See sketch in figure 1.6.

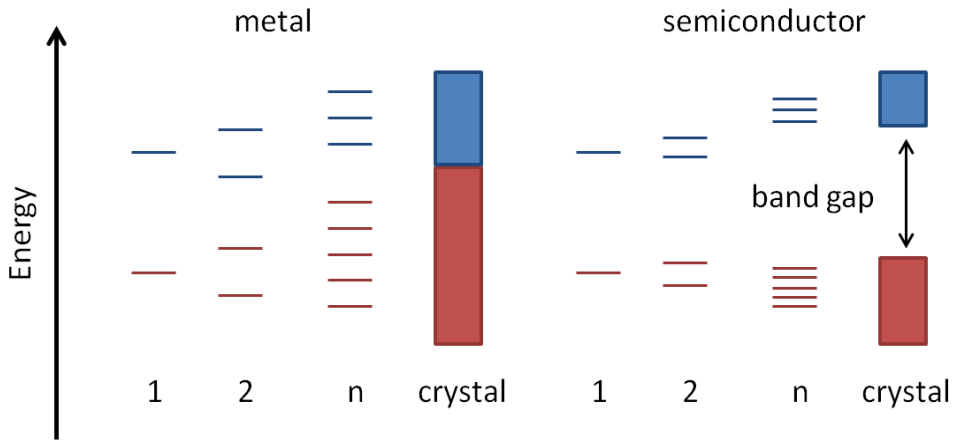

Figure 1.6: Nature of the band structure for a metal and a semiconductor.

The separation in energy (eV) between the two bands determine the type of material: metals - 0 eV, semimetals - less than 0.5 eV, semiconductors - between 0.5 and 3 eV, insulator more than 3 eV. When an electron is promoted from the VB to the CB, a positively charged vacancy remains in the VB. This vacancy is usually filled by the near electrons in the VB, moving the vacancy to the neighbour site. In the presence of an electric field this process can be repeated, resulting in a current represented by the movement of the vacancy in the opposite direction to the promoted electron. Since this vacancy results from a lack of negative charge (missing one electron), the relative current can be described as the current of positive *holes* in the VB. The electron and the relative hole are charges with opposite signs. Usually these two charges are considered independent one from the other, however in some conditions they can be interacting. In this particular conditions the Coulomb interaction, which is manifested between charges with opposite sign, bind the electron and the holes in a unique state called an *exciton*[11]. These excitons can be both stationary or mobile within the material. They result in a series of intra-band gap states slightly above the VB and below the CB. Although excitonic states are not relevant for electrons and holes in isolation, they are important for the optical properties of semiconductors.

1.3 Generation and Recombination Mechanisms

Generation is an electronic excitation event which increases the number of free carriers available to carry charge. Recombination is an electronic relaxation event that reduces the number of free carriers[12]. Generation is a process that requires energy; this energy can be provided by vibration (phonons), or light (photons). Recombination is a process that releases energy, with the inverse mechanisms of generation. For every generation process there is a recombination process.

In solar cells, the generation of charges from light absorption is called photogeneration. This process starts with the absorption of a photon and the promotion of an electron from the VB to the CB, creating an electron-hole pair. Recombination is the decay of the electron from the CB back to the lower state.

The absorption coefficient α describes how light is attenuated passing through the absorber material of the solar cell. Now, when the solar cell is illuminated, there is a flux

of photons (*I*) with energy *E* and intensity I_0. Part of this flux is absorbed through the absorber material according to the relative thickness *dx*. The absorbed part is given by:

$$\frac{dI}{dx} = -\alpha I \tag{5}$$

Integrating (5) gives with an uniform α the Lambert-Beer law (figure 1.7):

$$I(x) = I(0)e^{-\alpha x} \tag{6}$$

Where *I(0)* is the intensity just inside the surface.

If all of the photons are absorbed to generate free carriers, the rate of carrier generation per unit volume as a function of the depth *x* is:

$$g(E,x) = b(E,x)\alpha(E,x) \tag{7}$$

Where *b* is the photon flux at *x*. Notice that it is the number and not the energy of the photons which determines the generation rate.

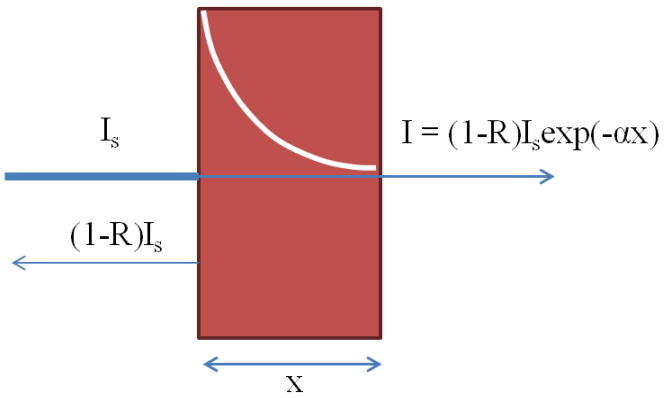

Figure 1.7: Attenuation of light intensity (white line) through the absorber material of the solar cell. The reflected part is taken into account in the balance of the final component. Photon flux density attenuates in the same way.

The importance of the importance of the number of photon respect to the energy carried must be noted (assuming the energy is higher than band gap, otherwise photons are not absorbed). Photons with an energy higher than band gap promote electron in the CB with an excess of energy (see figure 1.5) that is lost in a fast thermalization process, relaxing the electron in the minimum of the CB band. Microscopically, this energy is converted through collisions with the lattice to produce phonons. On the other hand, the number of photons is related to the number of excitation events that can occurs and so to the number of electrons promoted in the CB.

The term recombination is includes one or more mechanisms that reduce the number of mobile electrons and holes. There are two kind of recombination: unavoidable and avoidable.

1.3.1 Unavoidable recombination.

This mechanism is related to the intrinsic physical processes of the material. Radiative recombination and Auger recombination belong to this category (figure 1.8).

- Radiative recombination: this is one of the most important recombination mechanism in photovoltaics. Radiative recombination is the spontaneous emission of a photon from the recombination of an electron with a hole at the minimum/maximum of the CB/VB respectively. The energy of the emitted photon is equal to the band gap
- Auger recombination: this is the collision of two similar carrier (for example, electrons). In this non-radiative process one carrier transfers its kinetic energy to the other carrier. This leads to the decay of the first carrier in the VB and the promotion of the second carrier to high energy excited states before decaying and losing its energy in the form of phonons.

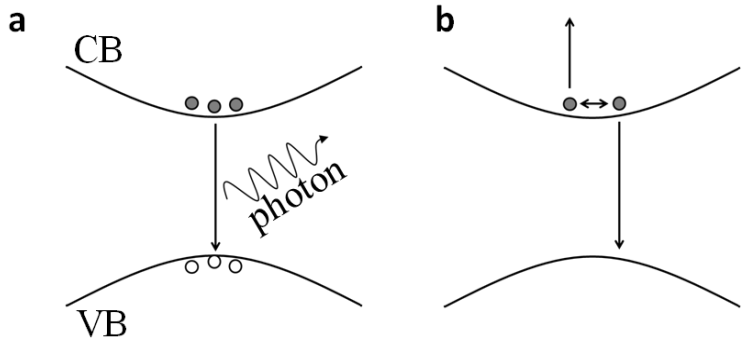

Figure 1.8: Unavoidable recombination mechanisms: radiative recombination (a), Auger recombination (b).

1.3.2 Avoidable recombination.

These mechanisms are related to defects and impurities in the material. Recombination through traps states and grain boundaries are a type of avoidable recombination (figure 1.9).

- Traps states: traps states are sub-band gap levels that act as a sink for both excited electrons and holes, like a potential well. These states act as recombination centres when the energy of the state lies deep within the band-gap such that recombination with the opposite carrier is much more likely than thermal detrapping back into the band. Otherwise electrons and holes can be de-trapped, resulting in a slower current.
- Grain boundaries recombination: surfaces and grain boundaries in polycrystalline films are defects rich zones. Localized states, like broken bonds or extrinsic impurities can create recombination centres like traps states, shortening the electron and holes capturing time.

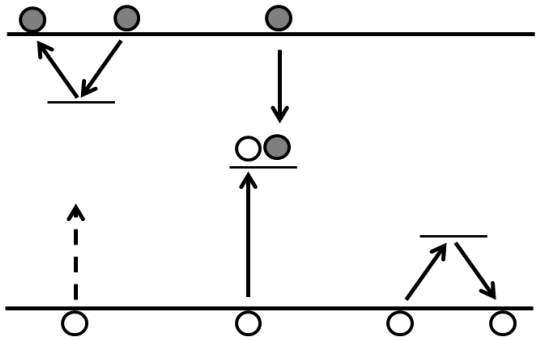

Figure 1.9: Avoidable recombination assisted by trap state. Recombination occurs only when both the electron an hole are trapped in the same site.

1.4 The Structure of Third Generation Solar Cells

The absorption of light and the generation of charges are two of the main process in the solar cell. Transporting them in a current is the third. To do this, a working solar cell needs an asymmetry which drives electrons and holes in different directions.

A *p*-*n* junction is the classic model of a solar cell. The junction is composed by a semiconductor with two zones doped *p* (thus with a deficiency of electrons) and *n* (thus with an excess of electrons), respectively. When the two zones are brought into contact, the valence and conduction bands of the two parts of the semiconductor bend. The difference between the two work functions generates an electric field within the junction which guides the charges photogenerated (figure 1.10).

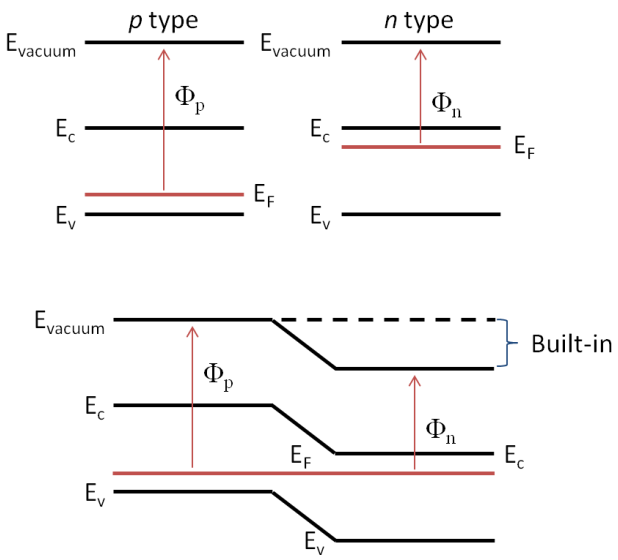

Figure 1.10: Energy band profiles for a *p-type* and *n-type* semiconductor. Bottom panel, the energy alignment for a *p-n* junction.

The way in which the junction is realized usually characterize the type of solar cell. Third generation solar cells use a variation of the Fermi level to generate an internal electric field (the built-in field) that drives the carriers in opposite directions. This field is generated by a potential step at the interfaces between the light absorber layer and two optimized material called extraction layers. This results in the bending of the VB and CB of the absorber layer across the interfaces with the two extracting layers in a similar way of what happen in the *p-n* junction. Now, when the device is illuminated the electrons and holes are separated by the built-in field and are transported to the opposite sides. This configuration differs from the classic *p-n* junction and is defined as *p-i-n* junction, where an intrinsic semiconductor layer (the *i-type* i.e. the photoabsorber material) is sandwiched between two layers intentionally doped to be *p-type* or *n-type*. The *p* layer presents a deep Fermi level and is responsible for the extraction of holes, the *n* layer on the opposite side presents a higher Fermi level and is responsible for the extraction of electrons. The built-in field generated by the *p* and *n* zones extends the electric field over the intrinsic semiconductor. Carriers that are photogenerated in the *i* region are then driven through the electric field to the respective contacts. The band profile for an ideal *p-i-n* junction are reported in figure 1.11.

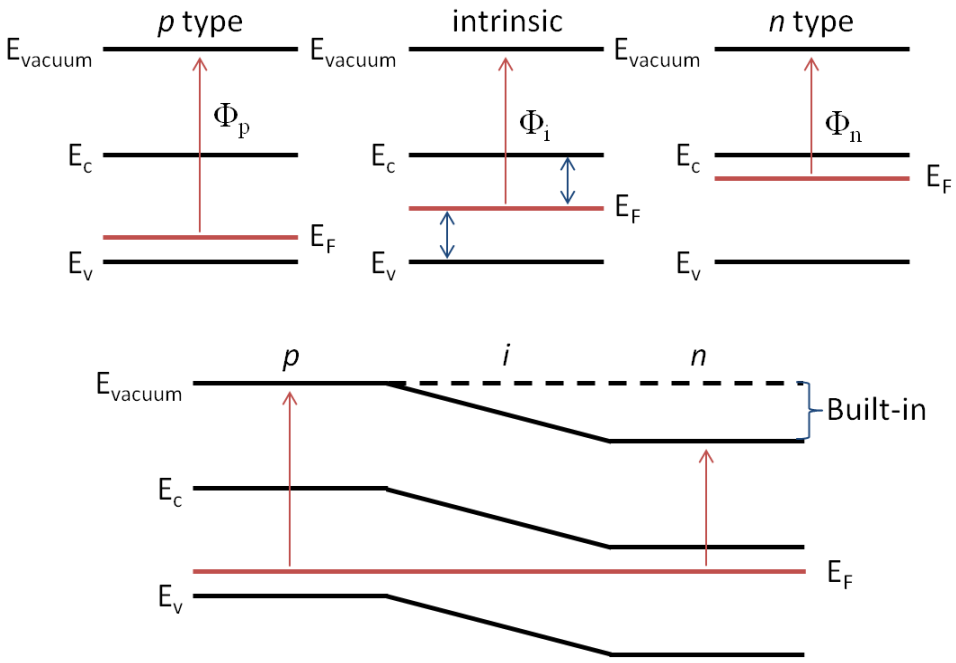

Figure 1.11: Band profile of a *p*, *i* and *n*-type semiconductors is isolation (top panel) and closed together in a *p-i-n* junction (bottom panel). E_F is the Fermi level, E_c, E_v the conduction and the valence band respectively while Φ represent the work function of the semiconductors.

One of the most important advantages of *p-i-n* junction solar cells is their simple structure. Almost all of these solar cells are comprised from four components: the active material, two selective interlayers, the electrodes.

1) The active layer. This is the core of the solar cell where light is absorbed and charges are generated. It can be composed by one semiconductor alone or two, either as a double layer or blended together.
2) An electron extraction layer. This layer is a material with appropriate energy levels: the conduction band is energetically close to the conduction band of the active layer and the valence band is deeper in energy respect to the valence band of the active layer. In this way this the extraction layer can collect the electrons that are photogenerated in the active material but not the holes.
3) An hole extraction layer. This layer works like the previous but with holes. The valence band is close to the valence band of the active layer and the conduction band is higher respect the conduction band of the active layer.
4) The electrodes are the terminals that connect the cell to the external circuit. This means that there are two electrodes: the top and the bottom. Since light is coming from one side of the cell, at least one of the two electrodes must be transparent.

With this configuration the charges are generated and collected according to a selective path. The energy levels of the two selective interlayers provides the built-in filed in the solar cell, which gives the driving force for the extraction of carriers.

1.5 Conclusions

This chapter has been dedicated to the introduction to the key concepts in photovoltaics. The fundamental characteristics of a solar cell obtained from the current/voltage characteristic have been thoroughly discussed along with the basic properties of semiconductors. The origin of the band gap and the introduction of the conduction and valence band are necessary concepts in order to understand the properties of novel solar cells. Photogeneration of carriers and their relative recombination mechanisms have been introduced to give an overview of the photophysical dynamics occurring within a photovoltaic device. Finally, a general description of a working third generation solar cell has been provided.

References

[1] - A. Luque, S. Hegedus, *Handbook of Photovoltaic Science and Engineering* **2003** Wiley-VCH.

[2] - P. Würfel, The Chemical Potential of Radiation J. Phys. C - Solid State Physics **1982**, 15, 3967.

[3] - M. A. Green, *Third Generation Photovoltaics* **2006**, Springer.

[4] - NREL Website: http://www.nrel.gov.

[5] - N.S. Sariciftci, L. Smilowitz, A.J. Heeger, F. Wudl *Science* **1992**, 258, 5087.

[6] - P. Stallinga, Electrical *Characterization of Organic Electronic Material and Devices* **2009** Wiley VCH.

[7] - A. Kojima , K. Teshima , Y. Shirai , T. Miyasaka , *J. Am. Chem. Soc.* **2009**, 131, 6050.

[8] - M. M. Lee, J. Teuscher, T. Miyasaka, T. N. Murakami, H. J. Snaith, *Science* **2012**, 338, 643.

[9] - P. Würfel, *Physics of Solar Cells* **2005**, Wiley-VCH, Weinheim.

[10] - J. Nelson, *The Physics of Solar Cells* **2004**, Imperial College Press.

[11] - P.T. Landsberg, *Recombination in Semiconductors* **1991** Cambridge University Press.

Chapter 2
Third Generation Solar Cells

The term “third generation” refers to the new technologies of photovoltaics that have arisen after the previous “first generation” - silicon wafers - and the “second generation” - thin films. Third generation solar cells are developed in order to outcome the limitations of previous photovoltaic generation: firstly, enhancing the power conversion efficiency limit; secondly, the reduction of high production costs. Under the conditions of detailed balance described by Shokley and Quiesser, the power conversion efficiency limit for a single junction solar cell is 33-34% under AM1.5 illumination. Multijunction solar cells avoid this limit by using several absorber layers to harvest light from different regions of the solar spectrum to minimise thermalization losses and have reached record efficiencies of more than 46%[1]. The problems with these devices are the extremely high manufacturing costs that relegate these solar cells to applications where other advantages, such as weight, are more important. On the other hand, emerging third generation solar cells have tried to reduce production costs using low cost processing techniques. Even if the efficiencies of these photovoltaics are lower compared to nowadays multijunction devices their possible exploitation in real world applications makes them appealing and has attracted a lot of interest. Leading this category there are organic photovoltaics and perovskite solar cells.

2.1 Organic Photovoltaics Solar Cells

Organic photovoltaics (OPVs) get their name from the nature of the light absorbing material, which is based on carbon. These solar cells belong to the category of excitonic solar cells which are characterized by the presence of bounded electrons-hole pairs (exciton) generated upon illumination (see introduction)[2]. The electrostatic interaction between the electron and the hole is relatively high due to the low dielectric constant of the organic materials used.

The stability of excitons in organic molecular systems is an obstacle to the generation of free charges, which occurs efficiently in other kinds of solar cells. In excitonic solar cells exciton dissociation occurs efficiently only in regions of an interface between two materials with different electron affinities: an electron-donor material (for simplicity called a donor) and an electron acceptor material (or simply an acceptor)[3]. The maximization of the area of these interfaces is an important consideration in the

deposition of these materials (figure 2.1). The concept of a bulk-heterojunction (BHJ) represents the ideal condition for this concept of photovoltaics[4]. Here the intermixing in separated phases of the donor and acceptor material increases the area of available interfaces, which maximizes the generation of free carriers. The photophysics of this system is based on highest occupied molecular orbital (HOMO) and lowest unoccupied molecular orbital (LUMO) of the donor and acceptor materials which, in terms of light absorption, are conceptually similar to the conduction and valence band in an inorganic semiconductor. The photophysics can be divided into four parts[5]:

1. Absorption of light and generation of excitons
2. Diffusion of excitons
3. Dissociation of the exciton and generation of the charges
4. Charges transport and collection

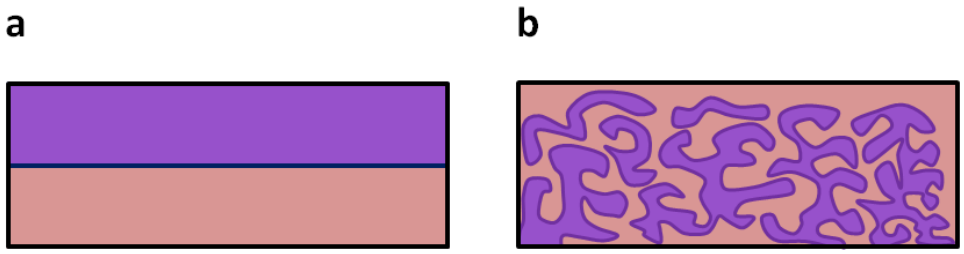

Figure 2.1: Difference between a bi-layer junction (a) and a bulk heterojunction (b).

Absorption of Light

Light is absorbed by the active layer of the solar cell. In particular, light is absorbed by the donor material (*D*), according to the relative absorption spectrum. This process promotes an electron from the HOMO level into the LUMO level, which results is an excited state in the donor phase (*D**)

$$D + h\nu \rightarrow D^*$$

The excited electrons in the LUMO leaves behind a hole in the HOMO. Due to the Coulomb interaction, these two charges are bond together forming an exciton.

Diffusion of Exciton

There are two types of excitons: Frenkel excitons and Wannier-Mott excitons. The difference between the two is based on the dielectric constant of the material, which reflects how tight the electron and hole are bound. Frenkel excitons are characterized by

a small dielectric constant and for this reason are localized in a narrow space (approximately on the same molecule)[6]. Wannier-Mott excitons on the contrary have a large dielectric constant and their radius extends over several crystalline units[7]. In OPVs the excitons formed are of the Frenkel type. Since many donor materials are comprised of conjugated bonds (for example π-conjugation both along polymer's chains or in molecular aggregates) the excitons can diffuse along the donor phase. During this stage the stability of the exciton is fundamental since geminate recombination of the electron-hole pair would prevent charge separation.

Dissociation of the exciton and generation of charges.

The binding energy of an exciton is the energy necessary to separate the electron and the hole. In Frenkel excitons this energy is around 1 eV[6]. In order to be separated the exciton must travel along the donor phase until the interface with the acceptor phase. The acceptor (*A*) is usually a material with a high electron affinity to separate the exciton into the free-charges. At the interface the exciton forms a transition state defined as charge transfer state (CT state - *[D - A]*)[8].

$$D^* + A \rightarrow [D - A]$$

This is a state with its own identity: the two charges are still bond by Coulomb interaction but their respective wavefunctions are localized on different molecules, giving the state an ionic character. If the electron and hole cannot be separated in the CT state they recombine. This is called geminate recombination. If the CT state doesn't recombine it further evolves, separating into free charges: the positive hole in the donor phase (D^+) and the negative electron in the acceptor phase (A^-).

$$[D - A] \rightarrow D^+ + A^-$$

Charge transport and collection

When the CT state splits, two independent free charges are formed. The Coulomb attraction is lost and the two carriers are allowed to drift in their respective phases. There are several mechanisms in this stage that can hamper the extraction of carriers: free charges can recombine with other free carriers non-geminately or they can thermalize into a closed domain of a donor/acceptor phase.

There are several types of donor/acceptor combinations. The choice of what materials are mixed together in the bulk heterojunction is based mainly on the energy levels of the two materials. To have efficient charge separation it is necessary that there is a positive difference in energy between the LUMO of the donor and LUMO of the acceptor, as shown in Figure 2.2. The alignment of the energy levels also determines the part of the internal field that separates the charges and the photovoltage obtained from the cell.

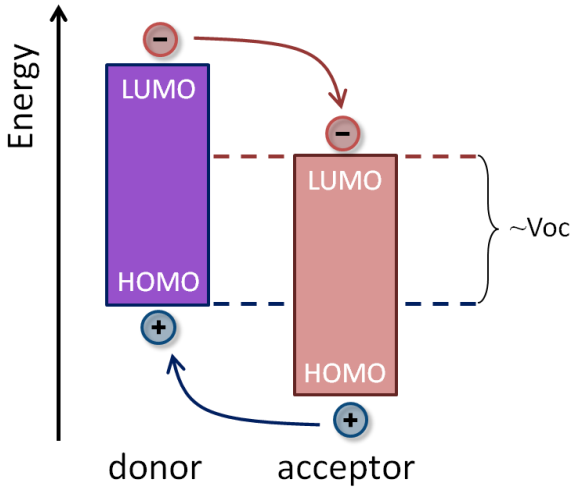

Figure 2.2: Diagram of the energy levels for a donor/acceptor junction. The electron transfer mechanism is also reported.

The most used donor material in BHJ devices is a semiconducting polymer: poly 3-hexylthiophene (P3HT). This polymer belongs to the family of thiophene polymers. These materials present good semiconducting qualities given a relatively simple synthesis. BHJ solar cells realized with P3HT have shown record efficiencies of 5.5% [4]. This respectable but low efficiency is mainly due to the absorption edge of P3HT that peaks at 560 nm. In this sense new polymers are the object of ongoing study directed towards exploiting the near-IR region of the solar spectrum. Low-band gap polymers like poly [2,6-(4,4-bis-(2-ethylhexyl) - 4H - cyclopenta [2,1-b; 3,4-b'] dithiophene) - alt - 4,7 - (2,1,3 - benzothiadiazole)] -abbreviated in PCPDTBT- are presenting interesting results [9]. Thanks to a reduced band gap this material is able to absorb almost the whole region of the visible spectrum, increasing the overall efficiency of the cells.

The acceptor material is usually a fullerene derivative: 6,6-phenyl-C61-butyric acid methyl ester (PCBM)[10]. Fullerene materials are suitable candidate acceptors because of their high electron affinity. Chemical functionalizations are necessary to improve the solubility of these compounds. P3HT, PCPDTBT and PCBM are represented in figure 2.3.

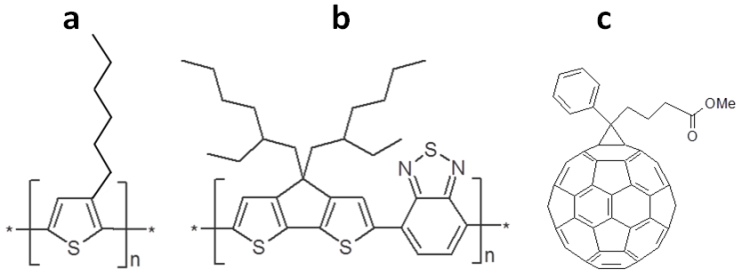

Figure 2.3: Schematic representation of P3HT (a), PCPDTBT (b) and PCBM (c).

For the extraction of electrons metal oxides are often used. Titanium Dioxide (TiO_2) and Zinc Oxide (ZnO) are suitable candidates thanks to their energy alignment with PCBM[11]. On the other side, for the extraction of holes the most used interlayer is poly (3,4-ethylenedioxythiophene)-poly (styrenesulfonate) - abbreviated as PEDOT:PSS - a polymer mixture of two ionomers with an elevated conductivity[12].

The structure with the energy levels of a standard organic BHJ solar cell is reported in figure 2.4.

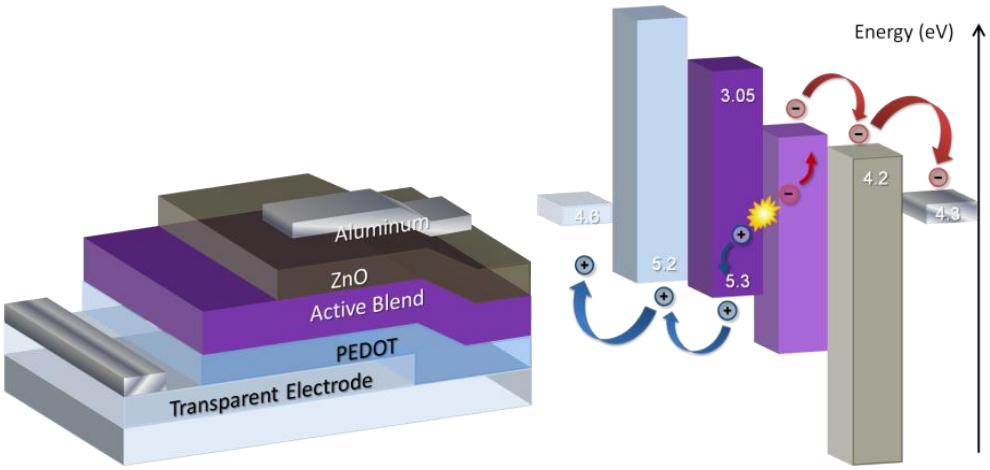

Figure 2.4: Structure and energy level for a standard BHJ solar cell. The active blend is composed by the intermixed phases of the donor and acceptor materials.

2.2 Perovskite Solar Cells

Perovskite Solar Cells (PSC) represent a new concept and design with respect to conventional third generation photovoltaics. These devices are a legacy of Dye-Sensitized Solar Cells (DSSC) that were first demonstrated with high efficiency by Micheal Gratzel and Brian O'Regan in 1990[13]. DSSCs implement an organic semiconductor (a dye) by sensitizing a metal oxide anode that can be regenerated with an iodide electrolyte in liquid version, or a solid state hole extraction layer that is typically a small organic molecule. Basically, these devices act as photoelectrochemical

systems. In order to increase the interaction between the photo-anode and the dye these devices implemented mesostructured configuration of the photo-anode. The first prototype of PSC was realized with the structure of a liquid DSSCs in 2009 with the perovskite absorber replacing the conventional dye[14]. The name "perovskite" is given for the crystalline structure of the absorber material: ABX_3. This material is conceptually an hybrid organo-lead halide compound obtained from a relative simple synthesis and deposited through conventional solution processed techniques[15]. In figure 2.5 is reported the structure of the perovskite with the relative XRD spectrum.

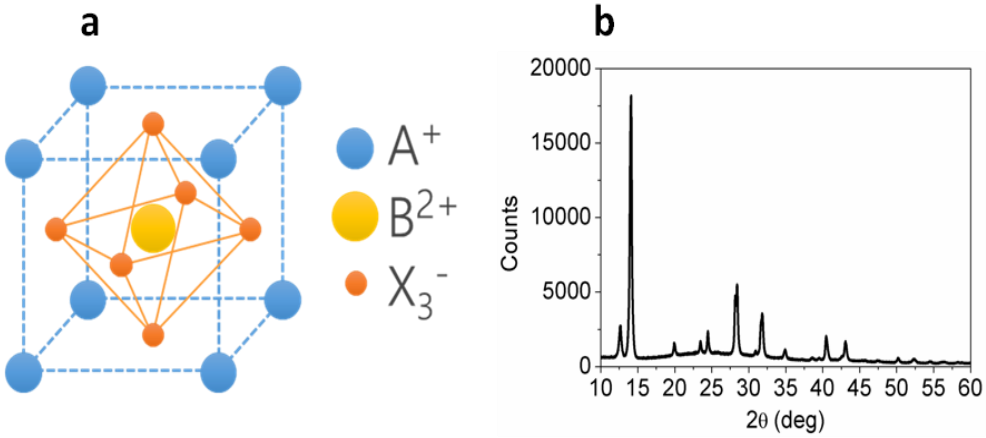

Figure 2.5: a) Structure of a perovskite ABX3. In photovoltaic applications $A^+ = CH_3NH_3^+$, $B^{2+} = Pb^{2+}$, $X^- = I^-$. b) XRD spectrum of a perovskite thin film.

The organic part of the material is an amine derivative, the inorganic part is a lead halogen compound. For photovoltaic applications the most used combination of the two is methylammonium iodide (CH_3NH_3I abbreviated with MAI) as organic precursor and lead Iodide (PbI_2) as a lead salt[16-19]. The resultant material is methylammonium lead iodide perovskite ($CH_3NH_3PbI_3$) also called $MAPbI_3$. The perovskite is realized through a two-step process[20]. The first step is the synthesis of the MAI. This is an acid-base reaction between methylamine and hydroiodic acid. The reaction is performed in an excess of methylamine that is subsequently removed in a series of washing cycles in ethanol[15]:

$$CH_3NH_2 + HI \rightarrow CH_3NH_3I$$

The second step is the reaction of the MAI with the PbI_2. This second step is quite delicate and strongly influences the perovskite formation. The way in which the organic precursor and the lead salt react can be realized with different techniques. The common

concept is that the perovskite formation is a crystallization process with similar characteristics to self-assembling mechanisms. The lead salt and the organic precursor can be dissolved together in a polar solvent (usually dimethylformimide DMF), the obtained yellowish solution is then deposited through solution processed techniques. The crystallization process starts with a thermal treatment that removes the solvent and change the colour of the deposited film from yellowish to dark brown. This process is defined *one-step deposition* and was used in the first embodiment of PSC[21]. The problem of this technique was the poor morphology obtained for the perovskite films. Soon, new techniques were developed in order to enhance the quality of the perovskite layer. The most successful among these is the two-step deposition. In this process the PbI_2 and the MAI are deposited from solutions subsequently. Firstly, the lead salt is dissolved in DMF and deposited on the substrate. Secondly, when the lead iodide film is dried, a solution of MAI dissolved in isopropyl alcohol (IPA) is used to convert the lead iodide film into perovskite. This step can be realized in very different ways: dipping the lead film into the MAI solution[20], spin-coating the solution MAI on top of the lead film[22] or exposing the lead film to MAI vapours[23]. All these methodologies result in perovskite formation with different morphologies (figure 2.6).

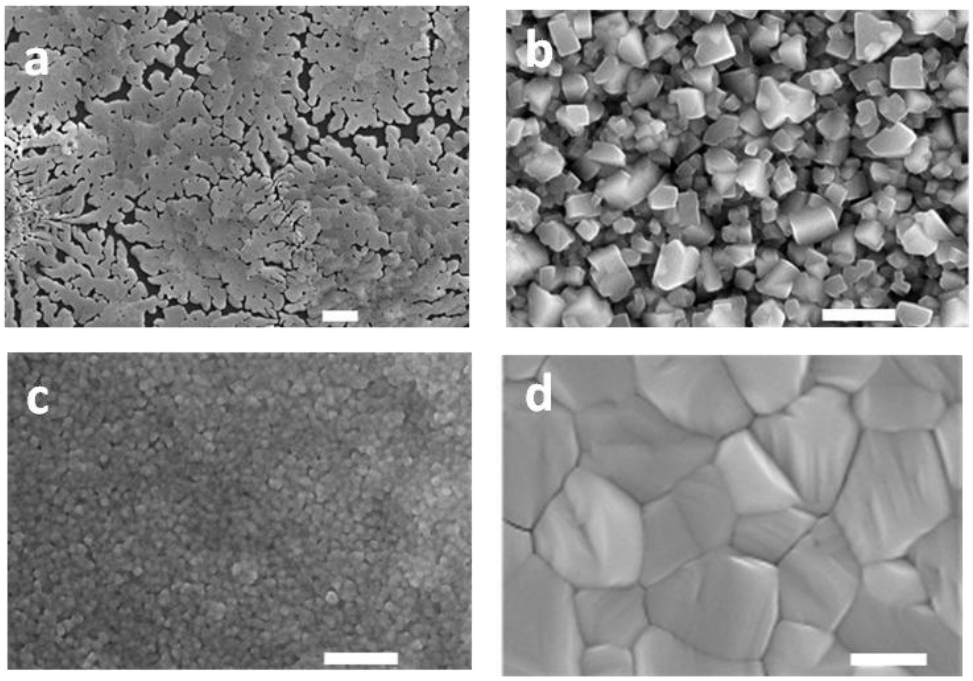

Figure 2.6: Scanning electron microscopy (SEM) top view of perovskite film deposited from different techniques: a) one step deposition, b) two step by dipping, c) two step spin coating, d) two step vapour assisted. Scale bar is 10 µm (a), 1 µm (b, c) and 500 nm (d).

$MAPbI_3$ is the most used perovskite in solar cells and this is due to the high efficiencies reported in several publications[15-19]. However, by changing the starting reagents it is possible to obtain perovskites with different properties. Iodine can be substituted with other halogens (bromine and chlorine) and the methylammonium can be replaced with formamidinium. Hybrid perovskites can be realized by mixing different reagents as methylammonium and formamidinium ($HC(NH_2)_2$)[24] or a mixture of halogens such as bromine/iodine or chlorine/iodine, for example[25]. Finally, cesium can replace the organic cation to form fully inorganic perovskite[26]. The different combination of reagents to form halide perovskite are reported In Table 2.1.

	Chloride	**Iodide**	**Bromide**
		$MAPbI_{3-x}Cl_x$	$MAPbBr_{3-x}I_x$
Methylammonium	$MAPbCl_3$	$MAPbI_3$	$MAPbBr_3$
		$(FAPbI_3)_{1-x}(MAPbBr_3)_x$	
Formamidinium	/	$FAPbI_3$	/
Cesium	$CsPbCl_3$	$CsPbI_3$	$CsPbBr_3$

Table 2.1: Metal-halogen perovskites. MA is referred to CH_3NH_3, FA to $HC(NH_2)_2$. Gray squares highline hybrid perovskites.

The photophysics of PSC is still an open point of discussions. Many works and reports tried to assign conventional or new mechanisms for the generation of carriers upon illumination. The starting point for the comprehension of the photophysics is to understand the optical properties of perovskite. The absorption spectrum of $MAPbI_3$ is reported in figure 2.7. With a band edge at 780 nm this perovskite is able to absorb all of the visible spectrum. This strong optical absorption is one of the key characteristics for a photovoltaic material. It reduces the required thickness of the film, avoiding transport and recombination. From the absorption spectra and theoretical calculation it has been determined that the perovskite is a direct band gap semiconductor[27]. The edge of the spectrum defines a band gap of 1.6 eV which is one of the most suitable values for photovoltaic applications. If the iodide is replaced by bromide the band edge blue-shifts to 560 nm, and out to 350 nm if the chloride is used instead[28]. This shift of the absorption is correlated to the opening of the band gap. Upon illumination photocarriers are generated within the perovskite. If these photocarriers are not

collected or extracted they recombine radiatively under ideal conditions, emitting a photon. The photoluminescence (PL) of the perovskite is caused by the radiative recombination of photoinduced carriers[29].

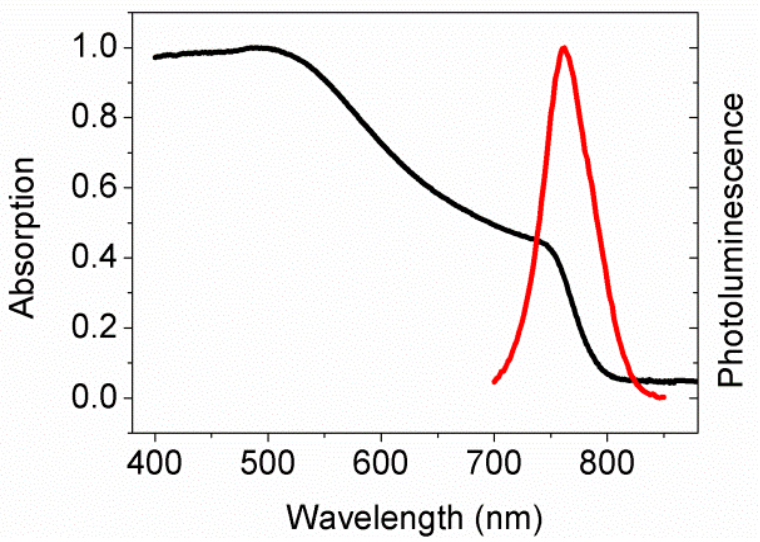

Figure 2.7: Absorption (black) and photoluminescence spectrum for a thin film of $MAPbI_3$.

The first studies attempted to classify the charge generation in perovskite with a pure excitonic mechanism[30], with bound electron and hole pairs providing the primary photoexcitation. More recent investigations have put forward a different scenario, where photoexcitation leads mainly to the generation of free electrons and holes, similar to the case of conventional polycrystalline inorganic semiconductors[31]. $MAPbI_3$ crystallites, with a small grain size (tens of nanometres), do not support exciton states even at low temperature. In contrast, in hundreds of nanometre-sized domains, free carriers may thermalize and coalesce into the 'exciton state', depending on the temperature and excitation density. Similar behaviour is also observed for the higher-band gap $MAPbBr_3$. Thus, a definitive classification - "excitonic" or "free carrier" semiconductor- as well as a universal value for the exciton binding energy in semiconductors presenting the same chemical composition is not possible for hybrid perovskites as both regimes are physically accessible by appropriately processing the compounds. In conclusion, upon illumination the perovskite absorber is able to generate charges directly or from exciton dissociation, depending on the dimension of the crystallites. However once the photocarriers are generated, the perovskites itself is able to transport them (both the electron and the hole) following the direction of the built in field. The transport of the charges is another important quality of the perovskites.

Charges are able to travel along the whole thickness of the absorber layer mainly due to the extremely low non radiative recombination rates (compared to other poly crystalline films). This property is reflected in the extremely high open circuit voltage which is almost coincident with the effective band gap potential[32].

Nowadays the conventional PSC is made in the configuration of thin-film solar cells (see chapter 1). The perovskite absorber is sandwiched between two extraction layers that contribute to the built in field for the extraction of charges. Nevertheless the very first devices used the DSSC configuration in which the perovskite was replacing the organic dye[15]. In this design the extraction of electrons occurs at the interface between a mesoporous scaffold of titanium dioxide (TiO_2) and the dye. In order to extend these interfaces a mesoporous scaffold of TiO_2 are used. Snaith et al. demonstrated that the mesoporous scaffold of TiO_2 could be replaced with a dielectric Al_2O_3 scaffold[15]. The presence of a dielectric material prevents the injection of the charges into the scaffold forcing the perovskite to transport them between the whole layer up to the extraction barriers. In this way it is possible to remove the mesoporous scaffold and realize solar cell in planar configuration, using thicker layer of perovskite that means more light can be absorbed[33].

PSCs can be divided in two main categories: mesoporous and planar. Mesoporous devices are realized on top of a transparent electrode (usually Fluorinated-Tin Oxide, FTO) covered by a thin layer of TiO_2 (usually 80 nm) which is the base of the electron extraction layer. This layer is obtained through different techniques that involve, for example, high temperature treatment in order to convert titanium isopropoxide in TiO_2. The mesoporous scaffold is deposited in the form of nanoparticles of the same diameter (from 20 to 50 nm) to give homogeneous porosity. It can be injecting (TiO_2) or not injecting (Al_2O_3), as shown in figure 2.8b. The perovskite precursors are deposited inside the scaffold - both in the one step or two step deposition. The solution fills the pore of the scaffold and during the thermal treatment forms small crystallites with a constrained growth. On top of the mesoporous scaffold the amount of solution left forms a layer of big crystals called the “capping layer”. The overall thickness of the mesoporous scaffold is 600 nm (300 nm scaffold and 300 nm the capping layer). The hole extraction layer is mostly a small organic molecule (2,2’,7,7’-tetrakis-(N,N-di-p-ethoxy phenylamine) 9,9’-spirobifluorene), SPIRO-OMeTAD. Some studies have investigated whether it is possible

to replace SPIRO-OMeTAD with other organic materials like polymers or metal oxides, but up to now SPIRO-OMeTAD is still the most efficient choice. The lateral sketch of a mesoporous device is reported in figure 2.8a.

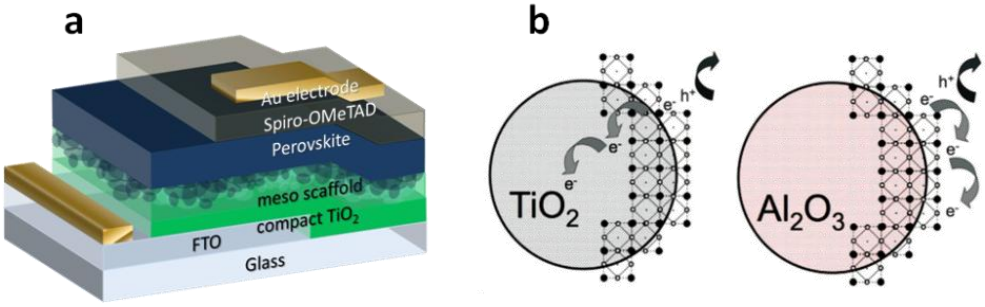

Figure 2.8: a) Architecture of a mesoporous perovskite solar cell. b) The difference in terms of injection for a mesoporous TiO_2 or Al_2O_3, taken from [15].

The planar configuration, on the contrary, does not employ a mesoporous scaffold and uses a flat layer-by-layer stacking. This category of solar cells can be divided in two subsets: standard and inverted. Standard devices are very similar to mesoporous PSC, the difference is the absence of the mesoporous scaffold. Since it has been demonstrated that the interface between perovskite/electron extraction layer is not fundamental for the generation of carriers, the planar configuration simplifies the realization of the devices and, with the tuning of the deposition techniques, increases the quality of the films. On the other hand, the inverted configuration uses similar interlayers to OPVs[17]. The hole transport layer is PEDOT:PSS and is deposited on top of the transparent electrode. The PEDOT:PSS layer is resistant to the solvents present in the perovskite solution and allows film formation (it is not possible to deposit the perovskite solution onto SPIRO-OMeTAD). The electron extraction layer is a film of PCBM deposited on top of the perovskite. Due to the high reactivity of PCBM anions, a layer of metal oxides nanoparticles like Zinc Oxide (ZnO) or TiO_2 are often used to protect the layer from degrading agents (see chapter 3)[17]. The definition of Standard and Inverted designs is a convention based on the direction of the photocurrent. In figure 2.9 are summarized the architecture of planar Standard and Inverted PSC.

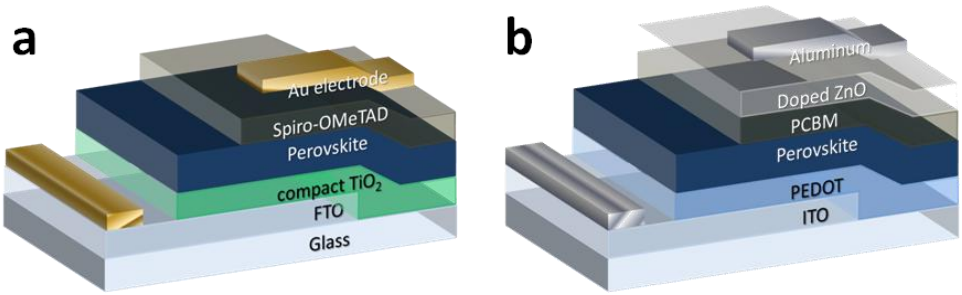

Figure 2.9: Different configuration of planar PSC. a) Standard, b) Inverted.

2.3 Stability of the Devices

Increasing the power conversion efficiency is the most challenging issue for the development of solar cells. However, apart from this need, the stability of devices is an essential challenge to be overcome before solar cells can be developed as commercial products. There are two ways to study the stability of the solar cells. The first case consists of running tests of durability. These tests can be linear over time, and thus very long, or accelerated by increasing the temperature/pressure conditions. These tests are expensive from an economical and temporal point of view and therefore, in general, are carried out on devices that are already optimized. The second case consists in the study of the physical processes of degradation. Understanding the mechanisms that lead to the deterioration of the solar cell allows new materials that are stable over time to be studied, saving resources.

Organic Photovoltaics are sensitive to UV-light and oxygen exposure due to the presence of π-conjugated semiconductors which leads to rapid degradation of the photoactive blend if not carefully protected. In this sense barriers and extra-layers are used to seal the devices. To maintain the exclusive properties of the OPVs (such as flexibility, transparency, light weight and so on) the cost of these barriers is quite high, affecting the overall technology. This engineering process can be resolved by a complete understanding of the degrading mechanisms that affects OPVs and then by tuning the synthesis of new material with satisfactory properties in terms of efficiency and stability over time.

The stability of metal halide perovskite is almost a new field of research. Preliminary studies have shown that the material is not stable upon exposure to moisture due to its ionic nature: water can convert the perovskite structure back to the precursors. This

effect is even accelerated in presence of an electric field applied. Moreover, the electrical stability of PSC is still under debate. Strange hysteretic behaviour in the current/ voltage characteristics has suggested a sort of electrical instability that is reflected in the drop of the photocurrent over time. Understanding the mechanisms behind these problems is mandatory in order to exploit PSCs in real world applications.

References

[1] - M. A. Green, *Third Generation Photovoltaics* **2006**, Springer.

[2] - B. C. Thompson and J.M.J. Frechet, *Angew. Chem. Int. Ed.* **2008**, 47, 58-77.

[3] - G. Dennler, M. C. Scharber and C. J. Brabec, *Adv. Mater.* **2009**, 21, 1-16.

[4] - C. Brabec, V. Dyakonov, U. Scherf, *Organic Photovoltaics Materials, Device Physics and Manufacting Technologies* **2008** Wiley-VCH**.**

[5] - G. Lanzani, *The Photophysics behind the Phopovolthaics and Photonics* **2012**, Wiley- VCH.

[6] - Frenkel, *J. Physical Review* **1931**, 37, 17.

[7] - Wannier, G. Physical Review 1937, 52, 191.

[8] - Braun, C. L. *Journal of Chemical Physics* **1984**, 80, 4157.

[9] - D. Di Nuzzo, A. Aguirre, M. Shahid, V.S. Gevaerts, S.C.J. Meskers and R.A.J. Janssen, *Adv. Mater.* **2010**, 22, 4321.

[10] - F. B. Kooistra, V. D. Mihailetchi, L. M. Popescu, D. Kronholm, P. W. M. Blom, J. C. Hummelen, *Chemistry of Materials* **2006**, 18, 3068.

[11] - M. Gratzel, Nature, **2001**, 414, 338.

[12] - A. Elschner, S. Kirchmeyer, W. Lovenich, U. Merker, K. Reuter, *PEDOT Principles and Applications of an Intrinsically Conductive Polymer* **2011**, CRC Press

[13] - B. O'regan, M. Gratzel, *Nature*, **1991**, 353, 737.

[14] - A. Kojima , K. Teshima , Y. Shirai , T. Miyasaka , *J. Am. Chem. Soc.* **2009**, 131, 6050.

[15] - M. M. Lee, J. Teuscher, T. Miyasaka, T. N. Murakami, H. J. Snaith, *Science* **2012**, 338, 643.

[16] - M. Liu, M. B. Johnston, H. J. Snaith, *Nature* **2013**, 501, 395.

[17] - P. Docampo, J. M. Ball, M. Darwich, G. E. Eperon, H. J. Snaith, *Nat. Commun.* **2013**, 4, 2761.

[18] - J. M. Ball, M. M. Lee, A. Hey, H. J. Snaith, *Energy Environ. Sci.* **2013**, 6, 1739.

[19] - J.-H. Im, I.-H. Jang, N. Pellet, M. Grätzel, N.-G. Park, *Nat. Nanotechnol.* **2014**, 9, 927.

[20] - J. Burschka, n. Pellet, S.J. Moon, R.H. Baker, P. Gao, M. K. Nazeeruddin, M. Gratzel, *Nature,* **2013**, 499, 316.

[21] - G.E. Eperon, V.M. Burlakov, P. Docampo, A. Goriely, H.J. Snaith, *Adv. Funct. Mater.* **2014**, 24, 151.

[22] - Z. Xiao, C. bi, Y. Shao, Q. Dong, Q. Wang, Y. Yuan, C. Wang, Y. Gao, J. Huang *Energy Environ. Science* **2014**, 7, 2619.

[23] - Q. Chen, H. Zhou, Z. Hong, S. Luo, H.S. Duan, H.H. Wang, Y. Liu, G. Li, Y. Yang, *J. Am. Chem. Soc.* **2014**, 136, 622.

[24] - N.J. Jeon, J.H. Noh, W.S. Yang, Y.C. Kim, S. Ryu, J. Seo, S.I. Seok, *Nature*, **2015**, 517, 476.

[25] - Y. Zhao, K. Zhu, *J. Phys. Chem. C*, **2014**, 118, 9412.

[26] - G.E. Eperon, G.M. Paternò, R.J. Sutton, A. Zampetti, A.A. Haghighirad, F. Cacialli, H.J. Snaith, *J. Mater. Chem. A* **2015**, 3, 19688.

[27] - P. Umari, E. Mosconi, F. De Angelis, *Sci. Rep.* **2014**, 4, 4467.

[28] - Q.A. Akkerman, V. D'Innocenzo, S. Accornero, A. Scarpellini, A. Petrozza, M. Prato, L. Manna, *J. Am. Chem. Soc.* **2015**, 32, 10276.

[29] - S. D. Stranks, G. E. Eperon, G. Grancini, C. Menelaou, M. J. P. Alcocer, T. Leijtens, L. M. Herz, A. Petrozza, H. J. Snaith, *Science* **2013**, 342, 341.

[30] - A. Marchioro, J. Teuscher, D. Friedrich, M. Kunst, R. van de Krol, T. Moehl, M. Gratzel, J.E. Moser, *Nature Photon.* **2014**, 8, 250.

[31] - F. Deschler, M. Price, S. Pathak, L.E. Klintberg, D.D. Jarausch, R. Higler, S. Huttner, T. Leijtens, S.D. Stranks, H.J. Snaith, M. Atature, R.T. Phillips, R.H. Friend *J. Phys. Chem. Lett.* **2014**, 5, 1421.

[32] - H.J. Snaith, *J. Phys. Chemm. Lett.* **2013**, 4, 3623.

[33] - J. M. Ball, M. M. Lee, A. Hey, H. J. Snaith, *Energy Environ. Sci.* **2013**, 6, 1739.

Chapter 3
Experimental Methods

This chapter is dedicated to the description of the methods and investigation techniques used in the development of the experiments of this thesis. In particular, in the first part the optical and magnetic spectroscopy techniques that were used are described, both in steady state and time resolved versions. The second part regards the preparation of the samples and photovoltaic devices both for the Organic Photovoltaics part and for the Perovskite-based solar cells. Finally, the third part describes techniques used in the electrical characterization of solar cells that are produced during the research work.

3.1 Optical Techniques

3.1.1 Absorption Spectroscopy

All the absorption spectra presented in this thesis are recorded using a commercial UV-VIS-NIR spectrophotometer (PerkinElmer Lambda 1050 model) with a spectral resolution of about 1 nm, together with an integrating sphere module. The Optical Density (OD) is evaluated according to:

$$I_T = (I_0 - I_R)10^{-OD*d}$$

where I_T, I_0 and I_R are the transmitted, impinging and reflected light respectively, while d is the sample thickness. The spectra are corrected for substrate absorption with the appropriated baseline.

Transient Absorption Spectroscopy

The pump excitation is provided by a HeNe laser at 632 nm modulated by a mechanical chopper. A 8 mm diameter laser beam is realized using a telescope in order to guarantee a good overlap with the probe beam. The probe is generated from a 100 W halogen lamp. The changes in transmission under photoexcitation are detected using a silicon photodiode and measured using a lock-in amplifier referenced to the modulation frequency in order to measure the signal in phase and out of phase with respect to the laser pump. The signal is then normalized to the un-modulated transmission for every wavelength ($\Delta T/T$), from which the differential optical density is calculated. The samples

can be measured both in a vacuum chamber filled with nitrogen or in air, according to the experimental conditions.

3.1.2 Photoluminescence

For the steady state photoluminescence a commercial spectrofluorimeter (HORIBA Jobin Yvon Nanolog) has been used. A 450 W Xenon short-arc lamp coupled with a single-grating excitation and emission monochromator is used to excite the sample. The emission spectra are collected using a VIS Si-based (400–800 nm) and IGA-020 near-IR solid-state photodiodes (800–1500 nm).

Time Resolved Photoluminescence

Time-resolved fluorescence measurements are performed using a femtosecond laser source and streak camera detection system (Hamamatsu C5680). An unamplified Ti:Sapphire laser (Coherent Chameleon Ultra II) operating at 80MHz is tuned to provide pulses with central wavelengths of 960 nm, energies of 50 nJ, and temporal and spectral bandwidths of 140 fs and 5 nm, respectively. A b-barium borate crystal is used for type I phase-matched second harmonic generation, leading to pulses with central wavelengths of 480 nm. Measurements uses a linear voltage sweep module with 1 MHz repetition rate excitation, achieved through the use of an acusto-optical modulating pulse picker (APE Pulse Select), yielding a maximum temporal resolution of 50 ps.

As for the Absorption Spectroscopy the samples can be measured both in the same conditions of inert atmosphere or ambient conditions.

3.1.3 Raman Spectroscopy

The Raman analysis is carried out with a micro Raman system based on an optical microscope (Renishaw microscope, equipped with 5x, 20x, 50x and 100x short and long working distance microscope 3 objectives) used to focus the excitation light and collect it in a back scattering configuration, a monochromator, notch filters system and a charge coupled detector. The sample are mounted on a translation stage of a Leica microscope.

The excitation used consists of a diode laser at 532 nm. The system is calibrated against the 520.5 cm^{-1} line of an internal silicon wafer. The final data are collected over ten accumulations in order to maximize the signal to noise ratio. The measurements are conducted at room temperature and in air. The laser power intensity is in the order of 300 μW to avoid any sample degradation effects.

3.1.4 Scanning Electron Microscopy

Scanning Electron Microscopy (SEM) pictures are recorded using an high vacuum tungsten filament commercial Jeol 6010-LV, with a working bias of 15 kV.

3.1.5 Magnetic Spectroscopy

The Electron Paramagnetic Resonance (EPR) investigation is carried out both in steady state and time-resolved versions using a custom modified Bruker ER200D X-band spectrometer equipped with a nitrogen flow cryostat for sample temperature control. Light-Induced EPR (LEPR) spectra are obtained by subtracting the EPR spectrum recorded before illuminating the sample from the spectrum recorded under illumination of the sample. A 300 W Xenon lamp, IR filtered and focused onto a quartz optical fiber, is used as the source of photoexcitation, delivering about 100 mW/cm^2 to the sample. Time-resolved EPR (trEPR) experiments are performed with an extended detection bandwidth (6 MHz) and direct detection of the signal without magnetic field modulation. Sample photoexcitation is obtained using the second harmonics of a pulsed Nd:YAG laser Quantel Brilliant, l = 532 nm, pulse length = 5 ns; E/pulseD5mJ, 50 Hz repetition rate. The EPR direct-detected signal is recorded using a LeCroy LT344 digital oscilloscope, triggered by the laser pulse. The overall response time of the instrument is about 150 ns. At each magnetic field position, an average of 200 transient signals are usually recorded. All the trEPR and LEPR spectra if not otherwise reported are recorded at °T = 120 K. Spectral simulations are carried out using Easyspin, a Matlab toolbox.

3.2 Devices and Samples Realization

3.2.1 Organic Photovoltaics

Samples realized for optical investigation are thin films of PCPDTBT (Mw = 55.7 kg/mol, PD = 2.28) and PCPDTBT/PCBM deposited on glass trough doctor blade technique in inert conditions. PCPDTBT is provided by Belectric OPV, PCBM is purchased from Solenne. The films are prepared from 1% (w/v) polymer solutions in chlorobenzene (CB), respectively. Blend films are processed from analogous solutions (same solvents and polymer concentrations) with PCBM in the optimized ratio of 1 : 3.6. Prior to polymer deposition, the substrates are cleaned for 15 min in acetone and 15 min in 2-propanol using an ultrasonic bath. After deposition, the samples are annealed in a nitrogen atmosphere at 70 °C for 15 min.

For the magnetic investigation, PCPDTBT and PCPDTBT:PCBM blend films are deposited on quartz tubes (4 mm diameter) from the relative solution (1mg/ml for the pristine polimer, 1:2 by weight for the PCPDTBT:PCBM blend, in CB). The solvent is eliminated from the solutions in the tubes by slow (about 30 min) evaporation under vacuum and finally the tubes are flame sealed under vacuum ($<10^{-3}$ mbar). Spin-coated samples are prepared by depositing a solution of PCPDTBT:PCBM (1:2 by weight, 10 mg/ml each component) onto pre-cleaned plastic substrates of PET and successively insert into quartz tubes.

3.2.2 Perovskite Solar Cells

The synthesis of the organic precursor (Methylammonium Iodide) for the realization of the perovskite follows a well established procedure. Methylamine (from Sigma-Aldrich) solution at 33% in ethanol reacts with Hydroiodic acid (57% containing stabilizer - in water). The reaction is lead in an excess of Methylamine with the adding of ethanol to the reaction flask. The solution is dried using a rotary evaporator in order to obtain a with salt (Methylammonium Iodide - MAI). MAI is then processed according to the type of perovskite desired or to the deposition techniques used. For solar cells and samples

used in this thesis, MAI is dissolved in N,N -Dimethylformamide (DMF) in a 3:1 molar ratio with $PbCl_2$ (from Sigma Aldrich). All the perovskite depositions are realized through spin coating the precursors solution and annealing the films in nitrogen atmosphere. Samples for optical characterization are covered by a layer of Polymethyl methacrylate (PMMA 80 mg/ml from CB) in order to provide a 500 nm thick barrier. For Standard solar cells the TiO_2 compact layer is realized from spin coating a solution of Titanium Isopropoxide (369 µl of titanium isopropoxide in 2.53 mL of 2-propanol with 35 µl of 2 M HCl) directly on top of Fluorine doped Tin Oxide (FTO)-covered glasses after a previous cleaning cycle with distilled water, acetone, isopropanol (IPA), and oxygen plasma. The TiO_2 precursors are dried in air at 500 °C for 1h. The final thickness of the TiO_2 compact layer is about 80 nm. The mesoporous scaffolds of Al_2O_3 (Sigma Aldrich) or TiO_2 (Dyesol) nanoparticles are deposited directly on top of the TiO_2 compact layer with a final thickness of 300 nm. PEDOT:PSS (Clevios 4083) is deposited on clean Indium Tin Oxide (ITO) substrates with a final thickness in of 50 nm. The perovskite solution is deposited at 2000 rpm for 1 min and annealed at 90 °C for 90 min for the flat substrates and annealed at 100 °C for 60 min for mesoporous scaffolds, with the exception of ZnO scaffold where an annealing over 1 min is degrading for the quality of the films. The hole extracting layer SPIRO-OMeTAD is processed according to previous methods with the addition of tert-butyl pyridine and bis-(trifl uoromethane) sulfonimide lithium salt (Li-TFSI, Sigma Aldrich) in a final concentration of 100 mg/ml in CB. PCBM (NanoC) is dissolved in anhydrous CB (30 mg/ml) and for the inverted devices is covered by a layer of Al-doped ZnO nanoparticles in isopropanol (Nanograde). Gold and aluminum electrodes are evaporated in vacuum at 1×10^{-6} mbar.

Lateral perovskite devices for poling investigations are realized on top of gold and silver electrodes. The electrodes are realized on pre-cleaned glass substrates by a standard lithography lift-off process. The thickness of the electrodes is 15 nm and the length of the channel is 20 µm. The perovskite deposition is the same as for the solar cells. The PCBM films for the doping investigation are realized by adding to a solution of PCBM (30 mg/ml in CB) MAI (10 mg/ml in 2-propanol) in a 30:1 ratio. The solution is deposited in a nitrogen atmosphere.

Thin-film field-effect transistors are composed by 35 nm thick Au source and drain contacts, on top of a 1.7 nm thick Cr adhesion layer, realized on a thoroughly cleaned

low alkali 1737F Corning glass substrate through a standard lithographic lift-off patterning process. Contacts for single transistors have a channel width to length ratio (W/L) of 10 000 µm/20 µm.

Before the semiconductor deposition, substrates are rinsed with acetone and 2-propanol. PCBM and the PCBM:MAI 30:1 solutions are both deposited in a nitrogen atmosphere from a 30 mg/ml (CB and CB/IPA) solution by spin-coating to obtain a ~40 nm thick film. The semiconductor film is then annealed at 90 °C for 20 min to guarantee solvent drying. Cytop

CTL-809M 9 % w/v solution (AGC Chemicals Europe) is adopted as the dielectric layer. A thickness of 600 nm is optimized by spinning at 4000 rpm for 90 s. After the deposition of the dielectric, samples are annealed at 80 °C for 90 min in nitrogen. An 80 nm thick aluminium layer is thermally evaporated through a metal shadow mask to pattern the gate electrodes.

3.3 Devices Performance Investigation

The J/V curves of the solar cells are recorded with a computer-controlled Keithley 2400 in air under a simulated AM1.5 spectrum provided by a class AAA Newport solar simulator. The intensity of the light is calibrated with a reference diode NREL certified with a spectral mismatch factor 0.99. The characteristic parameters such as scan rate, scan direction and pre-treatment are reported for each measurement along with the J/V curve.

The electrical characterization of lateral devices and transistors is performed in a nitrogen glove box with an Agilent B1500 Semiconductor Parameter Analyzer.

The Ultraviolet Photoelectron Spectroscopy (UPS) measurements are carried out with a Kratos Axis Ultra^{DLD} spectrometer using a He I (21.22 eV) discharge lamp. A -9.0 V bias Is applied to the sample in order to precisely determine the low kinetic energy cutoff. The analyses are carried out with an analysis area of 55 µm in diameter, at a pass energy of 10 eV, and with a dwell time of 100 ms.

Chapter 4
Organic Photovoltaics

Understanding the stability and degradation mechanisms of organic photovoltaics materials is required to achieve long device lifetimes. By and large instability is caused by the combination of light and atmospheric agents, with major roles of oxygen and water. The detrimental effects are electron trapping and photo-oxidation that break polymer conjugation and bleach the absorption[1]. Substantial efforts have been done to the development of efficient barrier materials which can protect the active photovoltaic layers from environmental agents[2]. However such attempts reflect more an engineerization of the devices respect to a fundamental solution to the problem. Investigating the degradation mechanism leads, on one hand, to the understanding of the physical chemistry behind the degradation issues, driving to an educated synthesis of optimized materials; on the other hand this can help in the optimization of the device architecture, e.g. targeting the right barrier responding to the right requirements.
As often highlighted when investigating the working mechanisms of excitonic solar cells, the interface physics rules the device macroscopic behaviour, and this is the case also for degradation processes. In fact, degradation of a single component can be substantially affected when it is blended to have the photovoltaic composite. A few concomitant phenomena are suggested, i.e. light screening, singlet exciton quenching and radical scavenging, where the latter is supposed to be the dominant one[3]. In fact, this mechanism is affected when tuning the electron affinities of the electron acceptor compound in order to improve the device photovoltage.

In the past few years, two mechanisms have been identified as being mainly responsible for organic molecules degradation in the presence of oxygen[4]. Oxygen sensitization is one of them, mediated by long lived triplet states with the energy level higher than the differential energy between the oxygen singlet state and its ground triplet state, i.e. 0.98 eV[5]. Alternatively, electron transfer could occur from the photo-excited polymer to molecular oxygen, generating the superoxide, O_2^-, which is a very reactive anionic

radical. It must be noticed that hydrated forms of molecular oxygen become easier to reduce, because their electron affinity becomes larger[6]; thus, even if water on its own seems to have a small effect, it can accelerate the rate of degradation when O_2 is present.

Blends comprising low band gap co-polymers acting as donors, combined with fullerene derivative acceptors, are among the most studied systems because of the possibility of extending the light harvesting into the red and near infra-red region of the solar spectrum. Poly [2,6-(4,4-bis-(2-ethyl hexyl)-4H-cyclopenta[2,1-b;3,4-b0]-dithiophene)-alt-4,7-(2,1,3-benzothia diazole)] (PCPDTBT) has been considered a prototypal system within the class of low band gap co-polymers, leading to PCE as high as 5.5% under optimized conditions in combination with [6,6]-phenyl-C61-butyric acid methyl ester (PCBM).

4.1 Review on the PCPDTBT:PCBM photophysics

Charge generation in PCPDTBT:PCBM blend has been recently elucidated with ultra-fast pump probe spectroscopy unveiling a sub-50 fs electron transfer at the polymer:fullerene interface resulting in the formation of both free carriers and interfacial charge transfer states (CTS with a branching ratio that depends on the photon energy). In particular it has been demonstrated that the higher is the exciton energy, the higher is the rate for charge generation, leading to exciton dissociation in less than 30 fs [1]. The bound low-lying energy CTS, on the other hand, act as a trap state and it can either recombine radiatively to the ground state (CTS1→CTS0 < 600 ps) [3] or further dissociate into free charges on a longer timescale. *Janssen R.* and co-workers [4] have recently observed that the interfacial CTS can also undergo intersystem crossing which back populates the co-polymer's triplet state, if the energy level lies below the interfacial CTS. The triplet and charge dynamics have been in particular investigated by means of optical TA measurements in the ns to ms time range by *Laquai et al.* [7]. Blending the PCPDTBT with a triplet sensitizer has been used as a way to univocally identify the triplet-induced absorption band of the PCPDTBT, showing a spectral feature peaking at 1 eV. They concluded that in the PCPDTBT:PCBM blend only polarons are

generated at room temperature, with no formation of triplets. This observation has a crucial impact into the physics of the PCPDTBT:PCBM based solar cell. From one side, shedding light onto the charge recombination pathways is indeed fundamental to increase the device power conversion efficiency; from the other side this has a direct impact into the solar cell stability as it is well known that triplet states can take part in the photo-oxidation mechanism of the active blend [3].

Janssen and co. workers[3] have concluded that triplet states, because of their relatively long lifetime, participate in bimolecular reactions such as singlet oxygen sensitization, responsible for severe degradation of the active layer. In particular, by using cw-photoinduced absorption (PA) spectroscopy, they correlate PCPDTBT:PCBM degradation with the population of the co-polymer triplet state from the interfacial CTS recombination. A more recent publication from *Friend et al.* [8] demonstrate with Time-resolved optical spectroscopy measurements that in the PCPDTBT:PCBM blend charges recombine towards the triplet state via a CTS with Triplet character. However, spectral features related to charge and triplet PA do overlap, leading their unique assignment through global fitting analysis only a reasonable guess.

4.2 Optical and magnetic characterization of PCPDTBT:PCBM blend

Figure 4.1 illustrates the absorption spectrum (a) and the excited state dynamics in Nitrogen atmosphere of the pristine PCPDTBT and of the PCPDTBT:PCBM blend investigated by means of combined CW photoinduced absorption (CW PA) spectroscopy (b), as a highly sensitive probe for the long-lived photoexcited species, and nanosecond transient absorption spectroscopy (ns-TA) (c), able to monitor the dynamics in the ns to μs time range.

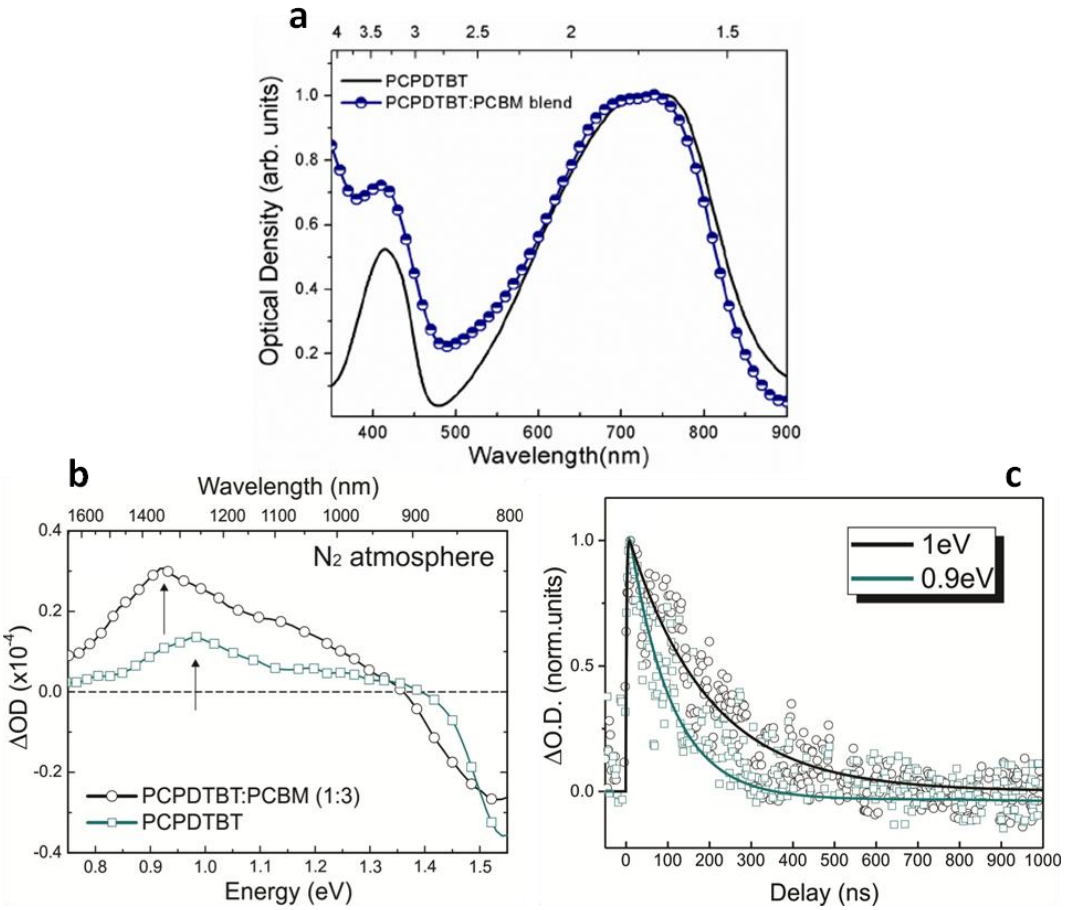

Figure 4.1: a) Absorption spectra of neat PCPDTBT (black line) and of the PCPDTBT:PCBM 1:3 (blue symbols). b) CW-PA spectra of the pristine PCPDTBT film (green) and PCPDTBT:PCBM blend (black) measured under Nitrogen atmosphere at room temperature. The arrows indicate the probe energies corresponding to the excited state triplet to triplet ($T_1 \rightarrow T_n$) photoinduced absorption (PA) transition (at 1eV) and to charge PA (at 0.9 eV). c) Temporal dynamics collected at probe energies of 0.9 eV and 1 eV for the PCPDTBT:PCBM blend and pristine PCPDTBT, respectively. The solid lines represent the fit extracted from a three-level rate equation model.

In figure 4.1b the pristine polymer presents the photobleaching (PB) band in the spectral range between 1.55 and 1.35 eV, in agreement with its absorption spectrum. A well-defined photo-induced absorption (PA) signal is recorded as well peaking at 1eV and with a decay time of about 100 ns (figure 4.1c). It has been assigned to triplet excitons absorption generated in the pristine polymer upon Inter-System Crossing (ISC) from the photoexcited singlet state (S_1) [9].

The spectrum of the blend reveals a broader and red shifted PA band, peaking at 0.9 eV, with a longer living component (see figure 4.1b). Previous studies have assigned this feature to the absorption of the polymer positive polaron [9], while no triplets are

supposed to be observed in the blend at room temperature [7]. However, as the spectral position of the triplet-induced absorption almost overlaps with the charges PA, it is very hard to optically disentangle the presence of the two species. To clarify this issue, we have performed Electron Paramagnetic Resonance (EPR) spectroscopy as a selective technique to detect paramagnetic species, such as triplets and polarons. The joint results will then strongly clarify the photophysical landscape of the system.

Figure 4.2a shows the trEPR spectrum of the pristine polymer solution at 500 ns time delay after the photoexcitation (thin film and solution samples show identical spectra). The spectrum extends over about 800 Gauss and shows a complex pattern, with a signal partially in emission and partially in absorption. These are common features for transient photogenerated paramagnetic species and depend on the non-equilibrium population of electron spin states (spin-polarization), controlled by spin-selective generation and decay processes[10]. The relevant parameters characterizing the magnetic interactions in the triplet state are the Zero-Field splitting parameters D and E, which are related to the mean electron-electron distance (D) and the deviation from axial symmetry of electron distribution in the S=1 state (E). They can be extracted by spectral simulation[11]. From the best fit simulation of the spectrum we obtained D = -0.0326 cm^{-1} and E = 0.0039 cm^{-1} (the sign of D is assumed to be negative as in other conjugated oligomers and polymers[12]). The good fit of the experimental trEPR spectrum allow us to infer that the triplet state, T_1, in the pristine polymer, is populated *via* spin-orbit promoted Inter System Crossing (ISC) from the singlet excited state S_1 (the sign of D and E is defined assuming an elongated electron distributions, and a positive E). This is a spin-selective process which populates the triplet zero field states with different rates and therefore generates a non-equilibrium distribution of the spin sublevel populations. The spin-selectivity of ISC process is defined by the triplet sublevels populations generated by ISC in absence of external magnetic field (zero field states). The relative sublevels populations are obtained from the fitting (presented as green line in Figure 4.2a) of the trEPR spectrum providing the values of Px:Py:Pz = 0.5:0.0:1.0.

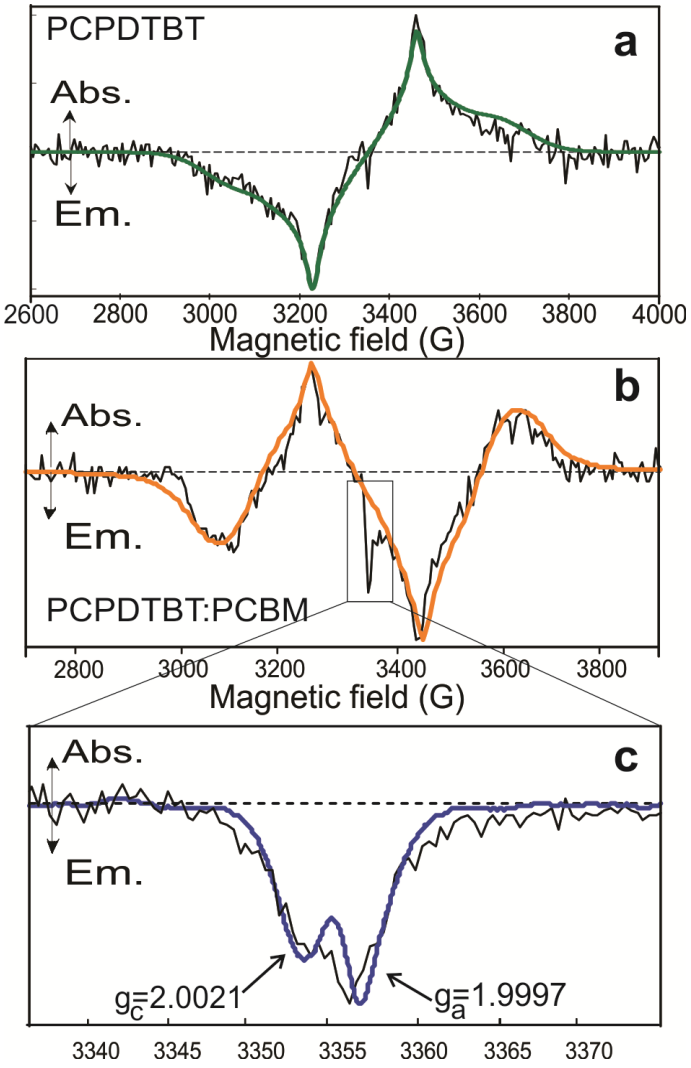

Figure 4.2: a) trEPR spectrum of the pristine PCPDTBT solution in o-DCB recorded at 0.5 ms after the laser pulse (black line: experimental data; green line: calculated triplet spectrum from ISC). (b) trEPR spectrum of the PCPDTBT:PCBM film recorded at 0.5 ms after the laser pulse (black line: experimental data; orange line: calculated triplet spectrum derived from both ISC and recombination processes). (c) trEPR spectrum in the narrow central magnetic field range (black lines: experimental spectrum), the integrated LEPR spectrum (blue line), sensitive only to long living photo-induced radical species. All trEPR spectra are recorded at 120 K. (Abs. = absorption, Em. = emission).

The trEPR spectrum of the PCPDTBT:PCBM blend (see figure 4.2b) at 500 ns time delay shows a signal extended over the same broad spectral range (about 800 Gauss) and a pattern that exhibits a double emission/ absorption peaks at low field-side and at high field-side. The shape of the signal suggests that we are still monitoring the triplet T_1 state of the polymer, but the different features indicate an *anomalous* spin polarization. The difference in the absorption/emission pattern with respect to the neat polymer is due to different spin sublevels populations. This can be rationalized by considering a

different pathway for triplet generation. While for the pristine PCPDTBT the T_1 copolymer state is solely be generated *via* ISC from S_1, in the electron donor-acceptor blend the EPR spectrum can be simulated by using the same zero field parameters of the PCPDTBT-pure triplet, but using sublevel populations generated by two concurrent mechanisms: the ISC and a spin-selective charge recombination mechanism populating preferentially the S = 1, m_S = +1 and S = 1, m_S = -1 spin states, indicated in the following as T_{+1} and T_{-1}. The best-fit calculated spectrum is shown in figure 4.2b (solid orange line). The $T_{\pm1}$ excess population can be explained by considering the possible spin states of a polaron pair or geminate charge transfer (CT) state: there are four spin levels, one with singlet character (S) and three with triplet character (T_- T_0, T_+). The S and T_0 levels are mixed by several mechanisms such as *g*-factor differences, electron-electron magnetic dipolar interaction and hyperfine interactions. The polaron pairs possess initially only singlet character. Due to the *g*-factor differences, hyperfine or dipolar interactions, the pair singlet state evolves into triplet T_0 within a time scale of 1-100 ns for organic radicals[10]. Spin relaxation processes slowly transfer population from T_0 to the T_- and T_+ states of the CT pair. If the CT pair in the singlet state recombines geminately, it leaves an excess of pairs in the triplet states T_+ and T_-, since the T_0 is partially depleted (see sketch in figure 4.3).

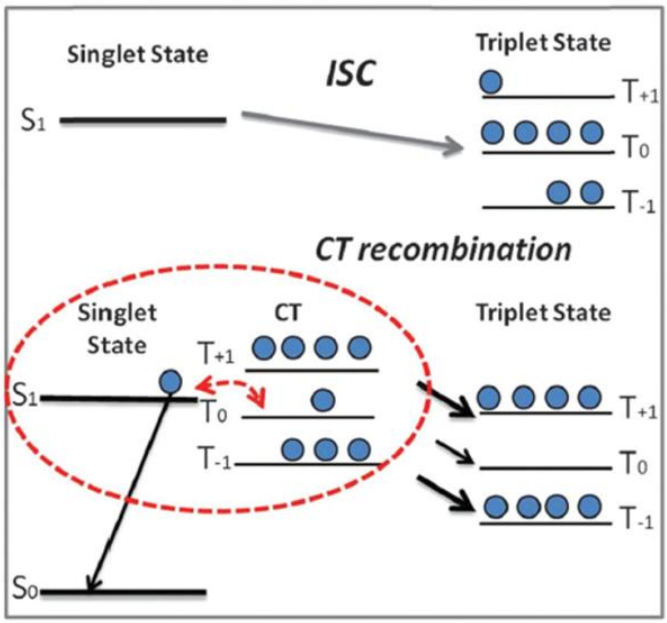

Figure 4.3: Representation of the main processes leading to triplet population.

Triplet recombination pathways for the polaron pairs have been already reported in the literature, leading to either the triplet state on the donor (the polymer) or on the acceptor (PCBM), with a spin-conserving process that projects the triplet sublevels population from the source state (the polaron pair in the triplet state) to the final triplet [13]; therefore, it is possible to conclude that the polymer triplet state acts in our photovoltaic blend as a sink state where a fraction of CTS can decay. When focusing in the spectral range between 3340 and 3370 Gauss (figure 4.2c) we note also the presence of a narrow emissive peak. The sharp feature is the result of two partially overlapped emissive peaks. Their spectral width extends over ~20 Gauss and their isotropic *g*-factors (as indicated by the arrows in figure 2.2c) correspond to the typical values for a semiconducting polymer cation (g_c = 2.0021) and for the PCBM anion (g_a = 1.9997)[14]. The solid blue line represents the two radicals species detected by Light-Induced EPR, sensitive only to long living photo-induced radical species, integrated and normalized (see figure 4.4 for the derivative spectrum and simulation). The emissive character of free charges has been already observed and interpreted in terms of a spin-selective decay pathway of the polaron pair by a partial mixing of S and T_- spin levels of the pairs[15]. The trEPR spectrum does not indicate any appreciable interaction between the two spins which could modifies the spectral shape giving rise to a spin-correlated radical pair spectrum, as already described in other polymer:fullerene based blends[15].

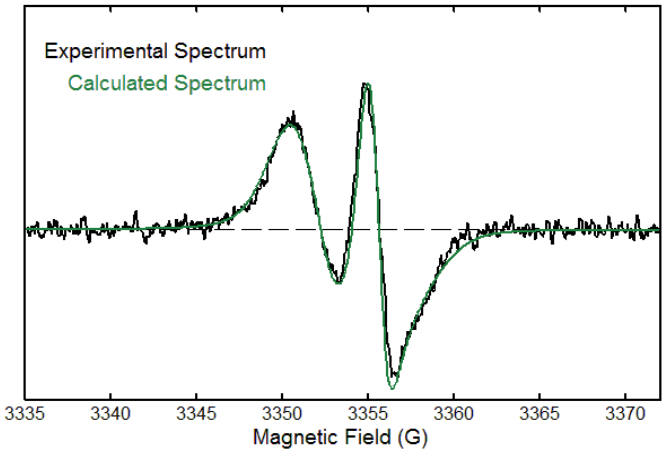

Figure 4.4: Black line: experimental LEPR spectrum (light on-light off) of PCPDTBT:PCBM film. Green line: calculated EPR spectrum of two radicals with *g* factors of 2.0021 and 1.9907. The spectrum has been recorded at 120K under Xe lamp illumination of the film.

From these results it can be now rationalized the main findings obtained from the joint optical and magnetic spectroscopy experiments. In the pristine material the excited

singlet state S_1, besides recombining directly to the ground state, populates the triplet T_1 state *via* ISC. In the blend, uncorrelated charges are optically detected, in agreement with *Laquai et al.* results. The CT recombination is spin selective and generates either ground singlet states or triplet states with a spin selectivity clearly revealed by its spin-polarized populations.

4.3 Degradation mechanisms induced by air exposure

Having clarified the photophysical scenario under inert conditions, it is necessary to explore the effect of air exposure. Photo-degradation in presence of oxygen is believed to occur through two main pathways. The first mechanism may involve the formation of singlet oxygen ($^1O_2$). This excited state of molecular oxygen can be formed by transfer of excitation energy from the polymer triplet excited state to molecular oxygen in its triplet ground state ($^3O_2$) as in the following reaction:

$$^3T_1 + ^3O_2 \rightarrow S_0 + ^1O_2^*$$

After formation, the singlet oxygen, which is a highly reactive species producing degradation in many organic materials[16], can react with the polymer chain leading to break up of the π-conjugation. The singlet oxygen generation is allowed only under the requirement that the excited triplet state energy is higher than the differential energy between the oxygen singlet state and its ground triplet state, equal to 0.98 eV. The second degradation mechanism involves the superoxide radical O_2^- formation upon photoinduced electron transfer from the photoexcited polymer singlet state. In this case a charge pair is formed, consisting of a positively charged polaron ($PCPDTBT^+$) on the polymer chain in combination with O_2^- [17].

In order to examine the energetic and assess the relative singlet and triplet excited states energies of the copolymer, are reported the results from Density Functional Theory (DFT) and time dependent (TD-DFT) calculations on a finite size chain oligomer of PCPDTBT.

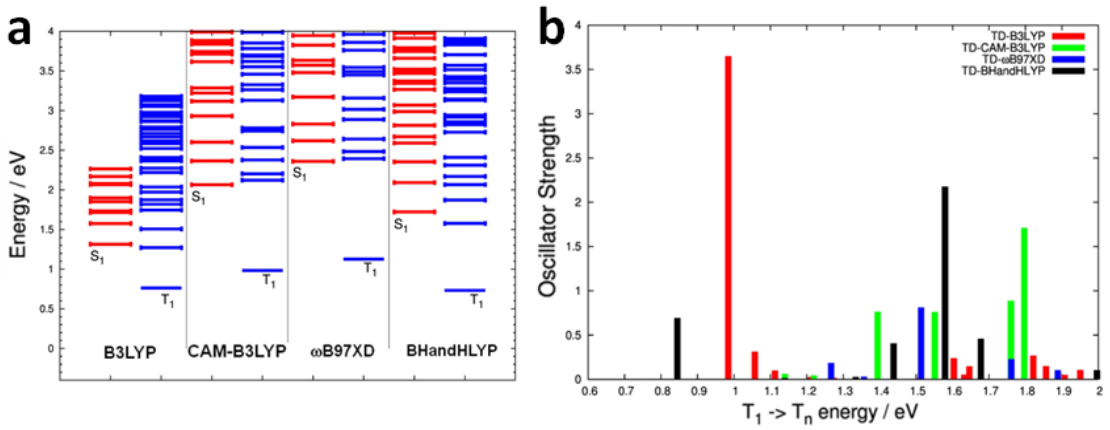

Figure 4.5: a) Vertical singlet and triplet transition energies as computed on the relative optimized ground singlet and triplet (T_1) state at different XC DFT functionals. b) TD-(U)DFT computed T1→Tn vertical excited state transitions at different XC DFT functional. TD-(U)B3LYP (red bars) gives the most reliable results if compared to the experimental (figure 4.1b) transient absorption spectra of the pristine PCPDTBT.

PCPDBT is a polymer featuring an intrinsic intra-molecular charge transfer character between the donor CPD and the acceptor BT units. In this frame standard GGA XC DFT functionals fail in describing the excited state *scenario*[18-20]. For this reason different XC DFT functionals have been considered[21-22]. In Figure 4.5a is shown the computed TD-DFT energies of both singlet (red lines) and triplet (blue lines) states of PCPDTBT as computed with different DFT functionals. B3LYP and BH and HLYP underestimate the energy of singlet excited states (in particular the low lying ones S_1) because of the strong intra-molecular charge transfer character[23]. CAM-B3LYP and ωB97XD correctly describe the character of the singlet excited states (at least S_1), however they slightly overestimate its energy[23]. Regarding triplet excited states the energy of the first T_1 state (the one of interest in this investigation) has been computed as 0.76 eV at (U)B3LYP, 0.73 at (U)BHandHLYP, 0.98 eV at (U)CAM-B3LYP and 1.12 eV at (U) ωB97XD. As also recently reported in the seminal work by *Gordon et al.* [22], range separated DFT functionals tend to overestimate the energy of triplet states, while the standard hybrid B3LYP (or PBE0) GGA functionals correctly describe them. For this reason the computed UB3LYP triplets energies can be considered as reference and the T_1 excited state can be allocated 0.98 eV above the ground state. This can be considered as assort of upper limit as in solid state, effect (e.g polarization effect) could even lower the actual triplet energy of the co-polymer. Then, the quality of the estimation is confirmed by computing the TD-DFT triplet-to-triplet ($T_1 \rightarrow T_n$) excited state transitions and their relative oscillator

strength (figure 4.5b). As it can be seen the TD-(U)B3LYP excited state transitions are extremely close to the experimental transient absorptions spectra (see PA band at 0.9 eV figure 4.1b), predicting an intense dipole allowed $T_1 \rightarrow T_3$ transition at 0.98 eV for PCPDTBT. Other DFT XC functionals overestimate the triplet excited state transitions energies (CAM-B3LYP and ωB97XD). Thus, from this theoretical investigation, it is possible to conclude that the T_1 state has very little chance to be involved in the degradation mechanism. This is experimentally confirmed when looking at trEPR spectra taken at ambient conditions. Figure 4.6a shows the trEPR spectra of the PCPDTBT:PCBM film taken in vacuum (10^{-5} mbar) and in air (black and red lines, respectively). The results show no alteration of the spectral features related to triplet species, indicating that the oxygen has a *negligible effect* on the polymer triplet trEPR intensity. The same observations are obtained in the pristine PCPDTBT film (see figure 4.6b).

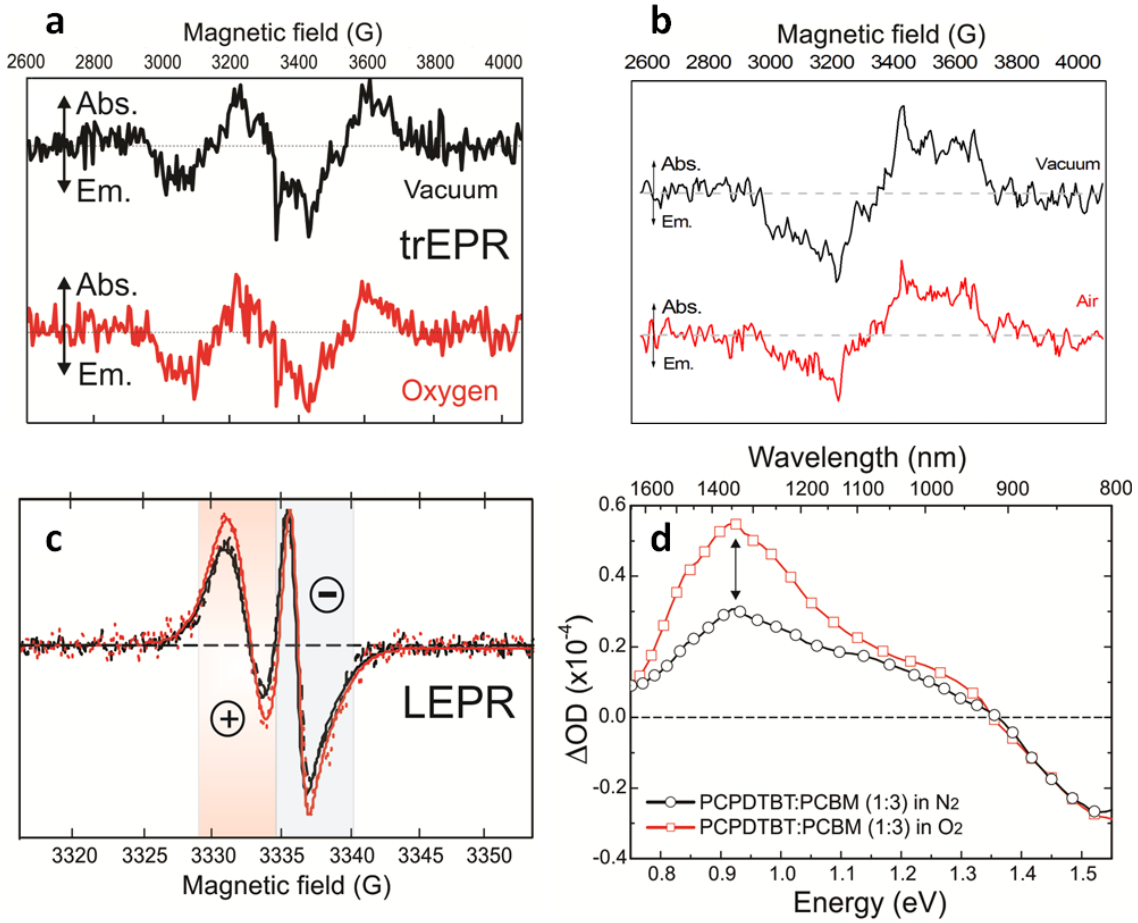

Figure 4.6 a) trEPR spectra at 0.5 μs after excitation of the PCPDTBT:PCBM blends in absence of oxygen (black), and in air (red). b) TrEPR spectra of pristine PCPDTBT film. Black spectrum: sample sealed under vacuum. Red spectrum: sample exposed to air. c) LEPR spectra of PCPDTBT:PCBM blend in absence of oxygen (black) and in air (red); dotted lines: experimental data, solid lines: best fit, calculated spectra. d)

CW-PA spectra of PCPDTBT:PCBM measured under Nitrogen (black dots) and O_2 (red squares) atmosphere. The arrow indicates the probe energy corresponding to $D_0 \rightarrow D_2$ transition (at 0.9 eV).

On the other hand, different scenarios appear by looking look at the effect of air exposure on the charge dynamics. In air it is possible to observe a reduction of the emissive peak of the free charges in the centre of the trEPR spectrum. Moreover, upon oxygen exposure, the Light-Induced EPR spectra (see figure 4.5c) show different intensity ratios of the spectral features related to the positive (PCPDTBT cations) and negative (PCBM anions) charges, the relative intensity of the cation being increased in air.

To clarify this point the information retrieved from EPR spectroscopy can be combined with the optical spectroscopy measurements. The CW PA spectra (see figure 4.6d) show that the PA band peaking at 0.9 eV increases under air exposure. On the other hand, one can note that the photobleaching (PB) feature does not change. This is telling that the density of the charge population in the polymer phase is increasing, though the total photoexcited population is unmodified. Bearing in mind that the dynamics of the pristine polymer is unaffected when the sample is exposed to air, it can be determined that the interfacial state, generated at very early times after exciton diffusion to the interface, is the key state which determines the branching ratio among the different populations. The oxygen molecules react with the interfacial charge transfer state at times faster than experimental time resolution ($t < 10$ ns) and electron transfer occurs leading to $PCPDTBT^+/O_2^-$ pairs. The observed enhancement in the optical absorption of the $PCPDTBT^+$ species and the unaffected dynamics of the triplet species suggest that the CT recombination to a triplet state is an extremely fast process and that another competing channel must exist. Note that if Oxygen was reacting directly with free charges no difference would have appeared in the PA spectra. To clarify this point are collected the photoluminescence (PL) spectra of the PCPDTBT pristine film and of the PCPDTBT:PCBM blend in vacuum and in air (Figure 4.7a and 4.7b respectively). The PL of the pristine sample, peaking at about 900 nm (1.37 eV), arises from the radiative recombination (S_1-S_0) of the polymer exciton. When the polymer is blended with PCBM, the excitonic PL is completely quenched, while an emissive band at a longer wavelength (around 1100 nm/1.12 eV) appears, which is assigned to the radiative recombination of interfacial CT states.

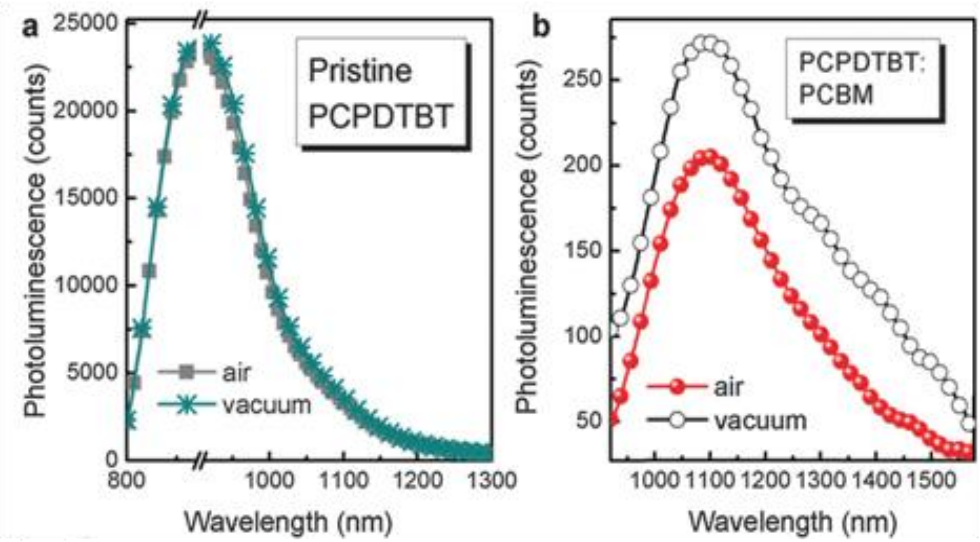

Figure 4.7: CW-photoluminescence spectra of (a) the pristine PCPDTBT (S1- S0) and (b) the PCPDTBT:PCBM blend (CT1 - CT0) upon excitation at 700 nm.

While the intensity of the pristine sample is unaffected, the emission intensity in the blend is quenched upon air exposure. This observation is in accordance with the short fluorescence lifetime of the pristine polymer film of 200 ps[22], which suggests that the deactivation of the pristine singlet excitons by radiative and non-radiative recombination is much faster than electron transfer to oxygen centred contaminant species. On the other hand, the excited state lifetime of the CT complex (>1 ns [11]) is long enough to allow for collisional quenching by oxygen involving electron transfer to the latter. Moreover, from PL emission it is possible to estimate the CT energy level to be around 1.1 eV (1127 nm), thus prone to interact with oxygen species. These results indicates that electron transfer from the CT state to the oxygen molecule competes with the radiative recombination of the interfacial charge transfer state to the ground state, leading to a higher density of unbalanced charges in the photovoltaic blend, see the resuming sketch in figure 4.8.

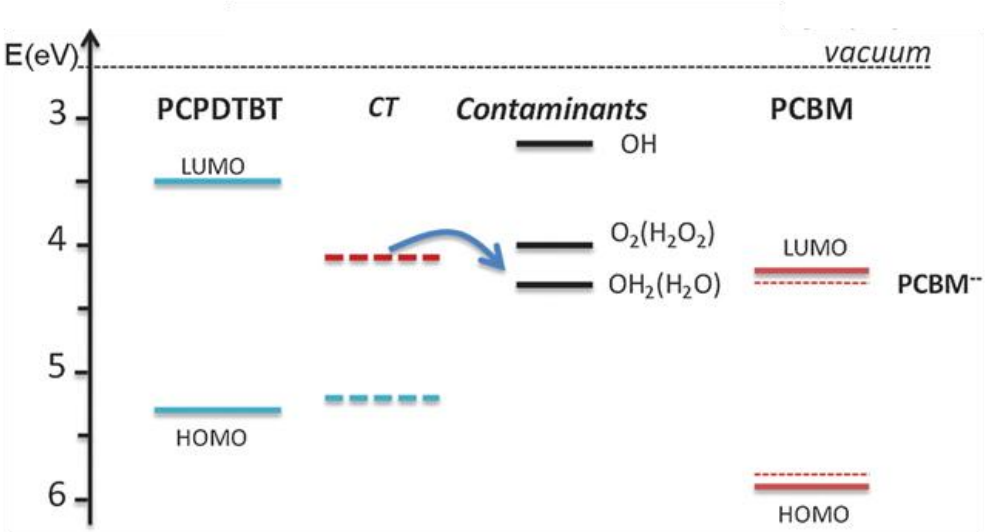

Figure 4.8: Energy level diagram of the system components. The arrow indicates the photo-degradation mechanism occurring through the interfacial CT state.

4.4 Conclusions

In this chapter the photophysics and the main degradation mechanisms that affect one of the most promising photovoltaic blend are deeply investigated. The dynamics of paramagnetic species, i.e. triplet and radical species, are thoroughly addressed by a combined optical and magnetic investigation: the pristine PCPDTBT the triplet state is populated via ISC from the singlet state, while in the PCPDTBT:PCBM blend, the interfacial CT state partially recombines into the polymer triplet state. Moreover, upon air exposure, the photophysical properties are virtually unaffected in the pristine polymer, but change dramatically in the blend with the electron acceptor. It is also demonstrated that the triplet state has no role in the degradation process. On the contrary it is shown the critical role of the photoexcited interfacial CT state in the generation of reacting and harmful species, such as the superoxide, upon electron transfer to contaminants such as OH·, OOH·, or hydrated $O_2(H_2O)_n$ clusters present in the atmosphere. In summary, this chapter sheds light on the crucial aspects of the interface physics, which so far has been mainly investigated to improve the overall device power conversion efficiency, in regard of the solar cell stability. The sensitivity of the CT state to contaminants depends on its lifetime and its energetics. The first one is more difficult to forecast, though recent studies have highlighted how the interface local morphology can facilitate the charge separation; on the other hand the latter can be easily tuned by

designing polymers and fullerenes with larger electron affinities. Robust photovoltaic blends require an educated design of the interface energetic not only for charge separation but also for stability.

References

[1] - F. Deschler, A. De Sio, E. von Hauff, P. Kutka, T. Sauermann, H.J. Egelhaaf, J. Hauch and E. Da Como, *Adv. Funct. Mater.*, 2012, **22**, 1461;

[2] - S. Guarnera, A. Bonucci, S. Perissinotto, R. Giannantonio, G. Lanzani and A. Petrozza, *RSC Advances*, 2013, **3**, 2163;

[3] - A. Distler, P. Kutka, T. Sauermann, H.J. Egelhaaf, D.M. Guldi, D. Di Nuzzo, S.C.J. Meskers and R.A.J. Janssen, *Chem. Mater.*, 2012, **24**, 4397;

[4] - E.T. Hoke, I.T. Sachs-Quintana, M.T. Lloyd, I. Kauvar, W.R. Mateker, A.M. NArdes, C.H. Peters, N. Kopidakis and M.D. McGehee, *Adv. Energy Mater.*, 2012, **2**, 1351;

[5] -D. Di Nuzzo, A. Aguirre, M. Shahid, V.S. Gevaerts, S.C.J. Meskers and R.A.J. Janssen, *Adv. Mater.*, 2010, **22**, 4321;

[6] -J.M. Shuo, L.H. Zhao, R.Q. Png, L.Y. Wong, P.J. Chia, J.C. Tang, S. Sivaramakrishnan, M. Zhou, E.C.W. Ou, S.J. Chua, S.W. Sim, L.L. Chua and P.K.H. Ho, *Adv. Mater.*, 2009, **21**, 4747;

[7] - Etzold, F.; Howard, I. A.; Forler, N.; Cho, D. M.; Meister, M.; Mangold, H.; Shu, J.; Hansen, M. R.; Mullen, K.; Laquai F. *J. Am. Chem. Soc.* **2012**,*134*, 10569-10583

[8] - A. Rao, P.C.Y. Chow, S. Gélinas, C.W. Schlenker, C.Z. Li, H.L. Yip, A.K.Y. Jen, D.S. Ginger and R.H. Friend, *Nature*, 2013, **500**, 435;

[9] - Di Nuzzo, D.; Aguirre, A.; Shahid, M.; Gevaerts, V. S.; Meskers, S. C. J.; Janssen, R. A. J. *Adv. Mater.* **2010**, *22*, 4321-4324.

[10] - Hayashi, H. *Introduction to Dynamic Spin Chemistry: Magnetic Field Effects on Chemical and Biochemical Reactions* **2004**, World Scientific Publishing Co., Singapore.

[11] - Weil, J.A.; Bolton, J.R.; *Electron Paramagnetic Resonance: Elementary Theory and Practical Applications* **1994**, John Wiley & Sons Inc., Hoboken NJ.

[12] - Bennati, M.; Grupp, A.; Mehring, M.; Bauerle, P. *J. Phys. Chem.* **1996**, *100,* 2849-2853.

[13] - Franco, L.; Toffoletti, A.; Ruzzi, M.; Montanari, L.; Carati, C.; Bonoldi, L.; Po, R. *J. Phys. Chem. C* **2013**, *117*, 1554−1560.

[14] - De Ceuster, J.; Goovaerts E.; Bouwen, A.; Hummelen, J. C.; Dyakonov, V. *Phys. Rev. B* **2001**, *64*, 195206

[15] - Franco, L.; Ruzzi, M.; Corvaja, C. *J. Phys. Chem. B* **2005**, *109*, 13431-13435.

[16] - Grossiord, N.; Kroon, J. M.; Andriessen, R.; Blom, P.W.M. *Org. Electron.* **2012**, *13*, 432–456.

[17] - Schafferhans, J.; Baumann, A.; Wagenpfahl, A.; Deibel, C.; Dyakonov, V. *Org. Electron.* **2010**, *11*, 1693-1700.

[18] - Peach, M. J. G.; Tozer, D. J. *J. Phys. Chem. A* **2012**, *116*, 9783-9789.

[19] - Peach, M. J. G; Williamson, M. J.; Tozer, D. J. *J. Chem. Theo. Compt.* **2010**, *6*, 1532-1537.

[20] - Dreuw, A.; Weisman, J. L.; Gordon, M. H. *J. Chem. Phys.* **2003**, *119*, 2943.

[21] - Sen, K.; Crespo-Otero, R.; Weingart, O.; Thiel, W.; Barbatti, M. *J. Chem. Theo. Compt.* **2013**, *9*, 533-543.

[22] - Leang, S. S.; Zahariev, F.; Gordon, M. S. *J. Chem. Phys.* **2012**, *136*, 104101.

[23] - D. Fazzi, G. Grancini, M. Maiuri, D. Brida, G. Cerullo, G. Lanzani, *Phys. Chem. Chem. Phys.*, 2012, **14**, 6367;

Chapter 5
Optical Properties of Perovskite Solar Cells

In the last two years, perovskite based solar cells (PSC) have been characterized by a fast development achieving impressive power conversion efficiencies up to 21%[1]. It has been demonstrated that organo-lead halide perovskite can work efficiently in a variety of device architectures going from a dye sensitized concept, in which the perovskite crystals replace the dye on the TiO_2 mesoporous scaffold[2], to a meso-superstructured device architecture in which the TiO_2 is replaced by an Al_2O_3 mesoporous scaffold[3], proving that the perovskite crystals can also sustain charge transport. As a further evolution, thin film architectures have been particularly successful[4] demonstrating performances comparable to traditional inorganic thin-film solar cells. However, beside the outstanding performances showed, the complete understanding of the fundamental properties of this material is still an open field of research. In particular, the comprehension of the optical properties of perovskite is mandatory for the progress and the development of new devices.

This chapter is dedicated to the investigation of the optical properties of organo-halide perovskite ($CH_3NH_3PbI_3$). The guideline is represented by the progressive knowledge of the optical properties, starting from concepts embedded in the devices up to a general analysis of the properties of the material, with the purpose of focusing the problems that affect the realization of the solar cells both in terms of structural uniformity and stability.

5.1 The Role of the Substrate

The optical properties of perovskite thin film are strongly influenced by the crystallization substrate. As reported in chapter 2, the perovskite is formed following a crystallization process similar to a self assembly. During this process the characteristics of the film are defined. In a simplified vision, this step “determines” the quality of the film, which is linked to the amount of defects formed during the crystallization process and the full conversion of the precursors. All these kinetics are influenced by the

underlying substrate used that, through variation of the Surface Free Energy (SFE) modifies the crystallization conditions. For this reason the optimization of the deposition techniques has been tuned for every single substrate, changing the annealing conditions. Early works on PSC were focused on the increment of the efficiencies of the devices without an eye to understand and describe the real properties of the perovskite. This was the result of the engineerization process of the devices in the rush for high efficiency. During this phase the optical properties of perovskite were considered the absorption spectrum and the photoluminescence (PL). On the one hand, the presence in the absorption spectrum of the band edge at 780 nm was as an indicator of successful formation of the perovskite ($CH_3NH_3PbI_3$ in this case) together with the X-ray diffraction spectra (XRD). From the opposite side, the PL was used to assign good charge communication between the perovskite and the interlayers[5-6]. The importance of this second point is relevant. As reported in chapter 2 the PL in perovskite is the consequence of the radiative recombination of photogenerated charges. Higher the intensity of the PL higher is the number of recombined charges. When a charge is injected in an extraction layer the possible number of recombination events is decreased and this is reflected in a PL with a lower intensity. This effect is called quenching of the PL and was assign to a good injection of charges in extraction layers. In this vision, understanding the role of the substrate in the crystallization processes, i.e. the extraction layer, is the first step for a complete description of the optical properties of perovskite thin films.

5.1.1 Consequences on the morphology

The first configuration of PSC uses mesoporous scaffold in which the perovskite is inserted (see chapter 2)[2-3]. These scaffold are metal oxides realized with electron injecting material (TiO_2) or dielectric (Al_2O_3). One of the problem of titanium dioxides is the complicated realization through slow and high-temperature treatments. Thanks to the work of *Kelly et al.* Zinc oxide (ZnO) results as a suitable candidate to replace titanium dioxide[7]. Due to its low-temperature processability this oxide has a strong technological relevance[8], in fact, it has already been employed as a selective contact in

perovskite based solar cells both on rigid and flexible substrates showing good charge collection properties[9] and overall performances comparable to the most commonly used TiO_2. Surprisingly, the annealing conditions required for the perovskite formation are strongly influenced by the choice of the substrate. For substrates such as TiO_2 and Al_2O_3, generally, after the deposition of the precursors the perovskite layer looks yellowish and transparent, meaning that the self-assembling of the crystal has not yet taken place. A heat treatment at 100 °C for 1 hour is essential for initializing the nucleation of the crystallites, thus enabling the formation of the perovskites[3-4]. On contrary, on ZnO the layer looks brownish by eye and after 1 min annealing at 100 ◦C the perovskite is completely formed. Longer annealing time leads to the complete degradation of the perovskite back to the original precursors. The reduction in the annealing time suggests a faster kinetic for the crystallization of the perovskites on ZnO substrates which can be mainly related to a different surface chemistry. To investigate these processes ZnO scaffolds of the same thickness were realized with nanoparticles of different diameters: 20, 50, 70 nm. The morphologies of the perovskite films obtained on these scaffolds and on a reference sample on Al_2O_3) scaffold are reported in figure 5.1 along with the respective absorption spectrum.

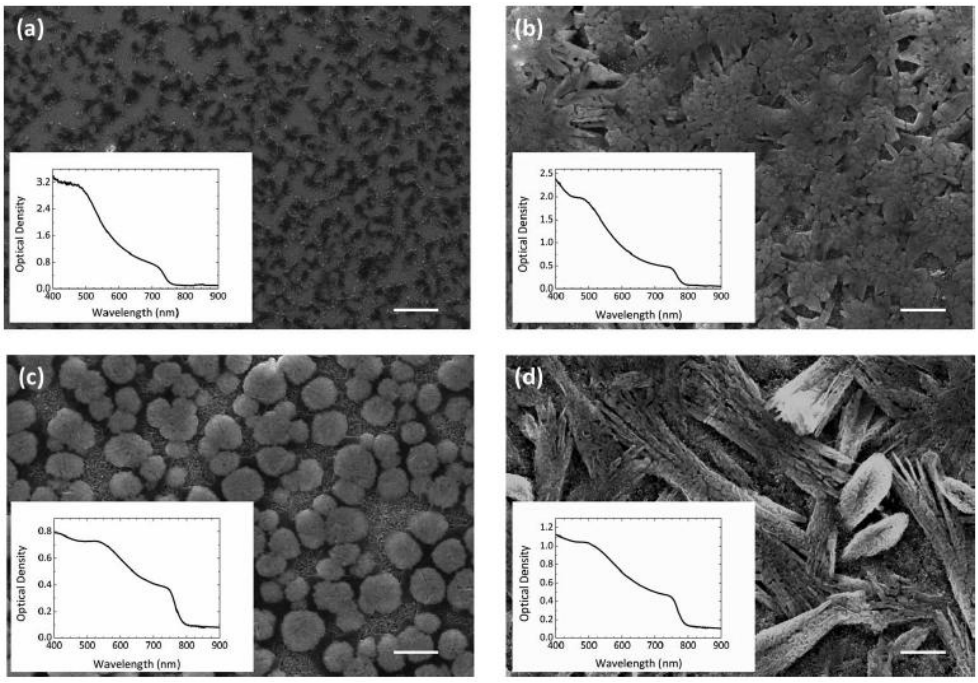

Figure 5.1: SEM pictures (top view) of perovskite polycrystalline films grown on 1000 nm thick mesoporous Al_2O_3 scaffold (a) and ZnO scaffolds made of ZnO nanoparticles of 70 nm diameter (b), 50 nm diameter (c), and 20 nm diameter (d), respectively. Scale bar: 10 μm (a); 2 μm (b)–(d).

While the perovskite crystals are mainly formed in the Al_2O_3 scaffold with limited coverage of the capping layer left on top of the mesoporous substrate (figure 5.1a), the samples fabricated on the ZnO substrates show a consistent capping layer (figures 5.1b-d). Interestingly, by changing the ZnO porosity it is possible to observe different crystalline macro-structures. Crystallites of perovskite are formed by nucleation on 70nm ZnO nanoparticles (figure 5.1b) rising interconnected structures of condensed domains in the range of few microns of diameter. Behind these capping structures the perovskites infiltrated inside the scaffold forming small crystals into the mesoporous. The structures obtained from 50nm ZnO nanoparticles are different from the previous one (figure 5.1c). In this case the capping layer is formed by compacted island with circular shape. The bridge-like interconnections between these structures are missing in favor to a flat connection, similar to the capping layer observed in Al_2O_3 scaffold. The coverage of the capping layer in this scaffold is less respect to the 70nm scaffold, showing more mesoporous regions of bigger domains. A completely different morphology is reported for perovskite growth on 20nm ZnO substrate. In this case the rounded shape presents in 70nm and 50nm is not formed. A fibrils-like structures are obtained with microns length. These fibrils extend all over the substrate as a disoriented mat overlapping each other. Zooming inside the fibrils showed a crystalline structures partially oriented in the sense of the fibers with sub-microns domains, figure 5.2.

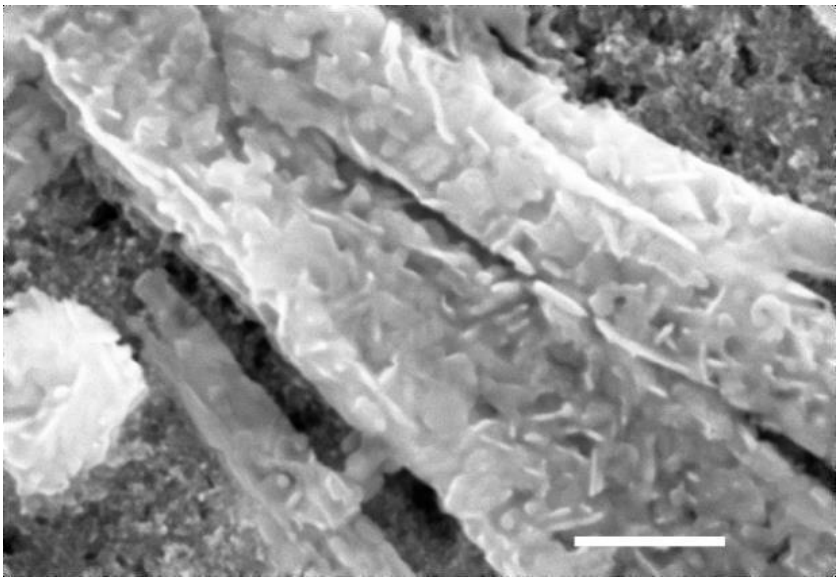

Figure 5.2: Structure of perovksite fibrils growth on ZnO scaffold made of 20 nm diameter nanoparticles. Scale bar: 1µm.

These observations highlight a critical issue for the *in situ* crystallization, especially in a porous substrate, whose wettability will be affected not only by the chemical nature of the scaffold but also by its porosity. Directly after application of the precursor solution, the pores will be wet by the solution with an excess of solution on top. The ratio between infiltrated solution and excess solution on top will strongly depend on the wettability of the substrate which is directly related to the Surface Free Energy (SFE) of the scaffold. SFE has been determined by Contact Angle (CA) measurements using the Owens-Wendt-Rabel-Kaelble (OWRK) model for the four substrates[10]. This model splits the SFE in two part: the dispersion forces on one hand and all the polar components on the other, in the approximation of negligible spreading pressure. The model uses a linear equation of different measures of CA obtained from different solvents whose both polar and disperse components of surface tension are well known. The slope and the intercept of the linear fitting are the square roots of the polar and disperse components of the SFE of the material under study. The SFE of the different ZnO and Al_2O_3 scaffolds are reported in table 5.1.

np size	**SFE**	**Polar**	**Disperse**
ZnO 70 nm	48.38	28.8	19.6
ZnO 50 nm	34.32	10.2	24.13
ZnO 20 nm	25.9	17.2	8.63
Al_2O_3 50 nm	63.75	58.13	5.62

Table 5.1: Surface Free Energy for ZnO and Al_2O_3 scaffolds. The polar and disperse component are also reported. The liquids used for the CA measurements are water, ethylene glicole and mixing of both in different ratios.

Al_2O_3 scaffold shows the highest SFE, while for the ZnO scaffold it increases with increasing the nanoparticles size. In the initial stages of spin-coating a large quantity of solution flows off the substrate and as the process proceeds the solvent evaporates from the surface of the wet film setting up a concentration gradient of the precursors within the film. The precursors are driven via diffusion into the pores with the loss of solvent and increasing concentration. Of course, this process critically affects the

crystallization dynamics which can favour the stabilization of different phases in terms of crystals chemical composition, structure, and size.

5.1.2 Consequences on the photoluminescence

The extraordinary differences in the shape and structure of the perovskite do not afflict the absorption spectra that appear to be very similar for all four scaffolds. It is therefore natural to wonder if the optical properties of these perovskites are really identical. The time-resolved fluorescence (tr-PL) allows to obtain more detailed information about the dynamics of photophysics than steady-state fluorescence and therefore becomes a sophisticated tool to understand what differences are hidden behind the different scaffolds.

Figure 5.3a shows the PL decays taken from the samples shown in figure 5.1, excited both from the capping layer side or the substrate side. The decays are taken at the peak of the photoluminescence band (figure 5.3b).

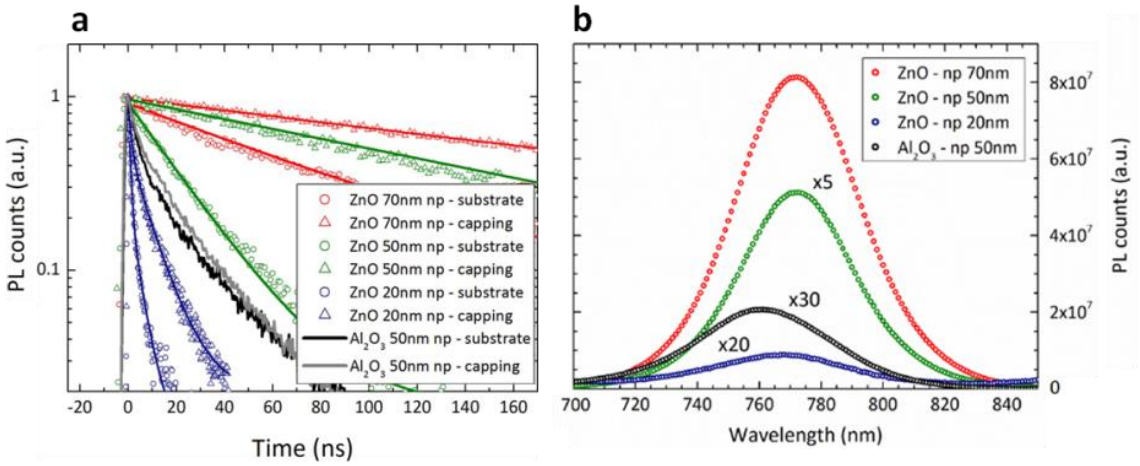

Figure 5.3: a) PL decays of perovskite deposited on ZnO mesoporous scaffold substrates: 20 nm blue, 50 nm green and 70 nm red, measured either exciting the sample from the substrate's side (circles) or from the capping layer side (triangles). Straight lines represent the fitting curves. The black and grey lines represent the PL decay on mesoporous Al_2O_3 exciting the sample from substrate and capping layer sides, respectively. b) PL spectra. Excitation wavelength λ = 480 nm.

Interesting observations can be highlighted. Overall, the PL decays become shorter as the ZnO nanoparticles' size becomes smaller. Moreover, when comparing the decays upon excitation of the capping-layer side and the substrate side, it can be observed a

further shortening in the lifetime in the latter case. Similar dynamics are also observed in the presence of mesoporous TiO_2 substrates, figure 5.4.

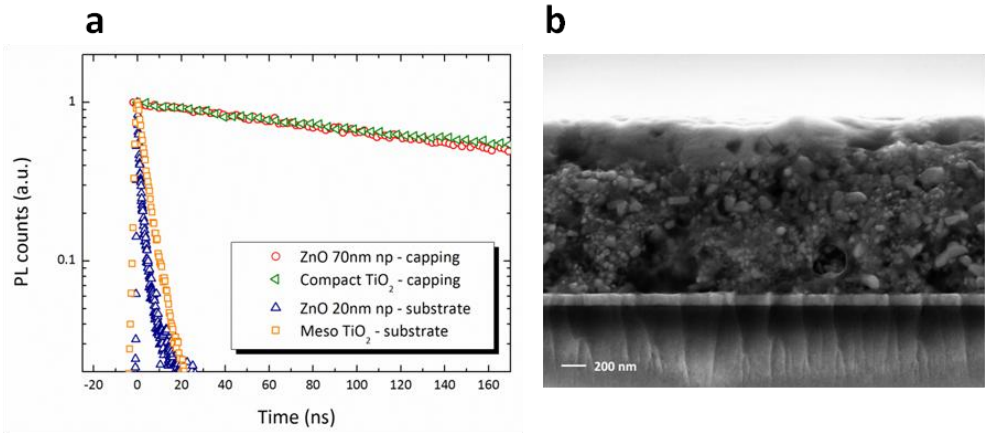

Figure 5.4: a) PL decay of perovskite deposited on ZnO mesoporous scaffold substrates obtained from 70 nm nanoparticles exciting the capping layer side is compared to PL decay on compact TiO_2. Moreover, the decay on ZnO mesoporous scaffold substrates obtained from 20 nm exciting from the substrate side is compared to the decay on TiO_2 mesoporous scaffold substrates obtained also from 20 nm nanoparticles. b) Cross-sectional SEM of perovskite polycrystalline film grown in a ZnO scaffold made of 20 nm diameter nanoparticles. Scale bar: 200 nm.

Since ZnO is an electron extraction layer, at a first glance this can be attributed to a more efficient injection of electrons in the presence of a larger density of interfaces due to the reduced average nanopores size. However, this conclusion does not appear really straightforward upon a deeper analysis. From the absorption spectra showed in the insets of figure 5.1 it is possible to estimate that the penetration depth of the excitation light at 480 nm ranges from ~150 nm to ~400 nm, thus exciting from the substrate side (scaffold thickness ~1000 nm) ensures excitation of the perovskite nano-crystallites grown exclusively within the oxide scaffold (see pores filling in figure 5.4b). Comparing the decay probed from perovskites grown in Al_2O_3 and ZnO scaffold, both made from 50 nm nanoparticles, one should expect a stronger PL quenching in the presence of the ZnO, as Al_2O_3 has a large band-gap which precludes charge injection.

However, for the 50 nm ZnO nanoparticle-based mesoporous substrate is possible to observe an even longer lifetime. In order to further investigate this issue the PL decays from perovskite polycrystalline films grown on a flat glass substrate, on a thin (~300 nm) Al_2O_3 mesoporous scaffold (which will also present a large fraction of capping layer) and on a thick (~800 nm) mesoporous scaffold (with a very small fraction of capping layer)

were measured and shown in figure 5.5a. The lifetime becomes shorter and shorter as the scaffold thickness is increased, i.e., increasing the contribution of crystallites grown in the scaffold to the overall PL signal with respect to the contribution coming from the crystals of the capping layer (schematic shown in Figure 4.5b).

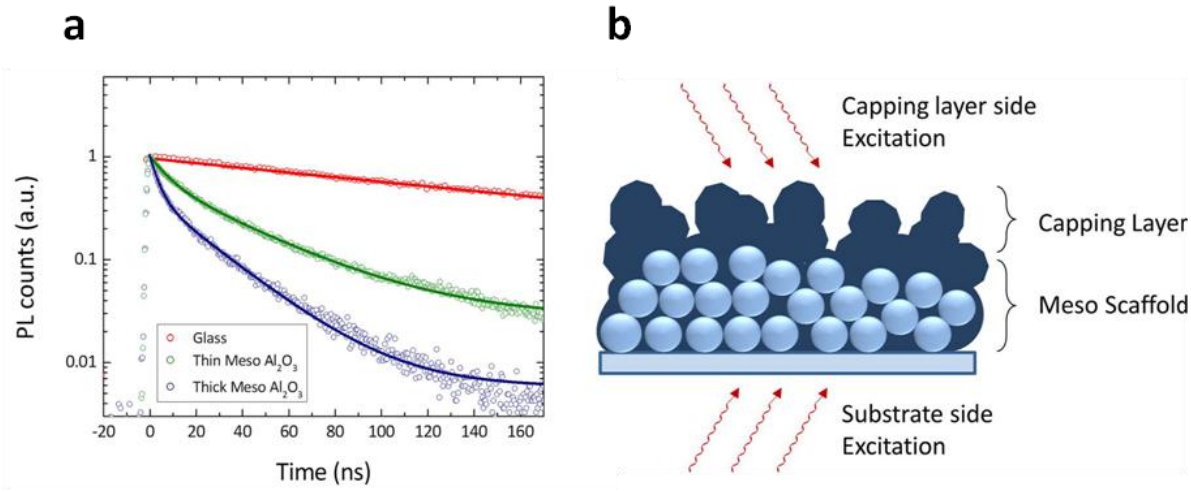

Figure 5.5: a) PL decay of perovskite deposited on bare glass (red), thin (~300 nm) mesoporous Al_2O_3 (green), and thick (~800 nm) mesoporous Al_2O_3 (blue) together with the straight line representing the fitting curves. b) Schematic representation of the layered structure of the samples investigated. Excitation wavelength λ = 480 nm.

Figures 5.6a and 5.6b show 2D photoluminescence maps collected from the perovskite polycrystalline film grown on an even thinner Al_2O_3 scaffold (~100 nm) exciting from the substrate side and capping layer side, respectively. These maps show that when changing the side of excitation two emissive states can be selectively observed, one short living and blue shifted with respect to the other. In particular, the emission shown in figure 5.6a arises from the superposition of two different contributions coming from the two layers in the thin film which get sequentially excited by the laser, i.e., the perovskite infiltrated into the mesoporous scaffold (short-living emission peaking around 760 nm) and the capping layer (long-living emission peaking at around 775 nm). This indicates that the shortening of the lifetime in presence of the scaffold is not simply due to PL quenching process, but it is related to an intrinsic change in the crystallite optoelectronic properties, in agreement with the absorption spectra taken from samples with similar architectures showing that the fully mesostructured film is characterized by a blue-shifted absorption onset with respect to the flat film. Ball *et al.*[4] have already demonstrated that the perovskite crystals present in the capping layer are larger in size,

going from less than 50 nm in the scaffold, where the crystal growth is constrained, to crystals larger than 500 nm when they are left to grow freely. Thus in conclusion, the capping layer and the mesostructured film must be considered as two different compounds with different photoluminescence properties.

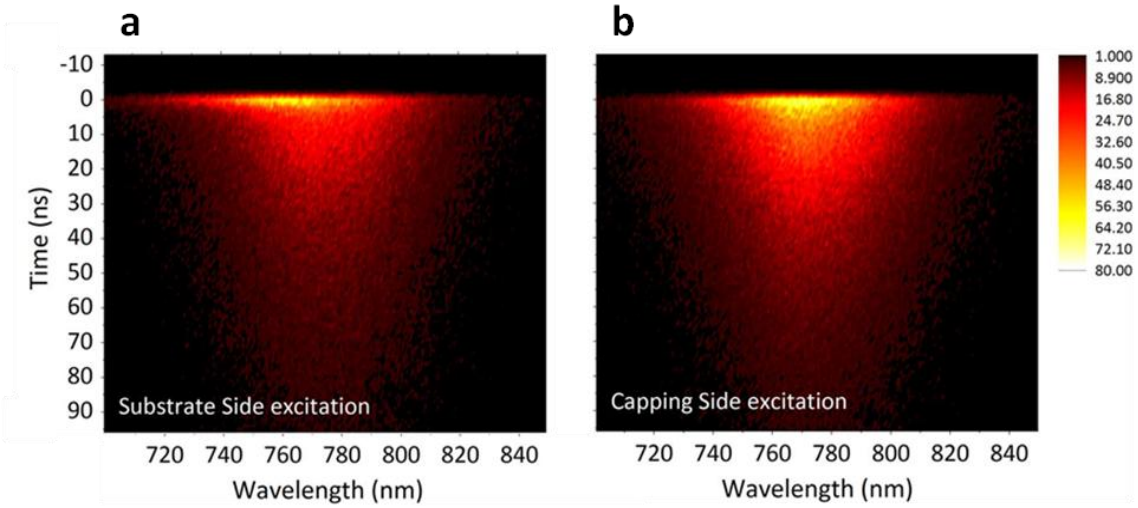

Figure 5.6: PL maps of perovskite deposited on thin mesoporous Al_2O_3 exciting the samples from the substrate side (a) and the capping layer side (b), respectively. Excitation wavelength λ = 480 nm.

5.2 From Mesoporous to Flat

It was shown in the previous paragraph that the perovskite infiltrated the scaffolds mesoporous has specific optical properties. The PL investigation showned that small crystallites that are formed inside the porosities show a blue shift in the emission respect to the surface layer which forms the capping layer. It is therefore natural to ask whether there are differences even between flat films of perovskite and mesostructured films. It has been reported that the photoluminescence is a powerful tool for investigating these properties, however there are some limits in the interpretation of its quenching. It is then necessary to use other techniques that could give a macroscopic description of the variation of optical properties depending on the nature of the perovskite itself.

Good quality of flat perovskite film was a though challenge to achieve. The main problem was the low coverage and the bad morphologies that were related to the first

deposition techniques used (in particular one step deposition, see chapter 2). In this sense to use a mesoporous scaffold was helped to get the films more homogeneous, removing defects that decreased the efficiency of the solar cells. However, with the development of the deposition techniques (in particular two step deposition), homogeneous and flat polycrystalline films of perovskite were achieved. These films present grains size from 500 nm up to 1 µm, which are much bigger respect to the constrained crystallites of the mesoporous scaffold. Raman spectroscopy represents a powerful tool to investigate the properties of these two types of perovskite form a different angle respect photoluminescence investigation. The vibrational Raman spectra of a flat perovskite and fully-mesoporous samples are reported in figure 5.7.

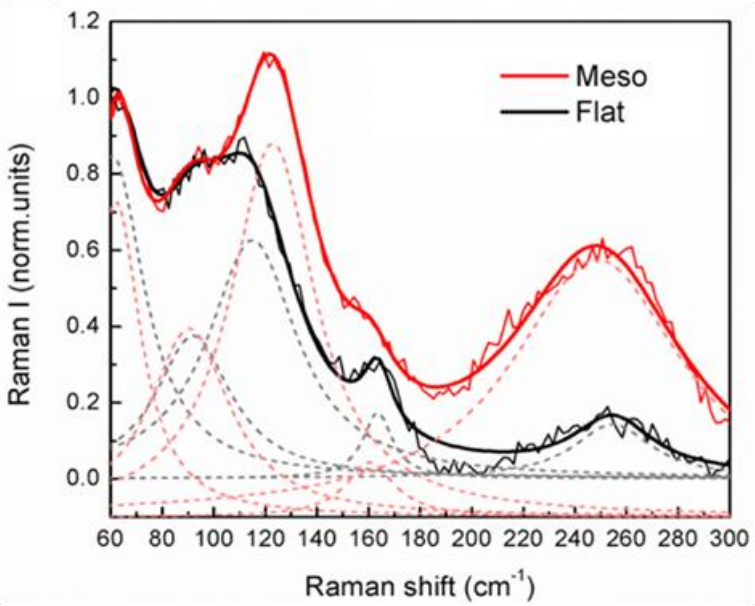

Figure 5.7: Resonant Raman spectra of mesoporous (red line) and of flat perovskite (black line). Dashed lines represent the Gaussian model used to fit the Raman peaks, the thick lines are the results of the fit, as the sum of the individual Gaussian functions.

The two peaks at lower frequencies, at around 62 and 94 cm^{-1}, represent the diagnostic modes of the inorganic cage[11]. The peak at 119 cm^{-1} is associated with the organic libration modes along with the unstructured feature in the frequency range of 150–160 cm^{-1}. Moreover, the broad, intense band at about 250 cm^{-1} is assigned to the organic torsional mode[12]. The latest, being sensitive to the specific organic–inorganic interactions (mainly occurring through Coulomb and hydrogen-bonds interactions between the NH_3 groups of $CH_3NH_3^+$ (MA) and the electro-negative iodine atoms) represents an important marker of the orientational disorder of the material[11]. In

particular, in the more disordered phase of $MAPbI_3$ (whose extreme is represented by the cubic phase for temperature above 327 K [13]) the MA^+ cations are arranged in a random orientation within the inorganic cage due to their large orientational mobility. This leads to a broadening and a red-shifting of the band at around 250 cm^{-1}. On the contrary, in the more ordered *head to tail* arrangement of the MA^+ cations (whose extreme is represented by the orthorhombic phase for temperature lower than 160 K), this band looses intensity (by symmetry selection rules) and it considerably blue-shifts. Finally, the broad shoulder peaking at ~160 cm^{-1} is assigned to libration of the MA^+ cations, calculated at 156 cm^{-1}. From the simulation it is additionally expected to become sharper and more intense, in the more ordered *head to tail* arrangement[12]. Analyzing the evolution of the Raman spectrum from the mesoporous to the flat perovskite a clear trend is visible at first glance: 1) the band at around 250 cm^{-1} blue-shifts and its intensity strongly decreases; 2) the peak at 119 cm^{-1} decreases in intensity and red shifts to 115 cm^{-1}; 3) the band at around 160 cm^{-1} becomes sharper and more resolved; 4) the peak at around 94 cm^{-1} gains strength.

These observations highlight the different organic-inorganic interactions affecting the orientational order of the organic cation in the unit cell when the perovskite film is grown in two different conditions: flat and mesoporous. The experimental findings point to a clear trend, that is an ordered arrangement of the MA cations in flat samples versus a more disordered cation arrangement in the mesoporous sample. Even if the organic cations do not directly participate to the frontier orbitals of the semiconductor[14], their displacement and their interaction with the global structure affect the electronic properties of the compound.

This is finally confirmed in the red shift of the onset of the UV-vis absorption spectrum and PL peak when moving from mesoporous to flat film, as reported in figure 5.8.

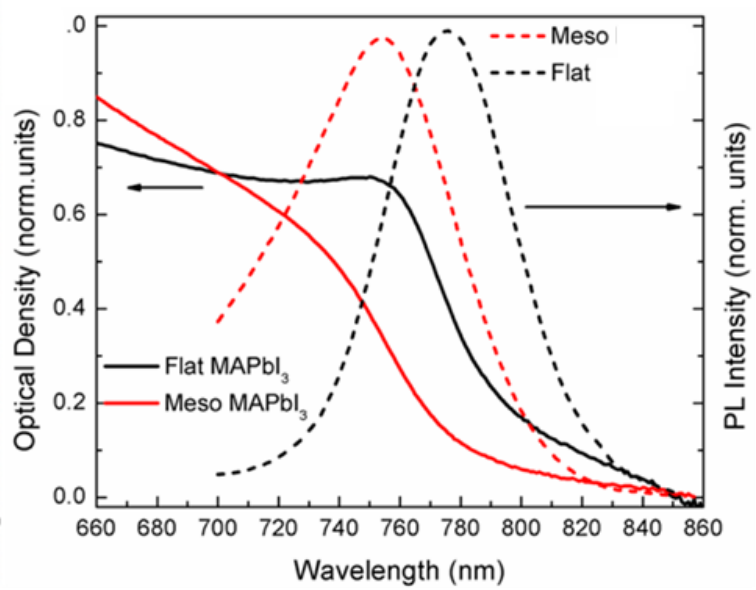

Figure 5.8: Normalized optical absorption (at 700 nm) for the mesoporous perovskite (red solid line) and the flat film (black solid line), and corresponding CW photoluminescence spectra (dashed lines).

5.3 The effect of the crystals size

In the first paragraph it was shown that the optical properties of perovskite in a mesoporous scaffold change moving from small crystallites inside the scaffold to large crystals of the capping layer. In the second paragraph the optical properties of a flat film of perovskite and those of a fully mesostructured samples were compared. It was reported that, passing from large polycrystals of the flat substrate to the crystallites of the mesoporous optical properties follow a similar trend to what seen in the first paragraph. It is therefore legitimate to wonder how the optical properties vary as a function of the size of the perovskite crystals.

Double step deposition is a suitable technique for the realization of homogeneous film of perovskite (see chapter 2). After the deposition of the lead salt (PbI_2) the substrate is dipped for a certain amount of time in a solution of Methylammonium Iodide (MAI) in isopropyl alcohol (IPA). While the dipping time seems to not affect the resulting film, the temperature and the molar concentration of the MAI solution play an important role on the final characteristics of the film. The resulting perovskite film obtained from two step deposition is composed by a coalesced structure of small cubic crystallites. The size of these cuboids vary as a function of temperature and MAI concentration. In detail, the size of the crystals is proportional to the temperature and inversely proportional to the

MAI concentration. The range of temperature can vary from 25 °C to 70 °C, while the MAI concentration from 0.031 M to 0.063 M. In figure 5.9 are reported the SEM top view of nine samples realized with different temperatures and MAI concentrations.

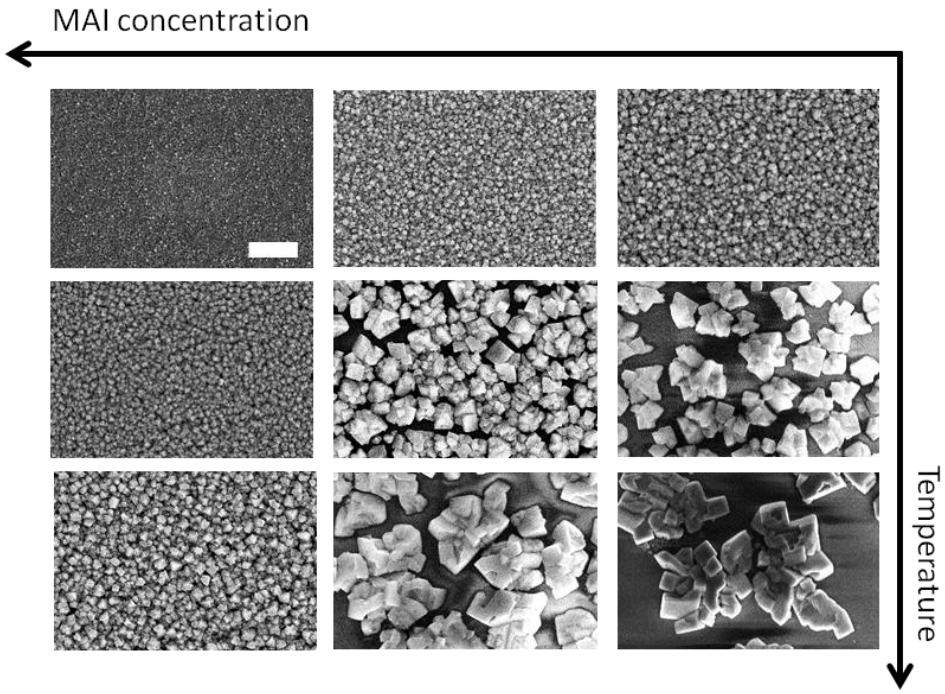

Figure 5.9: Top View SEM images of CH3NH3PbI3 crystals grown via two step deposition procedure changing the MAI solution's concentration and temperature. White bar is 4 µm.

The size of the crystals varies from less than 250nm up to more than 2 µm. Thanks to double step deposition is then possible to have a complete distribution of the dimensions in order to shed light on the variation of the optical properties. In figure 5.10 is reported the positions of the optical band edges obtained from UV–Vis absorption spectra as well as the positions of the PL peaks for all of the samples (coincident values are omitted).

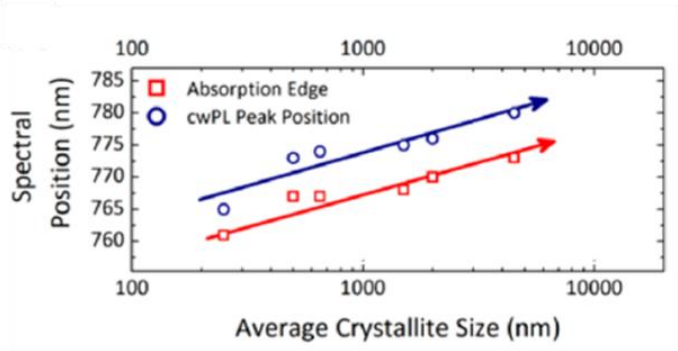

Figure 4.10: Spectral positions of the UV-vis absorption band edge (red) and cw-PL peak position (blue).

From figure 5.10 it can be observed that as the polycrystallite grows in size, the optical absorption edge shifts to longer wavelengths (lower energies) along with the PL peak position, keeping constant the shift between the two.

The time-resolved PL dynamics of the aforementioned series of samples is reported in figure 5.11. The measured tr-PL decays are fit with a stretched exponential function to obtain the respective PL lifetimes, which are reported as a function of the average crystallite size in the bottom panel of figure 5.11. For the smallest crystals (<250 nm), a lifetime of about 2 ns is obtained. As the crystallite size is increased, an associated increase in the lifetime can be appreciated (figure 5.11, bottom panel), with the largest crystallites (>1 µm) showing a lifetime greater than 100 ns, approaching values that in previous works have been reported only for Cl-doped $MAPbI_3$ perovskite (reported in figure 5.11 as black circles for comparison).

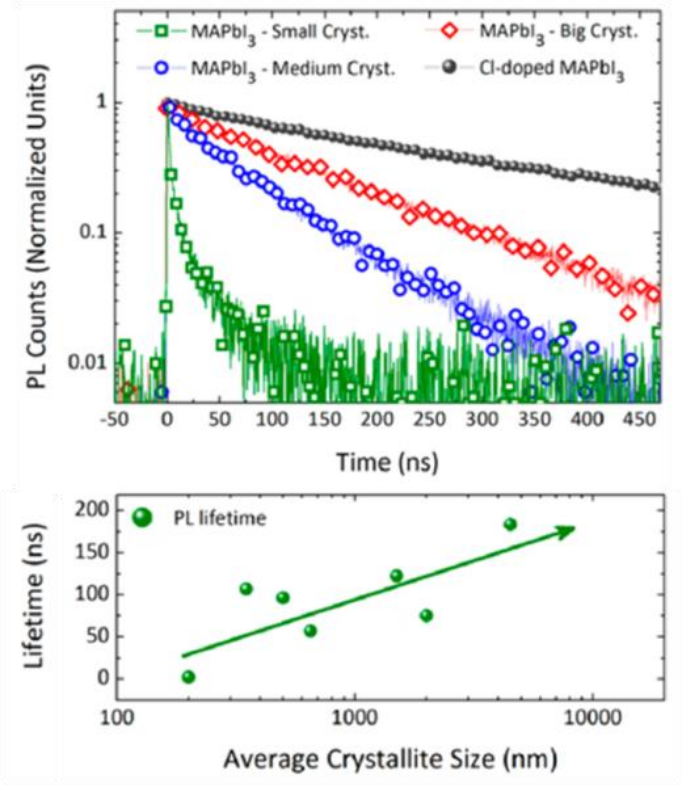

Figure 5.11: (top) Representative tr-PL dynamics for three different $MAPbI_3$ crystal sizes and PL dynamics of Cl-doped $MAPbI_3$. (bottom) PL lifetime as functions of the crystallite size. Excitation wavelength λ = 700 nm.

These results show that the optical properties critically depends on the specific morphology of the sample which is related to the adopted deposition technique. On a

deeper analysis it is possible to conclude that the control of the crystallization procedure allows the semiconductor band gap and the intrinsic radiative lifetime of the compound to be engineered following specific requests from the final application.

5.4 Degradation of the Optical Properties

Little is known about the mechanisms of degradation that afflict perovskites. In the next chapter will be discussed in detail the forms of electrical instability of the PSC. In this paragraph, instead, are considered the variations of the optical properties related to the decay of the perovskites.

The principal degradation mechanism of $MAPbI_3$ perovskite is the reversible reaction to the relative precursors. This event occur often in presence of water in form of moisture[15]. The perovskite film turns its brownish colour to a yellowish tint which is typical of PbI_2 films. According to[16] the chemical reaction that takes place is:

$$4CH_3NH_3PbI_3 + H_2O \Leftrightarrow 4CH_3NH_3{\cdot}H_2O + H_2O \Leftrightarrow (CH_3NH_3)_4PbI_6{\cdot}2H_2O+3PbI_2$$

The reaction products have been recently confirmed by X-ray diffraction measurements of perovskite left in humid air for several days showing that the perovskite interacts with moisture in air to form the monohydrate $CH_3NH_3PbI_3{\cdot}H_2O$ and dihydrate $(CH_3NH_3)_4PbI_6{\cdot}2H_2O$ phases[17]. In ambient conditions CH_3NH_2 and HI slowly evaporate from the more weakly bonded hydrated phase as gases, eventually leaving behind PbI_2, a process which is greatly accelerated by elevated temperatures:

$$(CH_3NH_3)_4PbI_6{\cdot}2H_2O+3PbI_2 + heat \Rightarrow 4CH_3NH_{2(g)} + 4HI_{(g)} + 4PbI_{2(s)}$$

Interestingly, the degradation mechanism only in presence of moisture (not in nitrogen or vacuum) is accelerated when an electric field is applied to the perovskite with a dendrimental effect on the stability of the solar cell. To investigate this effect in figure 5.12 are reported the local absorption spectra (top panel) and the PL (bottom panel) for a perovskite film sandwiched between two lateral gold electrodes at different distances from the positively charged electrode[16]. The central area between the two electrodes is

indicated with bulk. The voltage applied between the electrodes is 60 V, with a distance between the electrodes of 1 mm. Moving from the bulk area to the region close to the electrode, it is possible to observe a reduction in absorption over the entire spectral region characteristic of the hybrid perovskite along with a blue shift of the absorption onset. The PL spectrum recorded away from the electrode peaks at 780 nm as typically reported for $CH_3NH_3PbI_3$. Moving to the region close to the electrode, the main emissive peak blue shifts and a further broadband appears around 600 nm which is likely related to the presence of PbI_2. It is also worthwhile to notice that the broad PL band and the absorption spectrum present at wavelengths shorter than 650 nm indicate the presence of highly defective PbI_2[18]. Moreover, the blue shifted $CH_3NH_3PbI_3$ PL in the degraded region indicates the presence of a residual fraction of 3D perovskite with strained crystalline structure which may represent the initial phase of the degraded products[19-20].

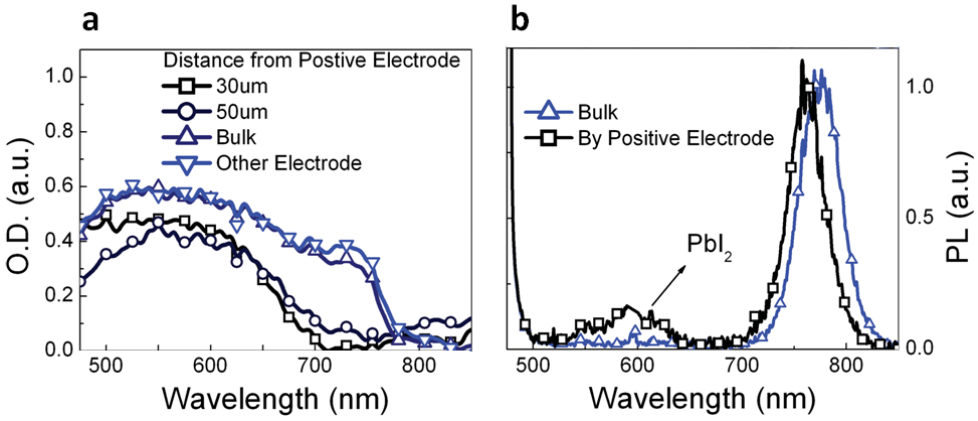

Figure 5.12: a) Absorption spectra taken at varying distances from the electrode that had been held at positive bias. b) Photoluminescence spectra in and out of the degraded region of the material.

The degradation reaction that occurs in presence of an external bias and in presence of water is:

$$(CH_3NH_3)_4PbI_6{\cdot}2H_2O+3PbI_2 + \textit{bias} \Rightarrow 4CH_3NH_3^+ + 4I^- + 4PbI_2$$

When the electric field is applied there is an accumulation of the ionic species at the interface with the respective electrodes, as demonstrated by *Huang et al.* [21]. However, the interaction between the perovskite and an applied electric field will be discussed in detail in the next chapter, since the presence of an external bias influences not only the

degradation mechanisms in air but completely change the electrical properties of the perovskite.

5.5 Conclusions

This chapter explained the optical properties of the perovskites used in solar cells. It was shown the crucial role of the substrate both in the crystallization conditions (i.e. temperature and annealing time) and in the variation of the optical properties. It was reported that mesoporous substrates in the optical properties of perovskite change passing through small crystallites contained in the mesoporous to large crystals of the capping layer. It was subsequently shown that this properties variation is linked to the size of the crystals themselves: the photoluminescence and the edge of the absorption spectrum shift to more blue values when the size of the crystals is reduced. Finally, the mechanisms of degradation in the optical properties caused by the presence of moisture and an applied electric field were introduced. It is seen that the result of the degradation is the dissociation of the perovskite in PbI_2 and volatile organic compounds. Therefore the need in the manufacture of the devices of the quality of encapsulation and also of the drying of the solar cells after any solution-based fabrication step prior to encapsulation, since both water and any polar solvents used during device fabrication can result in an increased deterioration.

References

[1] - NREL Website: http://www.nrel.gov.

[2] - L. Etgar, P. Gao, Z. Xue, Q. Peng, A.K. Chandiran, B. Liu, M.K. Nazeeruddin, M. Graetzel J. Am. Chem Soc. **2012**, 134, 17396.

[3] - M. M. Lee, J. Teuscher, T. Miyasaka, T. N. Murakami, H. J. Snaith, *Science* **2012**, 338, 643.

[4] - J. M. Ball, M. M. Lee, A. Hey, H. J. Snaith, *Energy Environ. Sci.* **2013**, 6, 1739.

[5] - P. Docampo, J. M. Ball, M. Darwich, G. E. Eperon, H. J. Snaith, *Nat. Commun.* **2013**, 4, 2761.

[6] - J.H. Heo, S.H. Im, J.H. Noh, T.N. Mandal, C.S. Lim, J.A. Chang, Y.H. Lee, H. Kim, A. Sarkar, M.K. Nazeeruddin, M. Gratzel, S.I. Seok *Nature Photon.* **2013**, 7, 486.

[7] - D. Liu, T. L. Kelly *Nature Photon.* **2013**, 8, 133.

[8] - Y. Sun, J. H. Seo, C. J. Takacs, J. Seifter, A. J. Heeger *Adv. Mater.* **2011**, 23, 1679.

[9] - D. Son, J. Im, H. Kim, N. Park *J. Phys. Chem.* **2011**, 118, 16567.

[10] - D.H. Kaelble *Dispersion-Polar Surface Tension Properties of Organic Solids*, The Journal of Adhesion **1969**, 2:2, 66-81.

[11] - C. Quarti, G. Grancini, E. Mosconi, P. Bruno, J.M. Ball, M.M. Lee, H.J. Snaith, A. Petrozza, F. De Angelis *J. Phys. Chem. Lett.* **2014**, 5, 279.

[12] - E. Mosconi, C. Quarti, T. Ivanovska, G. Ruani, F. De Angelis *Phys. Chem. Chem. Phys.* **2014**, 16,16137.

[13] - T. Baikie, Y. Fang, J.M. Kadro, M. Schreyer, F. Wei, S.G. Mhaisalkar; M. Gratzel, T.J. White *J. Mater. Chem. A* **2013**, 1, 5628.

[14] - N. Preda, L. Mihut, M. Baibarac, M. Husanu, C. Bucur, I.Baltog *J. Optoelectron. Adv. Mater.* **2008**, 10, 319.

[15] - T. Leijtens, G.E. Eperon, N. K. Noel, S.N. Habisreutinger, A. Petrozza, H.J. Snaith *Adv. Energ. Mater.* **2015**, 5, 20.

[16] - T. Leijtens, E.T. Hoke, G. Grancini, D.J. Slotcavage, G.E. Eperon, J.M. Ball, M. De Bastiani, A.R. Bowring, N. Martino, K. Wojciechowski, M.D. McGhee, H.J. Snaith, A. Petrozza. *Adv. Energ. Mater.* **2015**, 5, 20.

[17] - A. Leguy, Y. Hu, M. Campoy-Quiles, M. I. Alonso, O. J. Weber, P. Azarhoosh, M. van Schilfgaarde, M. T. Weller, T. Bein, J. Nelson, P. Docampo, P. R. F. Barnes, *Chem. Mater.* **2015**, 27, 3397.

[18] - A. E. Dugan, H. K. Henisch, *Phys. Rev.* **1968**, 171, 1047.

[19] - V. D'Innocenzo, A. R. S. Kandada, M. De Bastiani, M. Gandini, A. Petrozza, *J. Am. Chem. Soc.* **2014**, 136, 17730.

[20] - J. A. Christians, P. A. M. Herrera, P. V. Kamat, *J. Am. Chem. Soc.* **2015**, 137, 1530.

[21] - Z. Xiao, Y. Yuan, Y. Shao, Q. Wang, Q. Dong, C. Bi, P. Sharma, A. Gruverman , J. Huang, *Nat. Mater.* **2015**, 14, 193.

Chapter 6
Electrical Properties of Perovskite Solar Cells

Previously it was already introduced how this new material has captured the interest of many researchers. However, as for the optical properties, also the knowledge of the electrical characteristics of the organo-lead perovskite has not progressed in parallel to the development of the devices, remain largely misunderstood.
In the previous chapter the optical properties of perovskite layers were introduced. This chapter is dedicated to the detailed description of the electrical properties, with particular attention to the stability of the devices and their performances.

6.1 The current/voltage curve.

In chapter 1 the operations of a solar cell were introduced. It was reported that a solar cell device behaves like a diode in dark conditions, while, when illuminated, the current curve shifts by a factor which is related to the photocurrent generated (the short-circuit current J_{sc}). To determine the final efficiency of a device it is necessary to determine the relative current/voltage characteristic. This measure consists in applying to the solar cell several potential (from negative values to positive values) measuring the corresponding output current. In this way it is possible to obtained the three basic parameters that determine the ultimate efficiency of the cell: the short-circuit current (J_{sc}), the open circuit voltage (V_{oc}) and the fill factor (FF). For a working device these parameters must be stable over the life-time of the solar cell, any variation is reflected in the changes of the performances which means an intrinsic electrical instability of the solar cell. Figure 6.1 shows the measurement protocol of the current/voltage characteristic, defined below as J/V curve, for a hypothetical solar cell. As anticipated, the measure consists in applying different potentials to the cell (which reflect hypothetical workloads), starting from the reverse condition ($V_{applied} < 0$) and proceeding in a forward direction ($V_{applied} > V_{oc}$). The curve is recorded in light and dark. From the J/V curve other important information can be obtained like the series resistance and shunt resistance of the solar cell, which, however, will not be taken into account in the further discussion of this chapter. It must be noted that if the direction of the measurement is reversed (i.e. it starts from forward condition) the relative current must follow the same of the direct scan.

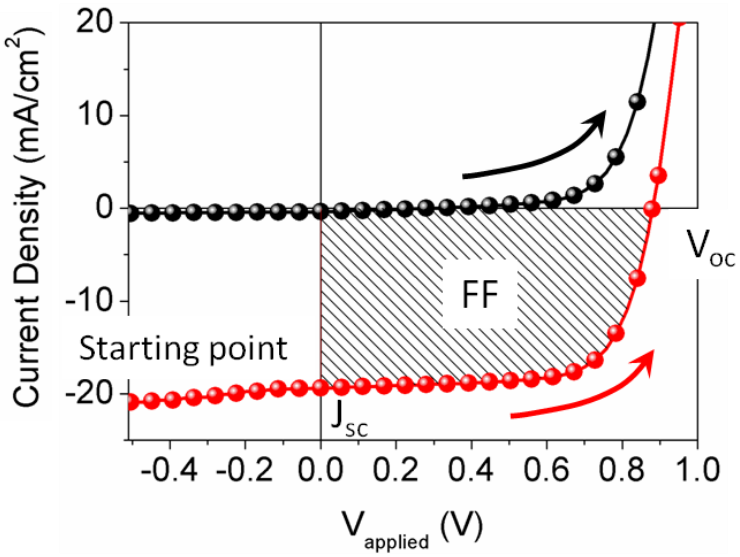

Figure 6.1: Current/voltage characteristic for a typical solar cell in dark (black curve) and in light (red curve). The main parameters are also reported. Arrows indicate the voltage scan direction.

6.2 The phenomenon of the "hysteresis"

Some Perovskite Solar Cells (PSC) architectures have a special characteristic in the J/V curves. In particular, mesoporous configurations and flat standard junctions (see chapter 2 for a description of the device) present a sort of anomaly in the determination of the J/V characteristic: the output values of the current vary according to the conditions of measurement[1]. This phenomenon creates a relevant problem in the final determination of the efficiency of the device and reveals an unstable nature of the electrical properties of these cells. The parameters that influence the measurement are mainly three: the scanning direction of the applied potential, the scan rate, and pre-treatments conditions.

- The scan direction. The conventional measure of a curve J/V provides that the scan starts from negative potential (*reverse*) and finishes to positive potential over the Voc (*forward*). If the scan direction is switched, that is, starting forward and ending in reverse conditions, the curve must coincide with that of the conventional one. In the case of some PSC the highest efficiency is obtained by performing a measurement in reverse, starting from potential over the Voc. If the measurement is repeated under conventional conditions the efficiency decreases primarily for a decrease in the fill factor.

- The scan rate (in V/s) is determined by the time taken to make a sweep of potential applied. In other words, how long a certain potential is applied before moving to the next value, at a fixed number of steps. To reflect the real working conditions of a solar cell it is necessary that the scan rate is sufficiently slow to simulate real load conditions. Typical values of scan rate are 0.1-0.2 V/s[1]. In some PSC the scan rate greatly affect the final performance. High efficiencies are obtained with high scan rate (10 V/s or more) that remarkably deviate from stationary working conditions[2]. If the scan rate decreases to conventional values the cell efficiency decreases considerably due to a strong decrease of the short-circuit current.
- Pre-treatments conditioning: this parameter regards all the processes that are carried out before measuring the solar cell. Mainly it refers to two phenomena: the light-soaking and pre-bias. With light-soaking it means a process of exposure of the cell to 1-sun light for a certain period of time. During this process the cell terminals are disconnected and the device is in a state of open circuit. This process is used to activate some light-induced phenomena such as self-doping of certain materials or electrical activation of the titanium oxide. This process occurs naturally when a solar panel is exposed to sunlight and therefore not considered in negative terms. Pre-bias means any electrical treatment before the measure of the J/V curve. A fixed potential value (both in forward or reverse conditions) is applied to the device for a certain amount of time (seconds to min) and immediately after, the sweep of potential is collected. This process does not occur naturally in working condition and is likely to create artificial results due to the effects of the applied electric field. Some PSC require these types of treatment to show high efficiencies. In particular, light-soaking is necessary for the cells that present a scaffold mesoporous of TiO_2[1], while pre-bias with a forward potential is necessary for cells with mesoporous Al_2O_3 and standard flat cells[3].

In figure6.2 are summarized the effects of scan direction and scan rate for a mesoporous Al_2O_3 and a flat standard perovskite solar cells. Both cells are pre-biased at 1.4V for ten seconds before the first measurement.

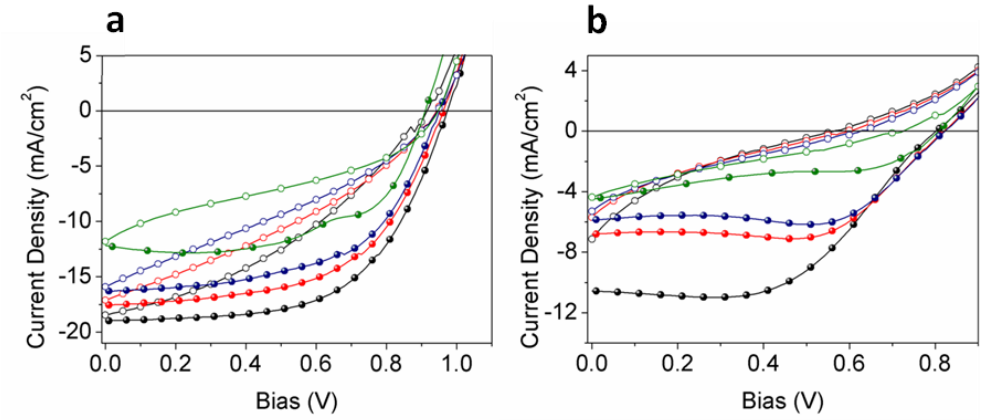

Figure 6.2: The effects of scan direction and scan rate for a Al_2O_3 mesoporous (a) and standard flat (b) perovskite solar cells. Scan direction: reverse to forward (hollow dots) and forward to reverse (full dots). Scan rate variations: fast (10 V/s - black lines) to slow (0.2 V/s - green lines).

All these phenomena represent a certain electrical instability in perovskite cells that has been defined by the term "hysteresis" due to the similarity to the hysteretic phenomena. It is a radical problem that afflicts substantially the determination of the efficiencies of the cells, which makes their classification problematic at an absolute level. This is why the PSC in the NREL chart are defined as "not stabilized". In addition, the hysteresis phenomenon is also manifested in the stability and in the life-time of the cells, as seen from the dependence on the scan rate. Understand, solve and fix this problem become a milestone in the perspective of the real development of the PSC.

6.3 The role of the cells configuration

In chapter 2 different configurations, better defined as architectures, of Perovskite Solar Cell were introduced. The variation of the architecture interestingly has shown a diverse response at the hysteretic phenomenon. The greatest hysteretic effect is present in cells with mesoporous Al_2O_3 and standard flat junctions that use TiO_2 and SPIRO-OMeTAD as extraction layers for electrons holes, respectively. The hysteresis decreases significantly if the mesoporous Al_2O_3 is replaced with mesoporous TiO_2, then it disappeared completely in the case of inverted architectures that use as interlayer PEDOT: PSS and PCBM. In figure 6.3 is reported the reduction of the hysteresis in the J/V characteristics for three different device architectures as a function of the scanning rate and direction

together with the respective architecture: mesoporous Al_2O_3, mesoporous TiO_2 and inverted configuration.

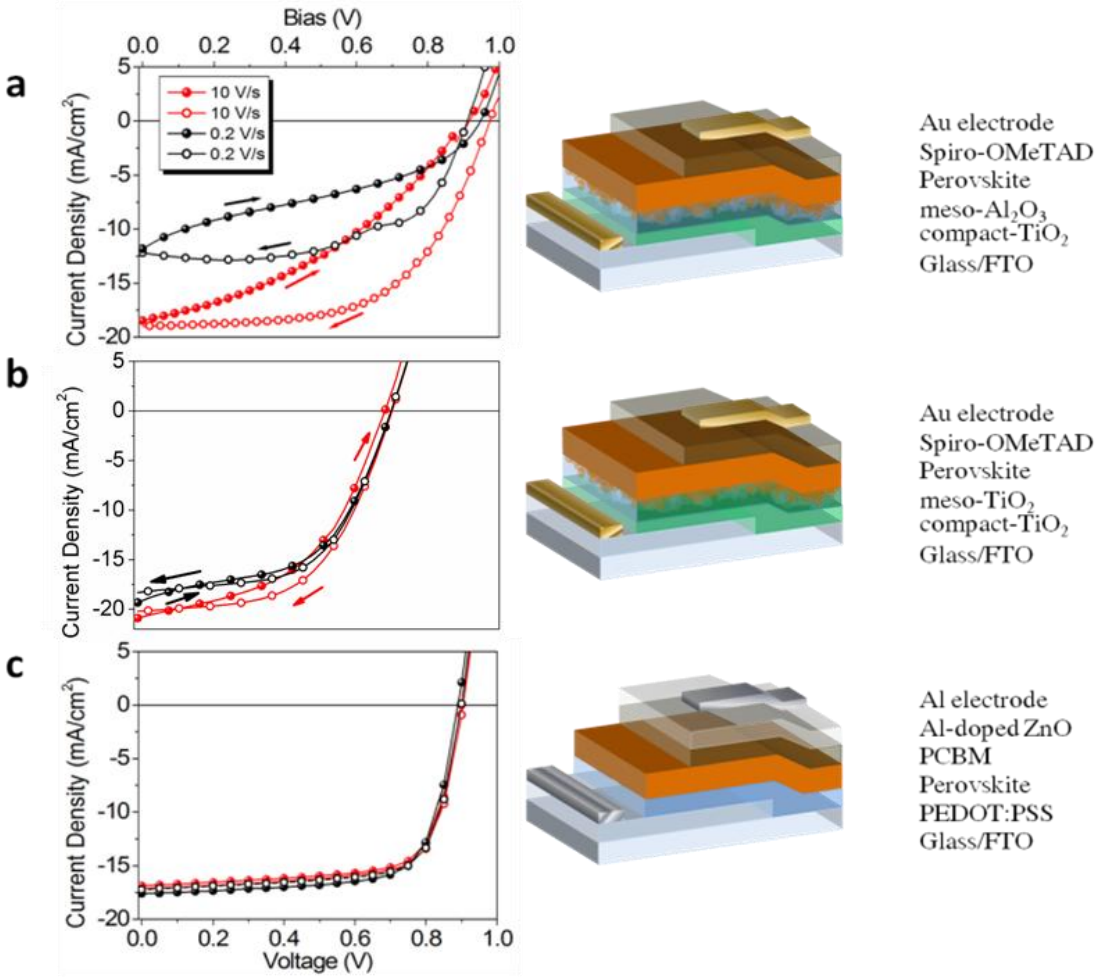

Figure 6.3: J/V characteristics of three different device architectures. a) Mesoporous Al_2O_3 based device, b) mesoporous TiO_2 based device, and c) inverted device. The current density is plotted as a function of voltage scan direction (hollow dots: from forward to reverse conditions; full dots: from reverse to forward conditions) and as a function of the scan rate (red line: 10 V/s; black line: 0.2 V/s). For each device the sketch of the structure and the interlayers used are reported in the right panels.

The architecture encompassing the mesoporous Al_2O_3 layer and a flat TiO_2 as electron extracting layer is affected by severe hysteresis features, with a strong reduction of the photocurrent when the scanning rate is slowed down. The phenomenon is attenuated by replacing the mesoporous alumina with a mesoporous TiO_2 extraction layer. This effect finally becomes negligible when electron extraction occurs at the interface with

PCBM, in an inverted structure. This trend already highlights a role of the charge extraction interface in the response of the device to slow transient phenomena. It must be noted that the curves of figure 6.3 have been obtained after a specific conditioning. In particular, the curves of figure 6.3a,b are observed only by scanning the device starting from a pre-biasing at 1.4 V for 10 s, without that the photocurrent is highly suppressed. On the other hand, even the hysteresis-free behaviour of the inverted device of figure 6.3c is obtained only after scanning the J/V characteristic of the same device several times, as shown in figure 6.4a, while a pre-bias at 1.4 V under light is highly detrimental resulting in a reduction of the short circuit current (figure 6.4b).

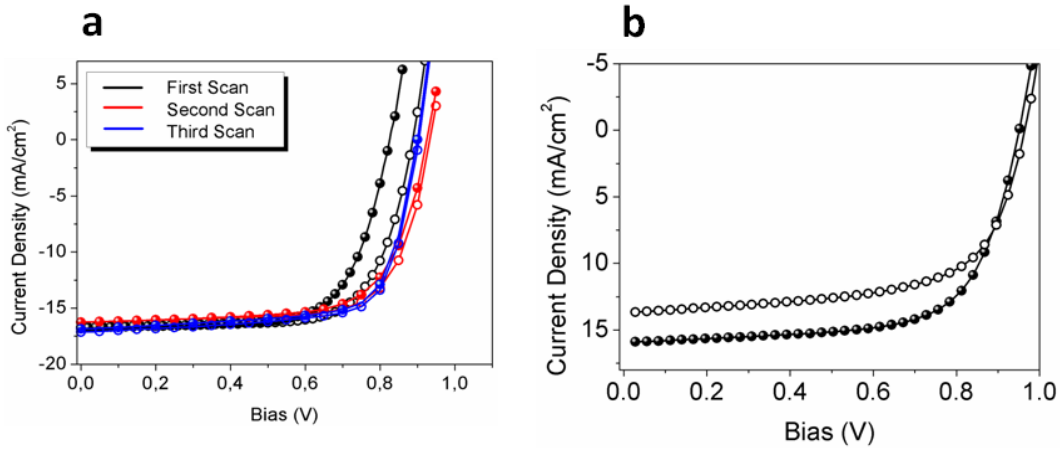

Figure 6.4: a) J/V characteristics of an inverted device repeated several times consecutively. Hollow dots: from forward to reverse; full dots: from reverse to forward. Scan rate 10 V/s . b) The effect of pre-bias at 1.4 V for an inverted device. Full dots, without the pre-bias. Hollow dots with pre-bias.

The figures of merit of the devices reported in figure 6.3 and details about their testing procedures are reported in Table 6.1. It must be noted that only through a clear description of the testing protocol used for the measurements of the J/V curves it is possible to extract useful information regarding the development of PSC. Incomplete or unclear measurements analysis lead to misjudge the devices with the risk of an overestimated final efficiency.

	Start Point [V]	End Point [V]	Stabilization Condition	Direction	Scan Rate [V/s]	Voc [V]	Jsc [mA/cm^2]	FF [%]	PCE [%]
TiO2/Al_2O_3meso/ PVK/Spiro	1.4	0	1.4 V, 10 s Light	OC-SC	0.2	0.91	12.18	61	6.79
					10	0.97	18.97	58	10.76
	0	1.4	No	SC-OC	0.2	0.95	11.81	34	3.81
					10	0.92	18.46	37	6.31
TiO_2/TiO_2meso/ PVK/Spiro	1.4	0	1.4 V, 10 s Light	OC-SC	0.2	0.70	18.33	58	7.25
					10	0.70	20.22	55	7.78
	0	1.4	No	SC-OC	0.2	0.70	19.34	52	6.95
					10	0.68	20.9	49	6.90
PEDOT:PSS/ PVK/PCBM	1.4	0	No	OC-SC	0.2	0.90	17.22	72	11.23
					10	0.90	17.13	72	11.14
	0	1.4	No	SC-OC	0.2	0.90	17.59	72	11.25
					10	0.90	16.86	72	10.91

Table 6.1: Performances of the standard and inverted perovskite solar cells versus the voltage scan direction and the scan rate. OC: open-circuit; SC: short-circuit.

Now, it is interesting to investigate the different behaviour of the inverted device. During the first J/V measurement performed on a freshly made device, the latter exhibits clear hysteresis when scanning the voltage from forward-bias to short-circuit and back. By repeating the measurement this difference is reduced, ultimately becoming negligible and producing the hysteresis free scans reported in figure 6.3c. In particular, while the short-circuit current is almost unaffected upon several scans, the open-circuit voltage needs a few cycles to be stabilized: evidently, what is at the base of the transient phenomena does not necessarily affects both parameters at the same time. A similar phenomenon is also present in the dark J/V curves, see figure 6.5. This shows the clear need of some “preconditioning J/V cycles” to reach a stable performance, even for an inverted device.

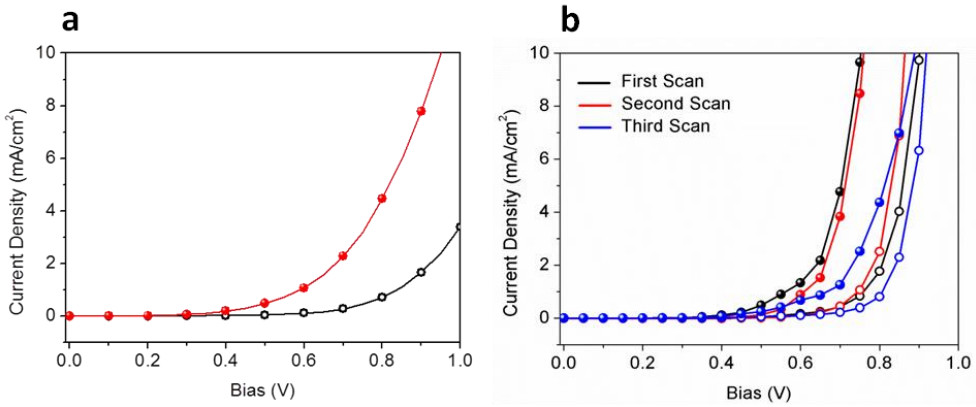

Figure 6.5: Presence of the hysteresis also without illumination for a standard flat device (a) and for an inverted device (b). For the latter are reported also the preconditioning cycles. Hollow dots: from reverse to forward bias, full dots from forward to reverse bias.

6.4 The nature of the Hysteresis

The hysteresis effect that afflicts the PSC is a problem that can be solved, as seems in the inverted configuration. However the very nature of this problem requires a complete understanding so that it will be possible to continue the optimization of the devices and architectures towards a stable and increasing efficiency. In the previous paragraph it was reported that the inverted devices after a specific treatment lose their hysteretic character. *Huang et al.* [4] assigned this beneficial effect at the presence of PCBM that is able to passivate the surface states of the perovskite rich of defects. The idea that the hysteresis is resulting from the presence of trap states induced by the crystallization processes has been the first explanation proposed[4-5]. These defects create energy levels accessible within the band gap of the perovskite, forming traps for the photogenerated charges. The filling of these states can be made by pre-treatment processes such as light soaking and pre-biasing. The problem of this theory is that the dynamics of the mechanisms of trapping and detrapping take place on the order of micro to milliseconds, while the processes that give rise to the phenomena that affect the hysteresis are much slower and occur in the order of seconds or minutes. This becomes clear by looking at the evolution of the current in time for a device at a given potential. In presence of hysteresis, both in light and in darkness the current is not stable over time making a transient evolution that lasts several minutes before stabilizing to a certain value. Figure 6.6 shows the transient in the dark current for a flat

standard device at 1.4 V. The evolution of the dark current over time is in agreement with the variations of the performances related to the different scan rate and direction and shows that: 1) the effect of the hysteresis is not necessarily linked to the presence of light (as already anticipated in figure 6.5) and 2) the time range in which hysteresis works is a lot slower mechanisms respect to trapping and detrapping dynamics.

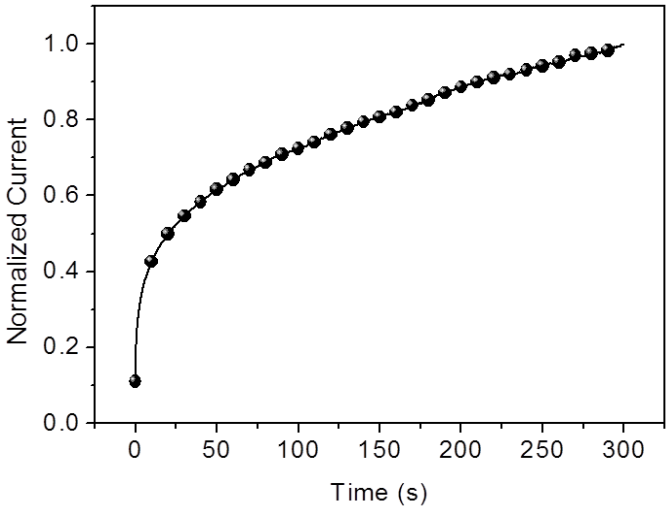

Figure 6.6: Evolution of the dark current under a constant bias of 1.4 V for a flat TiO2/perovskite/SPIRO-OMeTAD device.

A subsequent assumptions about the nature of the hysteresis was the idea that the hybrid perovskite has a ferroelectric character. The nature of the ferroelectricity would be found in the dipole moment present in the organic component ($CH_3NH_3^+$), which, in the presence of an electric field (external or internal considering the built in) rearranges rotating along the main axis and aligned along the lines of field[6-7]. The orientation of these dipoles would be opposed to the internal/external electric field and then would go to modify the properties of extraction of the charges. The dynamics of this mechanism is in agreement with the slow transients measured and with theoretical calculations provided for the rotation of the organic cation[8]. However this hypothesis has been recently discarded from a publication by *Snaith et al.*[9] which shows that replacing the organic cation with an atom of caesium does not decrease the hysteretic behaviour. Without any dipole moment the origin of the hysteresis cannot be ferroelectric.

A third theory proposes that the nature of hysteresis is due to the motion of the ionic species occurring within the perovskite in the presence of an electric field. According to this idea the perovskite behaves like an ionic conductor whose charges (anions and

cations) are able to drift along the electric field, accumulating at the interfaces between the various grain boundaries of the crystallites and the extraction layers. *Huang et al.*[10] have shown that the result of this accumulation of ions generates two doped zones at the side of the perovskite layer *p* or *n*, depending on the ion species accumulated (cations or anions, respectively). The movement of these ions and the relative accumulation substantially change the electrical properties of perovskite. In fact, the moving ions create an ionic current which has the same direction of the photogenerated charges. Furthermore due to their accumulation the ions change the electrical properties at the interface with the extraction layers. This hypothesis is well confirmed by the experimental observations of the hysteresis effects in the solar cell. The ions movement is independent by light exposure and their dynamics are in agreement with the slow transient evolution of the current. The main consequence of these factors is that the very nature of hysteresis is an intrinsic property of perovskite. It therefore remains unclear why some devices do not show a hysteretic behaviour (such as inverted architectures). The main difference between a device with and without hysteresis is the different nature of interlayers used. It has been already mentioned that the presence of PCBM appears benign in terms of reducing the hysteresis[4], it becomes essential to understand the physics that occurs at the interface between the perovskite and the charge extraction layer in operating conditions.

6.4.1 The Photophysics at the Interfaces

With the intent of clarifying the role of PCBM in the inverted structure, first must be explained the reason behind the short-circuit current stability compared to the cells integrating a TiO_2 layer. Figure 6.7a compares the photoluminescence (PL) quenching of perovskite forming a flat junction with TiO_2 and PCBM. Comparing these dynamics with the PL decay of a reference perovskite sample deposited on a glass substrate, it is possible to notice that the PCBM induces a considerable quenching, while in the presence of TiO_2 the quenching is nearly negligible (please note that crystal size effects cannot explain such large change in PL dynamics see chapter 5). From these results it can be safely assumed that that the perovskite surface will be improved upon PCBM deposition [4] rather than inducing interface trap states. A first conclusion is that PCBM

provides superior charge extraction properties with respect to TiO_2 . To better explain these results with what is generally observed in working devices, in figure 6.7b are reported the PL dynamics of perovskite embodied in a full inverted at short-circuit condition. In particular is compared the PL decay, at early times after photoexcitation (ps-ns), before and after a pre-biasing the device at 1 V. The dynamics do not change dramatically. Therefore it can be concluded that electron transfer is not affected by polarizing the perovskite film, consistently with the observed short-circuit current stability.

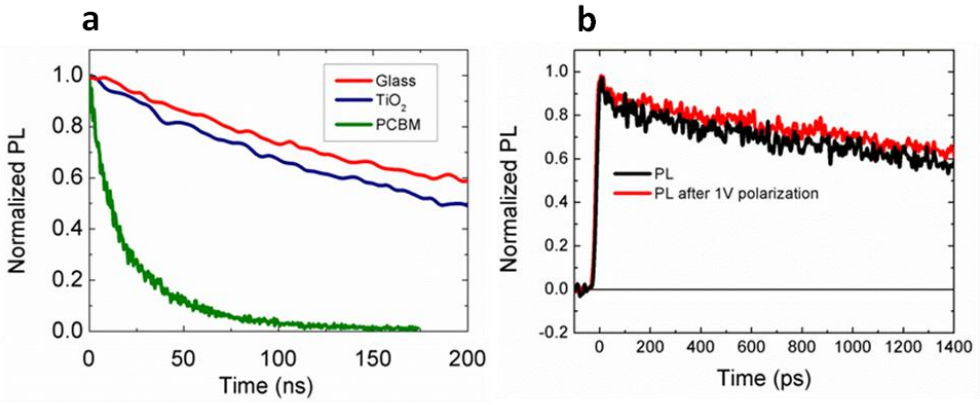

Figure 6.7: PL dynamics from CH perovskite/TiO_2 and perovskite/PCBM bi-layer and from perovskite deposited on glass; b) PL dynamics from perovskite embodied in a inverted architecture. The device was under short-circuit condition before (black line) and after (red line) a pre-polarization (1 V) treatment (probed wavelength 780 nm, excitation wavelength 700 nm).

For comparison, in figure 6.8 it is reported the photobleaching (PB) dynamics, in the ps-ns time window, of the same hybrid perovskite, probed in particular standard devices where SPIRO-OMeTAD was used as hole extracting material, while PCBM or TiO_2 are used as electron extracting layers[2]. The dynamic of the PB is compared with the PL dynamics taken from the inverted device. The photobleaching originates from the transparency induced at the onset of the optical absorption of a semiconductor upon photoexcitation after population of the bottom of conduction band and top of the valence band, respectively, thus it is a good indicator for the electron and holes population dynamics in the semiconductor[11-12]. When the PCBM is used, the PB dynamics well follow the PL dynamics of the inverted devices and they are not affected by pre-biasing of the device. On the other hand, in the presence of TiO_2 , the charge extraction becomes faster, and comparable to those in the presence of PCBM, only upon

pre-biasing. This is indicating, first of all, that the electron extracting interface is the most sensitive and critical one in state-of-the art perovskite solar cell architectures as electron extraction strongly depends on the nature of the interface and on the thin film polarization condition, while no significant change is observed by changing the hole extracting layer. Then, importantly, there is also the evidence that, differently from flat TiO_2, PCBM provides such good electronic contacts at the interface with perovskites that the extraction is not influenced by pre-biasing of the device. This well explains the steady state photocurrent stability found in the presence of PCBM.

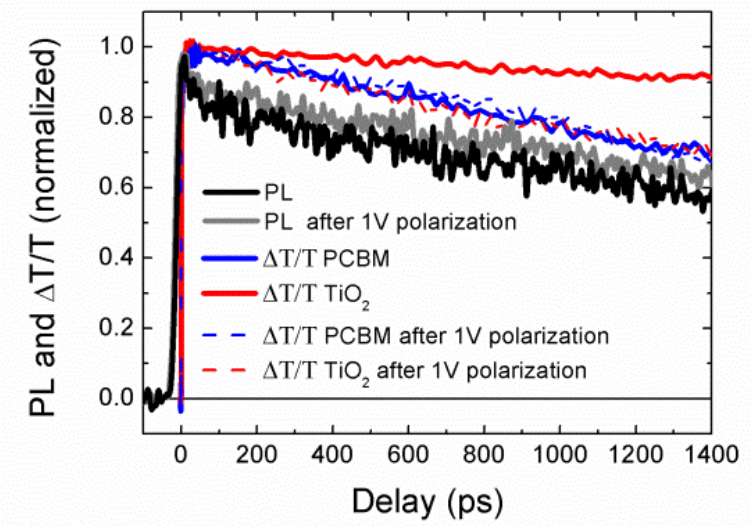

Figure 6.8: PL dynamics from perovskite in an inverted device in short-circuit condition before (gray line) and after (black line) a pre-polarization (1V) treatment. The PL dynamics are compared to the Photo-bleach dynamics (dotted lines) measured by Transient absorption spectroscopy ($\Delta T/T$) from perovskite embodied in standard architectures with SPIRO-OMeTAD as hole extracting layer and PCBM or TiO_2 as electron extracting layer.

6.4.2 The Effects of the Bias

Once clarified the fundamental role of the interface perovskite/electron extraction layer it is necessary to explain in detail the effects of the electric field in the phenomena that affect the hysteresis. For the sake of clarity, it is defined with the term of *poling* the polarization of a semiconductor (in this case the perovskite) through the application of an external electric field. To appreciate the effect of the electric field it is necessary to realize specific devices that do not present a built in internal field, that would otherwise alter the effects of the applied field[10]. For this reason devices with only lateral

symmetric gold contacts are realized with a distance between the two electrodes of 20 µm in which the semiconductor is deposited (see figure 6.9).

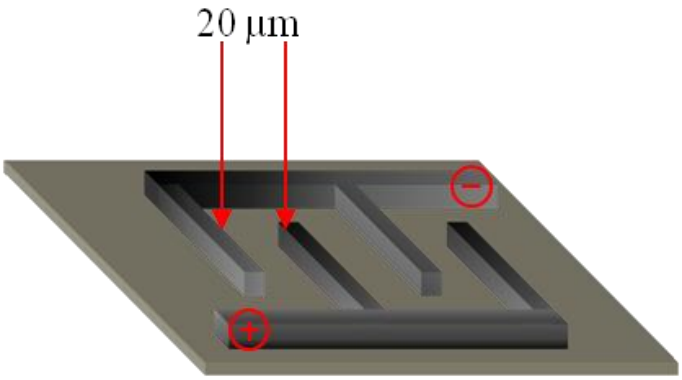

Figure 6.9: Sketch of the patterned electrodes used for the lateral devices. Thickness of the electrodes: 15 nm.

With the aim of studying the interaction between the perovskite and PCBM which seems behind the stabilization process highlighted in figure 6.4, a systematic investigation on the poling effects on pristine perovskite and perovskite/PCBM is performed (figure 6.10). The poling is applied to both samples by biasing them in dark conditions in order to be able to disentangle the effects strictly related to the device polarization from eventual light induced effects. All the experiments are performed in inert atmosphere. Without any prebiasing, the current–voltage characteristics recorded from 0 V to +28 V and from 0 V to −28 V on pristine perovskite and bi-layer samples are symmetric, with similar current values (figure 6.10a,b black lines). When the two samples are prebiased by applying a field of 1.4 V/µm, the symmetry in the curves is lost and the current exhibits a rectifying behaviour. This effect is the consequence of the partial positive and negative charges induced at the contacts that hamper the injection of charge at an applied voltage which is opposite with respect to the prebiasing, as suggested by Huang and co-workers[10]. Furthermore, it must be noted that by inverting the polarization between the two electrodes (indicated henceforth as positive and negative poling), the switching of the I/V characteristic is not instantaneous, as it requires minutes-to-hours in order to recover the initial condition. Huang and co-workers reported this effect for the first time for pristine perovskite under light illumination[10]. They concluded that it is the result of ions drifting through the perovskite, forming two doped regions, *n* and *p* , next to the electrodes, according to the voltage applied. Interestingly, figure 5.9b shows that

the presence of PCBM deposited on top of the perovskite layer does not apparently hamper the ions drift, as the loss of symmetry in the curves demonstrates. The only difference induced by the presence of PCBM is an increased value of the forward current under poling conditions.

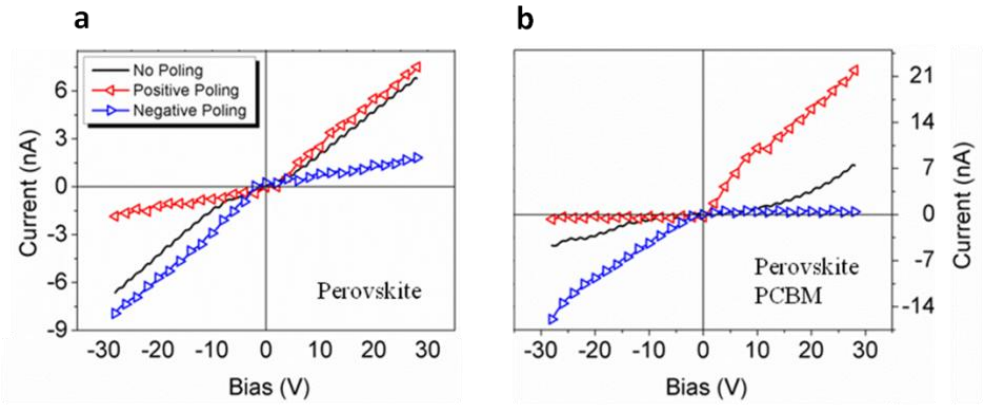

Figure 6.10: Current/voltage characteristics of lateral symmetric devices under poling conditions of a) perovskite and b) perovskite/PCBM: black line, no poling; red line, first polarization on a fresh sample; blue line, switched polarization on a fresh twin sample. The arrows indicate the directions of the voltage scan. Scan rate = 25 V/s, poling time = 120 s, field applied 1.4 V/µm.

From these results it is possible to summarize that: 1) the ion migration, proposed to be responsible for the formation of an internal field within the planar device with symmetric contacts, is observable not only under light illumination but also in the dark; 2) under polarization, the presence of PCBM does not prevent the ions drifting. Thus, ions diffusion/drifting is still present in solar cells with a PCBM electron extracting layer, even if the short-circuit current (i.e., charge extraction) is stable upon scanning.

The presence of PCBM in the planar sample increases the absolute values of the forward current. Though one can assume that PCBM diffusion in the perovskite thin film may induce a better morphology (compactness) of the thin film[4], however this can be excluded as the origin of the enhanced current because, without prebiasing, the current values are similar with or without PCBM.

To pin down the origin of the enhanced forward current when the perovskite/PCBM bi-layer is prebiased, in figure 6.11 is reported the time evolution of the current upon polarization, with and without PCBM, on a time scale of hundreds of seconds for both samples of figure 6.10 (please note that these are twin fresh samples respect of the ones studied in figure 6.10 in order to avoid artefacts in the measurements).

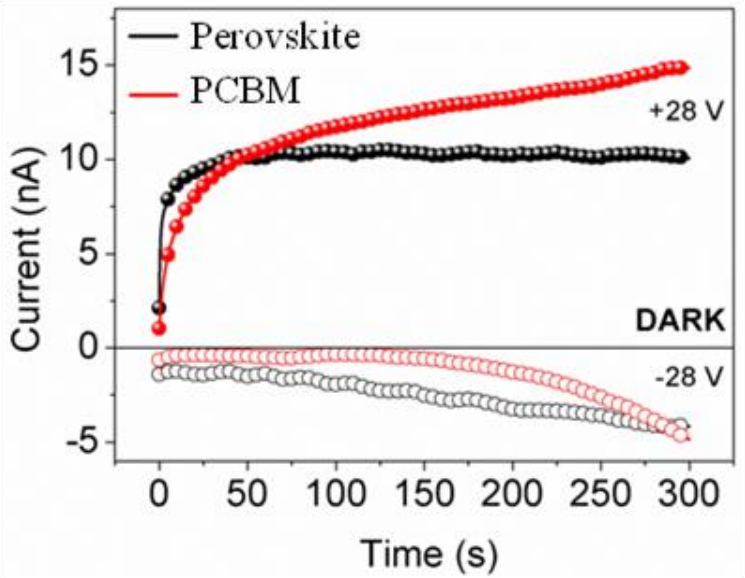

Figure 6.11: Evolution of the dark current under poling condition for lateral devices of perovskite (black) and perovskite/ PCBM (red). First polarization: full dots, switched: hollow circles. The inversion of the polarization is instantaneous. Voltage applied ± 1.4 V/µm.

Under poling, the pristine film (full dots, black line) shows an enhancement in current in the first 60 s until a plateau value is reached. This initial rising is attributed to the creation of the doped junction, via ions drifting, which is completed when the current stabilizes. In the presence of PCBM (full dots, red line) the transient dynamic is slowed down; however, the absolute value of the current increases without reaching a stabilized point in our time scale. This behaviour is not symmetric when the poling is instantaneously inverted between the two electrodes (hollow circles). In this condition the absolute values of the currents are strongly reduced and slowly increase for both films, again with a slower dynamic for the perovskite/PCBM film. Such slow dynamics clarify that the current enhancement in the presence of PCBM is also related to the migration of ions. Upon fabrication of the perovskite/PCBM bi-layer it can be assumed that the small organic molecules intercalate the perovskite grain of the polycrystalline film, thus forming also lateral PCBM/perovskite interfaces. These observations throw the idea that upon polarization, ions do interact with the organic compound, increasing the overall conductivity of the film. In the solar cell with PCBM as electron extracting layer, since ions, along with the photogenerated carriers, drift toward the electrodes due to the built-in voltage, an interaction of such species with the extracting layers is possible. Recent experimental[13-15] and theoretical[16-17] investigations have indicated iodide ions,

I^- , and Methylammonium ions, MA^+, as the most probable anionic and cationic species which can diffuse and/or drift within the perovskite absorber.

As a consequence of the built-in field deriving by the different contacts work-function, during cell operation iodide ions are expected to accumulate close to PCBM, while MA^+ close to the hole extracting contact[18]. The actual possibility for MA^+ to drift under the influence of a field is currently being debated. Recent theoretical studies predict a high activation barrier (0.84 eV)[16] while others derive a barrier consistent with MA^+ motion (0.46 eV)[17]. Some experimental works[13-14] agree with the latter, probing an accumulation of MA^+ upon polarization of perovskite thin film at the negatively polarized electrode, however these experiments were performed in air or in a polar environment. There is instead theoretical agreement on the migration of I^- [16-17], with however limited experimental evidence in inert atmosphere due to the poor sensitivity of the experimental techniques used.

After having clarified the particular characteristics which concern the perovskite in the presence of an electric field, it is necessary to explain in detail the consequences of the drifting of iodide as an effect of a field developing across the semiconductor and subsequently the relative interaction with PCBM. A valid way to prove the nature of the negatively charged mobile ions migrating within the perovskite is the biasing, in dark and nitrogen atmosphere, of a sample composed of a pair of planar and symmetric silver electrodes, on top of which a pristine perovskite layer is deposited. Silver is the suitable candidate due to its selective interaction with iodide, forming metal halides compounds. In figure 5.12 is reported the Scanning Electron Microscopy (SEM) images of the thin film deposited on the metal contacts in pristine conditions (5.11a) and upon biasing (5.11b). After biasing, differently from what observed previously with the samples based on gold electrodes, it is not possible to register any I/V curve and can be observed that the area corresponding to the positively biased electrodes results damaged, while the negatively biased electrodes appear unmodified. This provides evidence of the electro-migration of the I^- ions toward the positively biased electrode and their reaction with Ag.

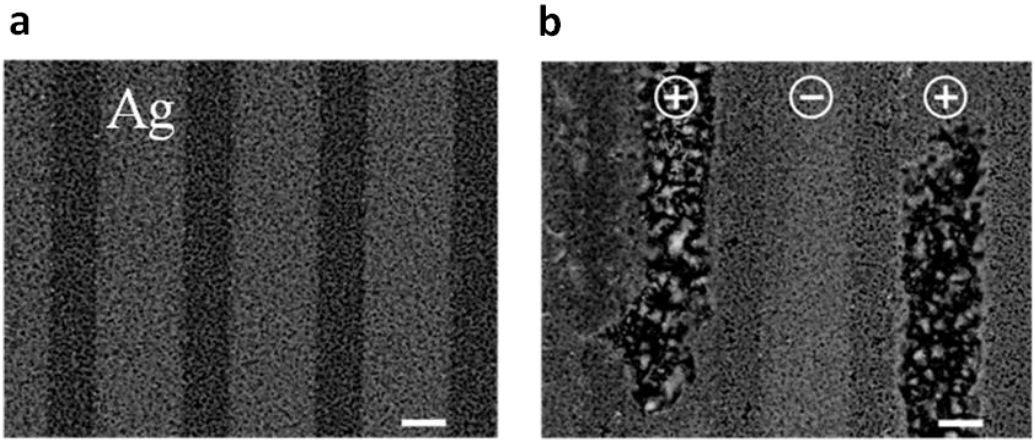

Figure 5.12: SEM top view of the perovskite lateral device with silver electrode a) before and b) after the poling. The different electrode polarizations are reported with the “plus” and “minus” symbols. Scale bar 20 µm.

6.4.3 The role of PCBM

It is well reported in the literature that PCBM can interact with alkyl ammonium salts resulting in a doping of the material itself [19]. In particular these salts act as *n*-dopants of the fullerene derivatives, increasing their conductivity by several orders of magnitude. It is worth to test this phenomenon with the ionic compounds that are used for the synthesis of perovskites. The first manifestation of a possible doping of the fullerene can be studied by comparing the conductivity measurements of a pristine film of PCBM and one film of PCBM with a controlled amount of I^-. The latter is realized by adding Methylammonium iodide (MAI) solution (10 mg/mL in Isopropanol) to the pristine PCBM solution (30 mg/mL in Chlorobenzene) with a ratio of 1:30. In figure 6.13, is reported the J/V plot of the two films. For this test are used symmetric gold contacts with a channel length of 200 µm in order to avoid contact resistance effects. The addition of the MAI salt to the PCBM results in a markedly increased conductivity, which changes from 6.43 × 10^{-7} S/m for the pristine film to 4.35 × 10^{-6} S/m for the PCBM/MAI film. This effect may be ascribed either to a chemical doping of the PCBM, i.e., an excess of free carriers, or to an improved mobility, or both.

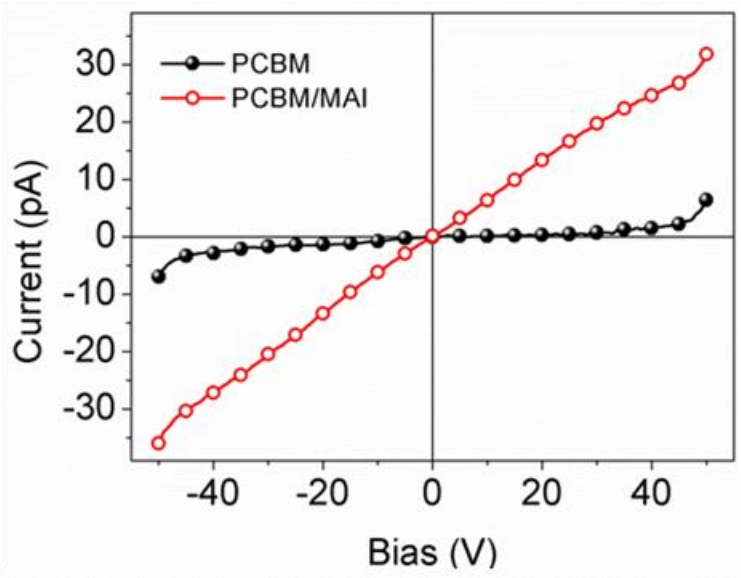

Figure 6.13: J/V curves of PCBM (black full dots) and PCBM/MAI (red open circles) films.

In order to get deeper insights, the electronic properties of a PCBM film and a PCBM/MAI film are tested in a top gate/bottom contact field-effect transistors (FETs). By comparing the measurements (figure 6.14) of the pristine PCBM and the MAI doped devices, it is possible to extract useful information regarding the PCBM interaction with ions that validate the aforementioned PCBM/perovskite interaction. The extracted saturation mobility (at $V_G = V_D = 60$ V) results in being 5.9×10^{-2} cm^2/Vs for the pristine PCBM transistor - in agreement with literature values [18-19] - and 0.15 cm^2/Vs for the doped PCBM/MAI device. The latter value is more than two times higher than the pristine PCBM one. The pristine PCBM device shows poorer subthreshold slope values and a higher threshold voltage (36.3 V, which reduces to 8.1 V upon doping), likely owing to deep trap states. The holes current tail exhibited at low gate voltages in the saturation regime by the pristine PCBM device disappears in the MAI doped one, resulting in a suppressed hole conduction. At the same time, a marked increase of the nongateable OFF current in saturation in the MAI doped devices denotes a conductivity increase of the semiconducting film, confirming the results reported above for the two terminal devices (in the linear regime the OFF currents are at the level of leakage and cannot be compared). The generally increased performances (table 6.2) of the doped device, with respect to the pristine one, can be attributed according to the literature[20] to an increased concentration of excess carriers, as a consequence of chemical doping which shifts the Fermi level closer to the LUMO level of PCBM.

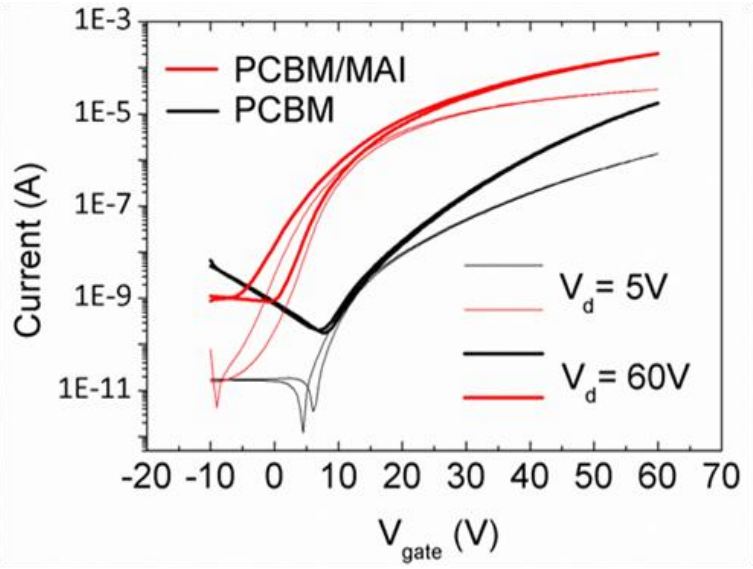

Figure 6.14: Transfer characteristics of the pristine PCBM top gate bottom contact transistor (black) and of the MAI doped PCBM device (red). Thick lines: saturation regime, thin line: linear regime.

	Electron Mobility [cm^2/Vs]	Threshold Voltage [V]	I_{ON}/I_{OFF}	Subthreshold Slope [V/dec]
PCBM	$5.9\ 10^{-2}$	36.3	10^6	6
PCBM/MAI (30:1)	0.15	8.1	10^7	3

Table 6.2: Device parameter comparison for pristine PCBM and MAI doped PCBM transistors.

To confirm the shift of the Fermi level, ultraviolet photoelectron spectroscopy (UPS) represent a suitable tool to investigate the energy levels of the same films used in the transistors (figure 6.15). The limited penetration depth characteristic of UPS makes this investigation more suitable to explain the FET data, where a nanometer thick channel accumulates at the semiconductor-dielectric interface, rather than the two terminal samples data. By linear extrapolation from the high binding energy region of the spectrum it is possible to derive the position of the Fermi level for pristine PCBM and for the PCBM/MAI film to be, respectively, at -4.27 and -4.13 eV. This is a relatively small but consistent shift of the Fermi level toward the vacuum level when the methylammonium salt is added to the film, indicating a clear *n*-doping effect. From the Fermi level position, as a first approximation, the charge carrier density at thermal equilibrium in both films can be estimated on the basis of a single-crystal lattice

model[21]. In the case of the pristine PCBM the determined electron density is 2.5 × 10^{11} cm^{-3}; while for the PCBM:MAI film is determined a concentration of 5.7 × 10 13 cm^{-3}, two orders of magnitude higher respect to the pristine sample. The calculation of the carriers is determined as follow. The electrons concentration is:

$$n = \frac{ni^2}{p}$$

With *p* the concentration of holes obtained by:

$$p = ni\ e^{\frac{Ef - Efi}{kT}}$$

With *Ef* the Fermi level of PCBM or PCBM:MAI from UPS measurements, *Efi* the intrinsic Fermi level considered at half of the PCBM band gap, *k* the Boltzamann constant and *T* the absolute temperature; *ni* is the intrinsic carrier concentrations at thermal equilibrium:

$$ni = \sqrt{NcNV}\ e^{\frac{Eg}{2kT}}$$

With *Nc* = 10^{21} cm^{-3} and *Nv* = 10^{21} cm^{-3} density of state in the conduction and valence band respectively and *Eg* the energy gap of PCBM.

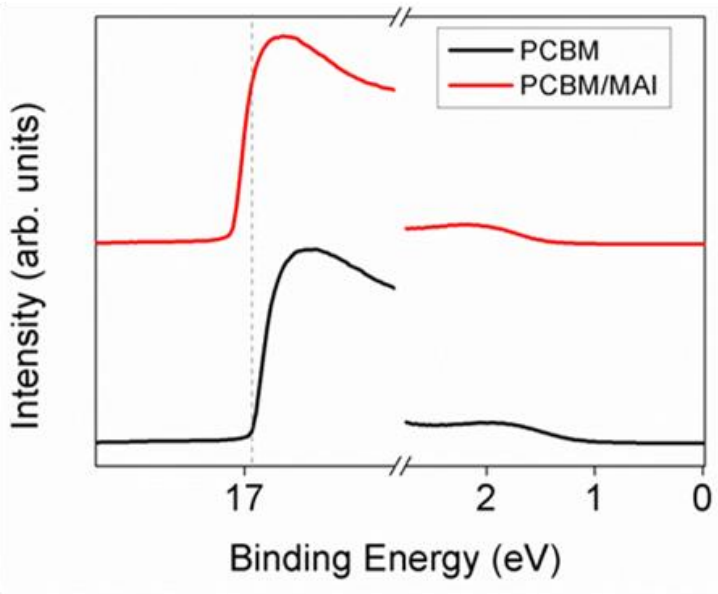

Figure 6.15: UPS spectra showing the evolution of the Fermi level for pristine PCBM (black) and PCBM:MAI (red) films. The dotted lines is used as a guide for the eye for the shift of the Fermi level.

Thanks to these results it is possible to conclude that in the transistor deep trap states are filled by chemically introduced excess carriers, and as a consequence, for the same applied gate voltage, electrostatically accumulated carriers in the channel occupy more mobile states, thus producing a net shift in the threshold voltage and an increased field-effect mobility. These results confirm the interaction between ions and the PCBM that occurs at the interface between the perovskite and the PCBM, with the increased conductivity of the PCBM phase owing to an increased number of free carriers induced by I^- doping.

6.5 Conclusions

In this chapter the hysteresis phenomenon in perovskites based solar cells has been deeply investigated. This phenomenon is one of the major problems that threaten the stability of the devices since it alters the fundamental electrical properties of perovskite itself. After a phenomenological description of the problem, several hypothesis on the nature of the hysteresis have been introduced. It is concluded that the main cause of hysteretic behaviour in perovskite solar cells can be found in the formation of an internal field upon ion migration, the role of the charge extracting layer is of paramount importance in determining the device response to such a transient phenomenon. Efficient charge extraction is critical to make the devices less sensitive to their *J–V* scanning history. This is especially true when monitoring the short-circuit photocurrent density: it was shown that by introducing a PCBM electron extracting layer, though a formation of a *p-i-n*-like junction within the perovskite layer is still expected upon cell operation, the electron transfer rate at the perovskite-PCBM layer results almost unaffected, stabilizing the short-circuit current from the very first J/V scan. This effect is the consequence of another phenomenon which needs to be taken into account both when designing efficient perovskite solar cells and when attempting their modelling. It was reported that, upon ion migration, a modification of the electronic properties of PCBM occurs at the interface with the perovskite. In particular, as an effect of the built-in field, iodide migrates toward the PCBM layer and it chemically dopes the organic semiconductor, increasing its conductivity. Upon “preconditioning” J/V cycles, such doping contributes to improve and stabilize the open-circuit voltage, as previously

observed also for other photovoltaic technologies[22], thus producing an overall stabilization of the device. The latter is a direct consequence of the electron transfer process between the ionic species and the organic molecule, establishing an "electrostatic trap" and reducing iodide back diffusion/drift.

References

[1] - W. Tress, N. Marinova, T. Moehl, S. M. Zakeeruddin, M. K. Nazeeruddin, M. Grätzel *Energy Environ. Sci.* **2015**, 8, 995.

[2] - C. Tao, S. Neutzner, L. Colella, S. Marras, A. R. S. Kandada, M. Gandini, M. De Bastiani, G. Pace, L. Manna, M. Caironi, C. Bertarelli, A. Petrozza, *Energy Environ. Sci.* **2015**, 8, 2365.

[3] - H. J. Snaith, A. Abate, J. M. Ball, G. E. Eperon, T. Leijtens, N. K. Noel, S. D. Stranks, J. T.-W. Wang, K. Wojciechowski, W. Zhang *J. Phys. Chem. Lett.* **2014**, 5, 1511.

[4] - Y. Shao, Z. Xiao, C. Bi, Y. Yuan, J. Huang *Nat. Commun.* **2014**, 5, 5784.

[5] - T. Leijtens, S.D. Stranks, G.E. Eperon, R. Lindblad, E.R.J. Johansson, I.J. McPherson, H. Rensmo, J.M. Ball, M.M. Lee, H.J. Snaith *ACS Nano* **2014**, 8, 7147

[6] - J. Wei, Y. Zhao, H. Li, G. Li, J. Pan, D. Xu, Q. Zhao, D. Yu *J. Phys. Chem. Lett.* **2014**, 5, 3937.

[7] - H.W. Chen, N. Sakai, M. Ikegami, T. Miyasaka *J. Phys. Chem. Lett.* **2015**, 6, 164.

[8] - R. Gottesman, E. Haltzi, L. Gouda, S. Tirosh, Y. Bouhadana, A. Zaban, E. Mosconi, F. De Angelis *J. Phys. Chem. Lett.* **2014**, 5, 2662.

[9] - G.E. Eperon, G.M. Paternò, R.J. Sutton, A. Zampetti, A.A. Haghighirad, F. Cacialli, H.J. Snaith *J. Mater. Chem. A* **2015**, 3, 19688.

[10] - Z. Xiao, Y. Yuan, Y. Shao, Q. Wang, Q. Dong, C. Bi, P. Sharma, A. Gruverman, J. Huang, *Nat. Mater.* **2015**, *14*, 193.

[11] - J. S. Manser, P. V. Kamat, *Nat. Photonics* **2014**, 8, 737.

[12] - S. D. Stranks, G. E. Eperon, G. Grancini, C. Menelaou, M. J. P. Alcocer, T. Leijtens , L. M. Herz, A. Petrozza, H. J. Snaith, *Science* **2013**, 342, 341.

[13] - Y. Yuan, J. Chae, Y. Shao, Q. Wang, Z. Xiao, A. Centrone, J. Huang, *Adv. Energy Mater.* **2015**, 5, 1500615.

[14] - T. Leijtens, E. T. Hoke, G. Grancini, D. J. Slotcavage, G. E. Eperon, J. M. Ball, M. De Bastiani, A. R. Bowring, N. Martino, K. Wojciechowski, M. D. McGehee, H. J. Snaith, A. Petrozza, *Adv. Energy Mater.* **2015**, 5, 20.

[15] - C. Eames, J. M. Frost, P. R. F. Bames, B. C. O'Regan, A. Walsh, M. S. Islam *Nat. Commun.* **2015**, 6, 7497.

[16] - J. M. Azpiroz, E. Mosconi, J. Bisquert, F. De Angelis *Energy Environ. Sci.* **2015**, 8, 2118.

[17] - T.-Y. Yang, G. Gregori, N. Pellet, M. Gratzel, J. Maier, *Angew. Chem.* **2015**, 127, 8016.

[18] - A. Walsh, D. O. Scanlon, S. Chen, X. G. Gong, S-H. Wei *Angew. Chem.* **2015**, 54, 1791.

[19] - C. Z. Li, C. C. Chueh, F. Ding, H. L. Yip, P. W. Liang, X. Li, A. K. Y. Jen, *Adv. Mater.* **2013**, 25, 4425.

[20] - D. Khim, K.-J. Baeg, M. Caironi, C. Liu, Y. Xu, D.-Y. Kim, Y.-Y. Noh *Adv. Funct. Mater.* **2014**, 24, 6252.

[21] - D. Neamen *Semiconductor Physics and Devices*, 4th ed., McGraw Hill Publications , New York City, **2011**.

[22] - K. Wojciechowski, M. Saliba, T. Leijtens, A. Abate, H. J. Snaith *Energy Environ. Sci.* **2014**, 7, 1142.

Conclusions

Evolution and technological progress have a price: energy. The development of renewable energy is the most efficient response of the humankind to answer the demand for energy. Through this vision, the Sun represent an inexhaustible source of energy ready to be exploited in the near future. The solar cells are a suitable way to convert sunlight in energy and for this reason they experienced a constant development over time of the conversion efficiency. However, for real progress, this increment should be compared with the stability of the photophysical processes. Understand and solve the problems that degrade the solar cells is a milestone together the improved efficiencies, both lead to a real exploitation of the photovoltaic processes. The purpose of this thesis is to study the mechanisms that influence the stability of the third generation solar cells with a special focus on two emerging technologies in this field: Organic Photovoltaics (OPVs) and Perovskite based solar cells (PSC). In the following are summarized the main conclusions for each of these studies.

Organic Photovoltaics. One of the most promising material for the light conversion in OPVs is a low band gap polymer (PCPDTBT) blended with a fullerene derivative (PCBM). Behind the high expectations regarding the improved light absorption of this blend, a careful study of the photoinduced dynamics showed a way of loss of photocarriers generation. After light absorption and the creation of Charge Transfer states, part of the energy is transferred to the triplet state of the polymer instead of generating charges. In this picture the triplet state acts as a sink for charges precursors and is macroscopically reflected in a decreased amount of available free charges. However, if on one hand the energetic of the system limits the formation of charges on the other hand it improves the stability of the materials. It is well know that OPVs are strongly affected by the presence of oxygen and/or moisturizing agents, presenting a limit in the processability of these solar cells in inert conditions and in the necessity of encapsulating barriers that affects the overall cost. In air condition oxygen superoxide (a strong oxidizing species that affects polymeric chains) is generated after light exposure from polymer triplet state whenever the energy of this state is 0.98 eV higher respect to the not excited state. For the experimental investigation and the theoretical calculation presented in this thesis, the triplet state of PCPDTBT has an energy lower than 0.98 eV meaning that

it is not a suitable precursor for the oxygen superoxide formation, which results in an enhanced stability of these solar cells in air conditions.

Perovskite Solar Cells. The introduction of metal halide perovskite represented a revolution in the photovoltaic research. This material presents the great advantage of an easy processability, mainly due to the solution-process techniques used, together with efficiency closed to crystalline silicon. However, behind the technological progress reported in the constant increment of the power conversion efficiency, many of the optoelectronic properties of this material are still under debate. This thesis reports a detailed description of the optical properties: absorption spectrum, photoluminescence and the Raman spectrum are described considering the influences of the crystallization substrate and the crystal size of the perovskite. Moreover, the stability of such properties is considered in operating conditions (i.e. under an applied electrical field) which results in the degradation of the optical properties mainly due to the decomposition of the perovskite in moisture environment, accelerated by the presence of the field.

Finally in the last chapter, the stability of the electrical characteristics for PSC is thoroughly addressed, in particular the phenomenon of the “hysteresis” in the current/voltage measurement. It has been demonstrated that the presence of parasitic ionic currents and their interaction with the electron extraction layer such as fullerene derivatives plays an important role in the device operation. The understanding of such mechanisms is a fundamental milestone in order to exploit this material in the real-world application.

Dissemination

List of Publications

1. ***De Bastiani M.****, Dell'Erba G., Gandini M., D'Innocenzo V., Neutzner S., Kandada A. R. S., Grancini G., Binda M., Prato M., Ball J. M., Caironi M. and Petrozza A.,* Ion Migration and the the Role of Pre-conditioning cycles in the Stabilization of the J-V Characteristics of Inverted Hybrid Perovskite Solar Cells, *Adv. Energy Mater.* DOI: 10.1002/aenm.201501453
2. ***De Bastiani M****, D'Innocenzo V.*, Stranks S. D., Snaith H. J. And Petrozza A.* Role of the crystallization substrate on the photoluminescence properties of organo-lead mixed halides perovskites, *APL Mater*. **2014**, 2 (8), 081509 (* equally contributed).
3. *Grancini G.*, **De Bastiani M.***, Martino N., Fazzi D., Egelhaaf H-J., Sauermann T., Antognazza MR., Lanzani G., Caironi M., Franco L., Petrozza A.* The critical role of interfacial dynamics in the stability of organic photovoltaic devices *Phys. Chem. Chem. Phys.* **2014**, 16, 8249 (* equally contributed).
4. *Grancini G., Kandada A. R. S., Frost J. M., Barker A. J.,* ***De Bastiani M.****, Gandini M., Marras S., Lanzani G., Walsh A., Petrozza A.,* Role of microstructure in the electron–hole interaction of hybrid lead halide perovskites, *Nature Photon*. **2015**, 9, 695.
5. *Leijtens T., Hoke E. T. H., Grancini G., Slotcavage D. J., Eperon G. E., Ball J. M.,* ***De Bastiani M.****, Bowring A. R., Martino N., Wojciechowski K., McGehee M. D., Snaith H. J., Petrozza A.* Mapping Electric Field–Induced Switchable Poling and Structural Degradation in Hybrid Lead Halide Perovskite Thin Films *Adv. Energy Mater.* **2015**, 1500962.
6. *Tao C., Neutzner S., Colella L., Marras S., Kandada A. R. S, Gandini M.,* ***De Bastiani M.****, Pace G., Manna L., Caironi M., Bertarelli C., Petrozza A.* 17.6% stabilized efficiency in low-temperature processed planar perovskite solar cells *Energy Environ. Sci*, **2015**, 8, 2365
7. *Zhang Y., Liu M., Eperon G. E., Leijtens T. C., McMeekin D., Saliba M., Zhang W.,* ***De Bastiani M.****, Petrozza A., Herz L. M., Johnston M. B., Lin H., Snaith H. J.* Charge selective contacts, mobile ions and anomalous hysteresis in organic–inorganic perovskite solar cells *Mater. Horiz.* **2015**, 2, 315.
8. *D'Innocenzo V., Kandada A. R. S.,* ***De Bastiani M.****, Gandini M., Annamaria Petrozza* Tuning the light emission properties by band gap engineering in hybrid lead halide perovskite *J. Am. Chem. Soc.* **2014**, 136 (51), 17730.
9. *Grancini G., Marras S., Prato M., Giannini C., Quarti C., De Angelis F.,* ***De Bastiani M.****, Eperon G. E., Snaith H. J., Manna L., Petrozza A.* The impact of the crystallization processes on the structural and optical properties of hybrid perovskite films for photovoltaics *J. Phys Chem. Lett.* **2014**, 5, 3836.

Conferences Presentation

1) 2015 MRS-Spring Meeting:
   Charge Extraction Layer Investigation for High Efficiency and Hysteresis-Less Organo Lead Halide Perovskite Solar Cell
   oral contribution

2) 2015 MESO-Workshop:
   Impact of the electron extracting layer in Hybrid Perovskite solar Cells
   oral contribution

3) 2014 SSSC-NanoGe:
   Role of the crystallization substrate on the photoluminescence properties of organo-lead mixed halides perovskites
   oral contribution

4) 2014 Workshop Photovoltaics New frontiers and applications:
   Charge Extraction Layer for High Efficiency, Low-Temperature and Hysteresis-less Organo Lead Halide Perovskite Solar Cells
   poster contribution

5) 2013 E-MRS-Spring Meeting:
   The Role of the Oxygen and Triplet states in the PCPDTBT:PCBM organic solar cells: Investigation on the Photo-Induced Dynamics.
   poster contribution

Awards

1) Best Poster Award: 2013 E-MRS Spring Meeting, Symposium B:
   The Role of the Oxygen and Triplet states in the PCPDTBT:PCBM organic solar cells: Investigation on the Photo-Induced Dynamics.

Ringraziamenti

Alla fine di tutto, guardando indietro, una tesi di dottorato è abbastanza simile ad un viaggio. Gli esperimenti, i risultati, i lavori conclusi e quelli abbandonati, le buone idee e quelle sbagliate. Tutto questo rappresenta un bagaglio di esperienze che caratterizzano una persona e col tempo contribuiranno a farne un ricercatore. Ma la cosa più importante, restano le persone che si sono incontrate: colleghi, amici e tutti quelli presenti in questi anni. Perché la ricerca si basa sulle idee, e le idee vengono dalle persone.

Questo lavoro è dedicato alla mia famiglia per avermi sempre aiutato e sostenuto, nelle scelte facili e in quelle meno chiare, e spero che un giorno possa essere un riferimento per chi verrà dopo di me. Senza troppe spiegazioni, a loro è dedicato il più grande Grazie.

Un tutor è una figura importante in un dottorato. E in questo non posso che ritenermi fortunato. Quello che ho imparato in questi anni lo devo principalmente ad Anna. Certo, ci sono stati dei momenti in cui le cose sembravano difficili, ma non fa parte del gioco? Alla fine imparare significa anche riuscire a risolvere i problemi. Grazie di cuore, per avermi dato la possibilità di lavorare anche sulle mie idee, giuste o sbagliate che fossero.

Un grazie sincero è dedicato anche al prof. Meneghetti, per avermi sostenuto ed aiutato fin dal principio, ma soprattutto per avermi dato la possibilità di vivere quest'esperienza unica.

E poi ci sono tutti i ragazzi del CNST. Non si vive solo di Scienza. Grazie a tutti quelli che mi hanno aiutato, chi con una birra, chi con un esperimento. In particolare l'ufficio tecnico - lo scheletro portante del centro - Luca, Enrico, Stefano, la Ale e l'onnisciente Desii. E poi i postdoc, primo fra tutti James, poi Ajay, Lamberti, Giulia e per finire tutti quelli che come me hanno vissuto il centro anche fuori dai laboratori: Dalle, Mez, Seba, Sadir, Pupi, Simone, Perinot, Passoni, Nico e tutti gli altri ragazzi…

Un ringraziamento particolare va ad un'Ancora e una Vela Spezzata, perché a volte non si è solo colleghi, ma questo voi lo sapete già.

L'ultimo ringraziamento lo voglio dedicare a Giulia, per essermi stata vicino in questo tempo, ma soprattutto per quello che verrà dopo.

Milano, Gennaio 2016

Michele De Bastiani